

**UNIVERSIDADE DE SÃO PAULO  
INSTITUTO DE FÍSICA DE SÃO CARLOS**

**Raul Ribeiro Prado**

**Modelo para teses e dissertações em  $\text{\LaTeX}$  utilizando a  
classe USPSC para o IFSC**

**São Carlos**

**2017**



**Raul Ribeiro Prado**

**Modelo para teses e dissertações em  $\text{\LaTeX}$  utilizando a  
classe **USPSC** para o IFSC**

Tese apresentada ao Programa de Pós-Graduação em Física do Instituto de Física de São Carlos da Universidade de São Paulo, para obtenção do título de Doutor em Ciências.

Área de concentração: Física Aplicada

Supervisor: Prof. Dr. Luiz Vitor de Souza Filho

**Versão original**

**São Carlos  
2017**

Folha de aprovação em conformidade  
com o padrão definido  
pela Unidade.

No presente modelo consta como  
folhadeaprovacao.pdf





# Acknowledgements



*“O estudo, a busca da verdade e da beleza são domínios  
em que nos é consentido sermos crianças por toda a vida.”*

*Albert Einstein*



# Abstract

PRADO, R. R. **Model for theses and dissertations in L<sup>A</sup>T<sub>E</sub>X using the USPSC class to the IFSC.** 2017. 131p. Tese (Doutorado em Ciências) - Instituto de Física de São Carlos, Universidade de São Paulo, São Carlos, 2017.

This is the english abstract.

**Keywords:** .



# Resumo

PRADO, R. R. **Modelo para teses e dissertações em L<sup>A</sup>T<sub>E</sub>X utilizando a classe USPSC para o IFSC.** 2017. 131p. Tese (Doutorado em Ciências) - Instituto de Física de São Carlos, Universidade de São Paulo, São Carlos, 2017.

**Palavras-chave:** .



# List of Figures

Figure 1 –	59
Figure 2 –	59
Figure 3 – Illustration of the phase space binning used for the charged hadron analysis.	63
Figure 4 – Illustration of the phase space binning used for the $V^0$ analysis. The plot on the left show the binning used for $\Lambda$ and $\bar{\Lambda}$ and the plot on the right show the binning used for $K_S^0$ .	64
Figure 5 – <b>(DO IT)</b> [1]	65
Figure 6 – $dE/dx$ data used in this analysis. Positively and negatively charged tracks are shown repectively in (a) and (b) for the 158 GeV/c data set, and in (c) and (d) for the 350 GeV/c one. The solid curves show the $\langle dE/dx \rangle$ parametrization for each particle type. <b>(noise rejection)</b>	67
Figure 7 – Examples of the fitted $dE/dx$ distributions from the 158 GeV/c dataset. On the top, the distributions of the (a) negatively and (b) positively charged tracks are shown for one phase space bin of the RST subset. On the bottom, the distributions of the (c) negatively and (d) positively charged tracks are shown for a different phase space bin of the WST subset. The values of the $\langle p \rangle$ and $\langle p_T \rangle$ for each phase space bin is indicated on the top of each plot. The black dots show the observed number of tracks, while the colored distributions are the results of the $dE/dx$ fit for each particle type. On the bottom of each plot, we show the residual of the fit, defined as the difference between the observed and the expected number of tracks from the result of the fit, divided by the uncertainty of the observed number.	73
Figure 8 – $\chi^2/\text{ndf}$ of the $dE/dx$ fit for the 158 GeV/c data set. The RST and WST are shown in (a) and (b), respectively.	74
Figure 9 – Calibration constants obtained from the $dE/dx$ fit of the RST and 158 GeV/c data set.	74
Figure 10 – Shape parameters obtained from the $dE/dx$ fit of the RST and 158 GeV/c data set.	75
Figure 11 – Particle fractions obtained from the $dE/dx$ fit of the RST and 158 GeV/c data set.	76

Figure 12 – Examples of the parametrization of the particle fractions to be used to create the Simulated Data Ensembles. The plots in (a) and (b) refer to the 158 GeV/c data set and in (c) and (d) to the 350 GeV/c one. The particle type, the RST/WST subset and the $\langle p_T \rangle$ are indicated on the top of each plot. The black dots show the particle fractions obtained from the $dE/dx$ fit and the red curves show the result of the fit of the Eq. (7.13) to these fractions. . . . .	78
Figure 13 – Relative standard deviation ( $\sigma_r$ , see the definition in the text) of the particle fractions obtained with the SDEs for the RST and 158 GeV/c case. The $\pi^+$ case is shown in (a), $\pi^-$ in (b), $K^+$ in (c), $K^-$ in (d), $p^+$ in (e) and $p^-$ in (f). . . . .	79
Figure 14 – Average relative bias ( $\delta_r$ , see the definition in the text) of the particle fractions obtained with the SDEs for the RST and 158 GeV/c case. The $\pi^+$ case is shown in (a), $\pi^-$ in (b), $K^+$ in (c), $K^-$ in (d), $p^+$ in (e) and $p^-$ in (f). . . . .	80
Figure 15 – Correction factors ( $c$ , see the definition in the text) for the RST and 158 GeV/c case. The $\pi^+$ case is shown in (a), $\pi^-$ in (b), $K^+$ in (c), $K^-$ in (d), $p^+$ in (e) and $p^-$ in (f). . . . .	81
Figure 16 – Particle fractions obtained from the $dE/dx$ fit of the RST and 158 GeV/c dataset, with target inserted. . . . .	82
Figure 17 – . . . . .	87
Figure 18 – . . . . .	87
Figure 19 – Optimization of the $L_{\text{decay}}^{\text{cut}}$ for the 158 GeV/c dataset. The plot on left, middle and right shows $\Lambda$ , $\bar{\Lambda}$ and $K_S^0$ , respectively. . . . .	88
Figure 20 – Examples of the fitted $m_{\text{inv}}$ distributions for the 158 GeV/c dataset. The plot on left, middle and right shows $\Lambda$ , $\bar{\Lambda}$ and $K_S^0$ , respectively. . . . .	88
Figure 21 – Examples of the fitted $m_{\text{inv}}$ distributions for the 158 GeV/c dataset, with target removed. The plot on left, middle and right shows $\Lambda$ , $\bar{\Lambda}$ and $K_S^0$ , respectively. . . . .	89
Figure 22 – . . . . .	89
Figure 23 – . . . . .	89
Figure 24 – . . . . .	90
Figure 25 – $\beta$ correction factor for the 158 GeV/c dataset. . . . .	91
Figure 26 – $\beta$ correction factor for the 158 GeV/c dataset. . . . .	92

Figure 27 – Examples of the fitted  $dE/dx$  distributions from the 350 GeV/ $c$  dataset.

On the top, the distributions of the (a) negatively and (b) positively charged tracks are shown for one phase space bin of the RST subset. On the bottom, the distributions of the (c) negatively and (d) positively charged tracks are shown for a different phase space bin of the WST subset. The values of the  $\langle p \rangle$  and  $\langle p_T \rangle$  for each phase space bin is indicated on the top of each plot. The black dots show the observed number of tracks, while the colored distributions are the results of the  $dE/dx$  fit for each particle type. On the bottom of each plot, we show the residual of the fit, defined as the difference between the observed and the expected number of tracks from the result of the fit, divided by the uncertainty of the observed number. . . . . 97

Figure 28 –  $\chi^2/ndf$  of the  $dE/dx$  fit for the 350 GeV/ $c$  data set. The RST and WST are shown in (a) and (b), respectively. . . . . 98

Figure 29 – Calibration constants obtained from the  $dE/dx$  fit of the WST and 158 GeV/ $c$  data set. . . . . 98

Figure 30 – Calibration constants obtained from the  $dE/dx$  fit of the RST and 350 GeV/ $c$  data set. . . . . 99

Figure 31 – Calibration constants obtained from the  $dE/dx$  fit of the WST and 350 GeV/ $c$  data set. . . . . 100

Figure 32 – Shape parameters obtained from the  $dE/dx$  fit of the WST and 158 GeV/ $c$  data set. . . . . 101

Figure 33 – Shape parameters obtained from the  $dE/dx$  fit of the RST and 350 GeV/ $c$  data set. . . . . 102

Figure 34 – Shape parameters obtained from the  $dE/dx$  fit of the WST and 350 GeV/ $c$  data set. . . . . 102

Figure 35 – Particle fractions obtained from the  $dE/dx$  fit of the WST and 158 GeV/ $c$  data set. . . . . 103

Figure 36 – Particle fractions obtained from the  $dE/dx$  fit of the RST and 350 GeV/ $c$  data set. . . . . 104

Figure 37 – Particle fractions obtained from the  $dE/dx$  fit of the WST and 350 GeV/ $c$  data set. . . . . 105

Figure 38 – Relative standard deviation ( $\sigma_r$ , see the definition in the text) of the particle fractions obtained with the SDEs for the WST and 158 GeV/ $c$  case. The  $\pi^+$  case is shown in (a),  $\pi^-$  in (b),  $K^+$  in (c),  $K^-$  in (d),  $p^+$  in (e) and  $p^-$  in (f). . . . . 106

Figure 39 – Relative standard deviation ( $\sigma_r$ , see the definition in the text) of the particle fractions obtained with the SDEs for the RST and 350 GeV/c case. The $\pi^+$ case is shown in (a), $\pi^-$ in (b), $K^+$ in (c), $K^-$ in (d), $p^+$ in (e) and $p^-$ in (f). . . . .	107
Figure 40 – Relative standard deviation ( $\sigma_r$ , see the definition in the text) of the particle fractions obtained with the SDEs for the WST and 350 GeV/c case. The $\pi^+$ case is shown in (a), $\pi^-$ in (b), $K^+$ in (c), $K^-$ in (d), $p^+$ in (e) and $p^-$ in (f). . . . .	108
Figure 41 – Average relative bias ( $\delta_r$ , see the definition in the text) of the particle fractions obtained with the SDEs for the WST and 158 GeV/c case. The $\pi^+$ case is shown in (a), $\pi^-$ in (b), $K^+$ in (c), $K^-$ in (d), $p^+$ in (e) and $p^-$ in (f). . . . .	109
Figure 42 – Average relative bias ( $\delta_r$ , see the definition in the text) of the particle fractions obtained with the SDEs for the RST and 350 GeV/c case. The $\pi^+$ case is shown in (a), $\pi^-$ in (b), $K^+$ in (c), $K^-$ in (d), $p^+$ in (e) and $p^-$ in (f). . . . .	110
Figure 43 – Average relative bias ( $\delta_r$ , see the definition in the text) of the particle fractions obtained with the SDEs for the RST and 350 GeV/c case. The $\pi^+$ case is shown in (a), $\pi^-$ in (b), $K^+$ in (c), $K^-$ in (d), $p^+$ in (e) and $p^-$ in (f). . . . .	111
Figure 44 – Correction factors ( $c$ , see the definition in the text) for the WST and 158 GeV/c case. The $\pi^+$ case is shown in (a), $\pi^-$ in (b), $K^+$ in (c), $K^-$ in (d), $p^+$ in (e) and $p^-$ in (f). . . . .	112
Figure 45 – Correction factors ( $c$ , see the definition in the text) for the RST and 350 GeV/c case. The $\pi^+$ case is shown in (a), $\pi^-$ in (b), $K^+$ in (c), $K^-$ in (d), $p^+$ in (e) and $p^-$ in (f). . . . .	113
Figure 46 – Correction factors ( $c$ , see the definition in the text) for the RST and 350 GeV/c case. The $\pi^+$ case is shown in (a), $\pi^-$ in (b), $K^+$ in (c), $K^-$ in (d), $p^+$ in (e) and $p^-$ in (f). . . . .	114
Figure 47 – Particle fractions obtained from the $dE/dx$ fit of the WST and 158 GeV/c dataset, with target inserted. . . . .	115
Figure 48 – Particle fractions obtained from the $dE/dx$ fit of the RST and 350 GeV/c dataset, with target inserted. . . . .	116
Figure 49 – Particle fractions obtained from the $dE/dx$ fit of the WST and 350 GeV/c dataset, with target inserted. . . . .	117
Figure 50 – Particle fractions obtained from the $dE/dx$ fit of the RST and 158 GeV/c dataset, with target removed. . . . .	118
Figure 51 – Particle fractions obtained from the $dE/dx$ fit of the WST and 158 GeV/c dataset, with target inserted. . . . .	119

Figure 52 – Particle fractions obtained from the $dE/dx$ fit of the RST and 350 GeV/c dataset, with target inserted. . . . .	120
Figure 53 – Particle fractions obtained from the $dE/dx$ fit of the WST and 350 GeV/c dataset, with target inserted. . . . .	121
Figure 54 – Optimization of the $L_{\text{decay}}^{\text{cut}}$ for the 350 GeV/c dataset. The plot on left, middle and right shows $\Lambda$ , $\bar{\Lambda}$ and $K_S^0$ , respectively. . . . .	122
Figure 55 – . . . . .	123
Figure 56 – . . . . .	123
Figure 57 – . . . . .	123
Figure 58 – Examples of the fitted $m_{\text{inv}}$ distributions for the 350 GeV/c dataset. The plot on left, middle and right shows $\Lambda$ , $\bar{\Lambda}$ and $K_S^0$ , respectively. . . . .	124
Figure 59 – Examples of the fitted $m_{\text{inv}}$ distributions for the 350 GeV/c dataset, with target removed. The plot on left, middle and right shows $\Lambda$ , $\bar{\Lambda}$ and $K_S^0$ , respectively. . . . .	124
Figure 60 – $\beta$ correction factor for the 350 GeV/c dataset. . . . .	125
Figure 61 – $\beta$ correction factor for the 350 GeV/c dataset. . . . .	125



# List of Tables

Table 1 – Number of events after the event selection for the data and simulation sets and for both beam momenta, 158 and 350 GeV/ $c$ .	63
Table 2 –	83
Table 3 –	91



# Contents

<b>1</b>	<b>Introduction</b>	<b>23</b>
<b>2</b>	<b>Ultra-high energy cosmic rays</b>	<b>25</b>
<b>3</b>	<b>Extensive air showers and UHECR composition</b>	<b>27</b>
3.1	Extensive air shower phenomenology	27
3.1.1	Electromagnetic component	27
3.1.2	Hadronic component and muon production	27
3.1.3	Longitudinal and lateral profiles	27
3.2	Extensive air shower simulations	27
3.2.1	Hadronic interaction models	27
3.3	Measurements of EAS observables and UHECR composition	27
3.3.1	Shower maximum ( $X_{\max}$ ) and UHECR composition	27
3.3.2	Number of muons ( $N_\mu$ ) and the muon excess	27
3.3.3	Muon production depth ( $X_{\max}^\mu$ )	27
3.3.4	Further measurements	27
<b>4</b>	<b>UHECR detection and the Pierre Auger Observatory</b>	<b>29</b>
<b>5</b>	<b>Interpretation of measurements of the number of muons in extensive air shower experiments</b>	<b>31</b>
<b>6</b>	<b>A new air-shower observable to constrain hadronic interaction models</b>	<b>45</b>
<b>7</b>	<b>Hadron production in pion-carbon interactions</b>	<b>57</b>
7.1	NA61/SHINE experiment	58
7.1.1	Beam	59
7.1.2	Beam detectors and trigger system	59
7.1.3	Time projection chambers	60
7.2	Data and simulation sets	61
7.3	Event selection	61
7.4	Phase space binning	62
7.5	Particle identification for the charged hadron analysis	63
7.5.1	Track selection	64
7.5.2	$dE/dx$ measurements	65
7.5.3	$dE/dx$ model	67
7.5.4	$dE/dx$ fit strategy	69
7.5.5	$dE/dx$ fit results	72
7.5.6	Simulated data ensembles, cuts and corrections	75
7.5.7	Particle identification results	79
7.6	$V^0$ analysis	83
7.6.1	$V^0$ selection	83

7.6.2	Signal extraction strategy . . . . .	84
7.6.3	$V^0$ cuts . . . . .	86
7.6.4	Signal extraction results . . . . .	87
7.7	Monte Carlo corrections . . . . .	89
7.7.1	Feed-down from weak decays . . . . .	92
7.8	Spectra . . . . .	93
7.8.1	Statistical uncertainties . . . . .	93
7.8.2	Systematic uncertainties . . . . .	94
7.8.3	Integration over $p_T$ . . . . .	95
7.9	Results . . . . .	96
7.10	Summary and conclusions . . . . .	96
<b>8</b>	<b>Conclusions</b> . . . . .	<b>127</b>
	<b>Bibliography</b> . . . . .	<b>129</b>

# 1 Introduction



## 2 Ultra-high energy cosmic rays



# 3 Extensive air showers and UHECR composition

## 3.1 Extensive air shower phenomenology

- 3.1.1 Electromagnetic component
- 3.1.2 Hadronic component and muon production
- 3.1.3 Longitudinal and lateral profiles

## 3.2 Extensive air shower simulations

-softwares: CORSIKA, CONEX, etc

### 3.2.1 Hadronic interaction models

- low energy
- high energy

## 3.3 Measurements of EAS observables and UHECR composition

- 3.3.1 Shower maximum ( $X_{\max}$ ) and UHECR composition
- 3.3.2 Number of muons ( $N_\mu$ ) and the muon excess
- 3.3.3 Muon production depth ( $X_{\max}^\mu$ )
- 3.3.4 Further measurements

- risetime asymmetry
- delta method



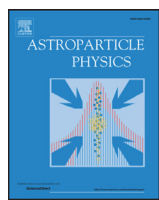
## 4 UHECR detection and the Pierre Auger Observatory



## 5 Interpretation of measurements of the number of muons in extensive air shower experiments



Contents lists available at ScienceDirect



## Interpretation of measurements of the number of muons in extensive air shower experiments

Raul R. Prado <sup>a,\*</sup>, Ruben Conceição <sup>b</sup>, Mário Pimenta <sup>b</sup>, Vitor de Souza <sup>a</sup><sup>a</sup> Instituto de Física de São Carlos, Universidade de São Paulo, São Carlos, Brazil<sup>b</sup> Laboratório de Instrumentação e Física Experimental de Partículas, Lisbon, Portugal

## ARTICLE INFO

## Article history:

Received 25 January 2016

Revised 8 June 2016

Accepted 19 July 2016

Available online 20 July 2016

## Keywords:

Ultra high energy cosmic rays

Muons

Composition

## ABSTRACT

In this paper we analyze the energy evolution of the muon content of air showers between  $10^{18.4}$  and  $10^{19.6}$  eV to be able to determine the most likely mass composition scenario from future number of muons measurements. The energy and primary mass evolution of the number of muons is studied based on the Heitler-Matthews model and Monte Carlo simulation of the air shower. A simple model to describe the evolution of the first and second moments of number of muons distributions is proposed and validated. An analysis approach based on the comparison between this model's predictions and data to discriminate among a set of composition scenarios is presented and tested with simulations. It is shown that the composition scenarios can be potentially discriminated under the conditions imposed by the method. The discrimination power of the proposed analysis is stable under systematic changes of the absolute number of muons from model predictions and on the scale of the reconstructed energy.

© 2016 Elsevier B.V. All rights reserved.

### 1. Introduction

The energy spectrum of ultra high energy cosmic rays (UHECRs) has been measured recently with high precision and two major features were confirmed. The ankle ( $\log(E/\text{eV}) \sim 18.7$ ) and the flux suppression ( $\log(E/\text{eV}) \sim 19.5$ ) have been undoubtedly established by HiRes [1], the Pierre Auger Observatory [2,3] and Telescope Array [4]. However, the astrophysical interpretation of these structures cannot be inferred with complete certainty mainly because of the lack of knowledge on the UHECR composition at these energies. In a light abundance scenario, the ankle could be interpreted as the modulation resulting from the particle interaction with radiation backgrounds [5,6]. On the other hand, it could also be explained as the transition from galactic to extra-galactic cosmic rays [7]. The flux suppression can be equally well described by the energy losses of extra-galactic particles due to interactions with CMB photons [8] or by the maximum reachable energy of the astrophysical acceleration mechanisms in nearby sources [9]. In each one of these astrophysical scenarios, the energy evolution of the UHECR composition is significantly different.

The UHECR measurements are done indirectly through the detection of extensive air showers. Therefore, the determination of

the composition depends strongly on the data analysis capability to correlate the measured properties of the shower to the primary particle type. This correlation is achieved using air shower simulations. However, intrinsic fluctuations of the showers and uncertainties in the high energy hadronic interaction models for energies above  $10^{17}$  eV prevent us from a definitive conclusion about the primary particle type for each event. Statistical analysis and evolution trends [10,11] are used to minimize the fluctuation effects, nevertheless an unique interpretation of the data is not possible because of the hadronic interaction model uncertainties. Currently, the most reliable observable to investigate composition at higher energies is  $X_{\max}$ , the atmospheric depth at which the shower reaches the maximum number of particles [12]. A second very powerful observable sensitive to primary particle mass is the number of muons ( $N_\mu$ ) in the showers. However, the lack of knowledge of the high energy hadronic interactions and the systematic uncertainties in the energy determination limit the interpretation of  $N_\mu$  data in terms of composition in a more severe way than they do for  $X_{\max}$ . There are several indications that the current most often used hadronic interaction models fail at predicting the muonic component features of air showers [13,14]. Moreover, as  $N_\mu$  scales directly with shower energy, the systematic uncertainty in energy reconstruction (typically  $\sim 10 - 20\%$ ) represents also a difficult challenge to overcome in the interpretation of the  $N_\mu$  data. As a consequence, it is not straightforward to envisage a data analysis procedure that extracts the mass abundance from the  $N_\mu$  data.

\* Corresponding author.

E-mail address: [raul.prado@usp.br](mailto:raul.prado@usp.br) (R. R. Prado).

In this paper we propose a new approach to interpret  $N_\mu$  data which accommodates the systematic uncertainties of the high energy hadronic interaction models and of the energy reconstruction. The analysis proposed here is based on the energy evolution of the first ( $\langle \log_{10} N_\mu \rangle$ ) and second ( $\sigma[\log_{10} N_\mu]$ ) moments of the  $\log_{10} N_\mu$  distribution. There are two central features of the proposed procedure: (a) a simplified model to describe the energy and mass evolution of  $\langle \log_{10} N_\mu \rangle$  and  $\sigma[\log_{10} N_\mu]$  which minimizes the hadronic interaction model dependencies, and (b) a comparison between the predictions of this model for a set of given composition scenarios and the data integrated in energy to maximize the discrimination power.

First in [Section 2](#) we propose a simplified model to describe the energy and mass evolution of  $\langle \log_{10} N_\mu \rangle$  and  $\sigma[\log_{10} N_\mu]$ . We argue that to a very good approximation only two parameters ( $a$  and  $b$ ) summarize all uncertainties of the currently used high energy hadronic interaction models. This simplification of the description of  $\langle \log_{10} N_\mu \rangle$  and  $\sigma[\log_{10} N_\mu]$  with energy and mass is an important step in the analysis procedure because it minimizes the dependencies on hadronic interaction models in the interpretation of the data. In [Section 3.1](#) we use shower simulations to study the energy and mass evolution of  $\langle \log_{10} N_\mu \rangle$  and  $\sigma[\log_{10} N_\mu]$  and to validate the model proposed in [Section 2](#). We also introduce in [Section 3.1](#) the algorithm developed to build the large set of simulations used in this paper. This simulation process is complemented in [Appendix A](#).

In [Section 4](#) we introduce a set of six benchmark composition scenarios defined by the percentage of proton, helium, nitrogen and iron nuclei as a function of energy. Four composition scenarios are astrophysical motivated (based in Refs. [6–9,15]) and two were derived from the  $X_{\max}$  measurements performed by the Pierre Auger Collaboration (based on Ref. [16]). By using simulations we also study the energy evolution of  $\langle \log_{10} N_\mu \rangle$  and  $\sigma[\log_{10} N_\mu]$  for each one of these scenarios and evaluate the effects of the uncertainties on the energy scale and on the absolute  $N_\mu$  due to the misprediction by the hadronic interaction models.

In [Section 5](#) we show how the model proposed in [Section 2](#) can be used to discriminate between these representative composition scenarios. The comparison of the model predictions for the composition scenarios with the data in an energy range is the important step of the analysis procedure proposed here because it maximizes the discrimination power allowing us to identify the most likely scenario that generated a set of  $N_\mu$  data. This comparison is done by the traditional  $\chi^2$ , which assumes the minimal value for the composition scenario which best describes the data. We use simulations to test our approach and show that it is possible to achieve a good discrimination between the chosen scenarios supposing a realistic case with the statistic to be collected during 3 years of data taking with the Pierre Auger Observatory Upgrade - AugerPrime. We also show that the systematic uncertainties in the energy reconstruction and on the absolute scale of the number of muons do not mix the composition scenarios. Hence we conclude in [Section 6](#) that by using only the energy evolution of  $\langle \log_{10} N_\mu \rangle$  and  $\sigma[\log_{10} N_\mu]$  it would be possible to identify, by comparing the composition scenarios to the data, the scenario which best describes the measurements of  $N_\mu$ .

## 2. A model for the energy and mass evolution of $\log_{10} N_\mu$ moments

In this section we present a model to describe the energy and primary mass evolution of the  $\log_{10} N_\mu$  first and second moments. The Heitler-Matthews model [17] is a semi-empirical description of the shower development which describes the dependencies of

the mean  $N_\mu$  as

$$\langle N_\mu \rangle_A = A^{1-\beta} N_\mu^p \quad (1)$$

and

$$\langle N_\mu \rangle_E = \left( \frac{E}{\zeta_c^\pi} \right)^\beta, \quad (2)$$

where  $N_\mu^p$  is the number of muons in a proton shower and  $\zeta_c^\pi$  is the pion critical energy, assumed to be equal to 20 GeV in [17].  $\beta$  is often taken to be constant because its value is shown to vary in a small interval from 0.85 to 0.92 [17,18].

Both equations define a clear linear relation of  $\langle \log_{10} N_\mu \rangle$  with energy and mass that can be summarized as

$$\langle \log_{10} N_\mu \rangle_{E,A} = a + D_A \cdot \ln(A) + D_E \cdot (\log_{10} E - 19.0), \quad (3)$$

where  $D_E = \beta \simeq 0.85 - 0.92$ ,  $D_A = (1 - \beta) \cdot \log_{10} e \simeq 0.434 \cdot (1 - \beta) \simeq 0.0347 - 0.0651$ , and the energy  $E$  is given in eV. Because of our lack of knowledge of the hadronic interactions at the highest energies, the value of  $a$  is highly model dependent and presents a large variability. It can be written as  $a = \log_{10}(N_\mu^p) - \beta \log_{10}(\zeta_c^\pi)$  and varies approximately from 6.5 to 8.0, depending on the hadronic interaction model. These values of  $a$  were obtained using the simulations described in [Section 3](#).

In addition to the  $\langle \log_{10} N_\mu \rangle$ , the  $\sigma[\log_{10} N_\mu]$  could also be modeled by the same approach. However, no analytic model has been proposed to describe the shower-to-shower fluctuations and our study relies on simulations to propose a similar description of  $\sigma[\log_{10} N_\mu]$  evolution with energy and mass. We propose that the  $\sigma[\log_{10} N_\mu]$  can be described as

$$\sigma[\log_{10} N_\mu]_A = \sigma[\log_{10} N_\mu]_{Fe} + b \cdot [\ln(A) - \ln(56)]^2, \quad (4)$$

where  $\sigma[\log_{10} N_\mu]_{Fe}$  is the  $\sigma[\log_{10} N_\mu]$  for iron nucleus initiated showers. Two main assumptions were used in this proposal: a) for a fixed primary (A), the  $\sigma[\log_{10} N_\mu]$  does not depend on energy and b) a quadratic dependency of  $\sigma[\log_{10} N_\mu]$  with  $\ln(A)$ . These assumptions are justified in [Section 3](#) via Monte Carlo simulation of the air shower.

The description of the  $\sigma[\log_{10} N_\mu]$  is analogous to the deduction of  $\langle \log_{10} N_\mu \rangle$  using the Heitler-Matthews models in the following way. We will show in [Section 3](#) that, for the purposes of this paper's analysis,  $\sigma[\log_{10} N_\mu]_{Fe}$  can be taken to be constant, in other words, the small model dependence of  $\sigma[\log_{10} N_\mu]_{Fe}$  can be ignored. On the other hand,  $b$  changes significantly with the hadronic interaction model, which reflects the theoretical uncertainties concerning the muonic component description.

[Eqs. \(3\)](#) and [\(4\)](#) summarize the first step of this paper. These equations offer a simple, but good description of the two first moments of the  $\log_{10} N_\mu$  distribution with energy and mass. The uncertainties due to hadronic interaction model descriptions are only significant for two parameters,  $a$  and  $b$ , while for the further parameters there is a good agreement between their predictions. The quality of the description given by [Eqs. \(3\)](#) and [\(4\)](#) is going to be numerically studied in the next section.

For a mixture of primaries in which each primary particle type,  $i$ , has mass  $A_i$  and contributes to the total flux with a fraction given by  $f_i$ , we can show that  $\langle \log_{10} N_\mu \rangle$  and  $\sigma[\log_{10} N_\mu]$  of the mixture (mix) can be calculated as follows

$$\langle \log_{10} N_\mu \rangle_{mix} = \sum_i f_i \cdot \langle \log_{10} N_\mu \rangle_{A_i} \quad (5)$$

$$\langle \log_{10} N_\mu \rangle_{mix} = a + D_A \cdot \langle \ln(A) \rangle_{mix} + D_E \cdot (\log_{10} E - 19.0),$$

and

$$\begin{aligned} \sigma^2[\log_{10} N_\mu]_{\text{mix}} &= \sum_i f_i \cdot \left[ (\langle \log_{10} N_\mu \rangle_{A_i} - \langle \log_{10} N_\mu \rangle_{\text{mix}})^2 + \sigma^2[\log_{10} N_\mu]_{A_i} \right]. \end{aligned} \quad (6)$$

Using Eq. (3) we can write

$$\begin{aligned} \sigma^2[\log_{10} N_\mu]_{\text{mix}} &= \sum_i f_i \cdot [D_A^2 \cdot (\ln(A_i) - \langle \ln(A) \rangle_{\text{mix}})^2 + \sigma^2[\log_{10} N_\mu]_{A_i}]. \end{aligned} \quad (7)$$

Note that  $\sigma^2[\log_{10} N_\mu]_{\text{mix}}$  does not depend on  $a$ . The dependence on  $b$  is implicit in the  $\sigma^2[\log_{10} N_\mu]_{A_i}$  term.

### 3. Simulation studies of $\log_{10} N_\mu$ moments

In this section we briefly describe the procedure adopted to produce simulated  $\log_{10} N_\mu$  distributions that are extensively employed in the following sections of this paper. The present discussion is complemented by Appendix A where more details about the simulations are given. Furthermore, in this section we also use the simulated showers to validate the  $\log_{10} N_\mu$  moment descriptions proposed in Section 2 and to study the energy evolution of  $\log_{10} N_\mu$  moments for a set of mass composition scenarios.

#### 3.1. Simulation technique

In our analysis we aim to assess the number of muons measured in UHECR experiments. A combination of detector technology, observatory altitude, spatial configuration of the detectors and analysis procedures determines the lateral distance range and the energy threshold of detectable muons. To avoid saturation of the detectors (close to the shower axis) and large statistical fluctuations (far from the shower axis), a fiducial lateral distance range is commonly defined to get the lateral distance function integrated. Therefore, the measured number of muons ( $N_\mu^{\text{meas}}$ ) is not the total number of muons at the ground but only a sample of them above an energy threshold and within a distance range.

In this paper  $N_\mu^{\text{meas}}$  is defined as the number of muons with energy above 0.2 GeV reaching the ground (1400 m above sea level, the Auger mean altitude) at a distance between 500 m and 2000 m from the shower axis. This choice is motivated by the design of the main current high energy cosmic ray experiments, for example, the Pierre Auger Observatory [19] and Telescope Array [20].

The muons spatial and energy distributions at the ground can be evaluated by CORSIKA [21] (version 7.4000), which is a full Monte Carlo code able to perform 3D shower simulations.  $N_\mu^{\text{meas}}$  could be determined by CORSIKA, in despite of its high computational cost [22]. CONEX [23] (version 2r4.37) is a very fast hybrid simulation code which combines full Monte Carlo with solutions of one-dimensional cascade equations. From CONEX simulations it is possible to determine the total number of muons at the ground above 1 GeV ( $N_\mu^{\text{tot}}$ ).

$N_\mu^{\text{tot}}$  and  $N_\mu^{\text{meas}}$  can be simultaneously obtained from full simulated showers (CORSIKA), allowing us to parametrize the relation between them. We propose the following parametrization:

$$N_\mu^{\text{meas}} = R(E, X_{\max}) \cdot N_\mu^{\text{tot}}, \quad (8)$$

where the conversion factor  $R$  should be determined for each primary and depends on the energy and  $X_{\max}$ . The parametrization of  $R(E, X_{\max})$  is explored in detail in Appendix A. The  $X_{\max}$  dependence of the factor  $R$  ensures that the parametrization takes into account the shower-to-shower fluctuations due to the variance of the first interaction depth. Furthermore, the most relevant physical

processes responsible for muons production in showers are reliably reproduced by the CONEX simulations, and consequently they should also be represented in  $N_\mu^{\text{meas}}$ . As shown in Appendix A, the  $N_\mu^{\text{meas}}$  distributions obtained based on the proposed parametrization are in very good agreement with the ones obtained from full Monte Carlo simulation.

The parametrization was done only for shower at 38° zenith angle. The zenith angle dependence can be taken into account by simulating other primaries with the corresponding arrival direction and by dividing the data in zenith angle intervals.

#### 3.2. Simulating $\log_{10} N_\mu$ moments

We generated 60,000 CONEX (version 2r4.37) showers with energies between  $10^{18.4}$  and  $10^{19.6}$  eV, for four primaries (proton, helium, nitrogen and iron) and two hadronic interaction models (EPOS-LHC [24] and QGSJetII-04 [25]). The showers are distributed uniformly in  $\log_{10}(E)$  and the zenith angle is fixed at 38°. From the  $R(E, X_{\max})$  parametrization of Appendix A, the CONEX showers were converted into a set of  $N_\mu^{\text{meas}}$ .

Fig. 1 shows the evolution of  $\langle \log_{10} N_\mu^{\text{meas}} \rangle$  with the primary mass for three energy intervals. Lines are the result of a linear fit which demonstrates the dependence of  $\langle \log_{10} N_\mu^{\text{meas}} \rangle$  with mass as proposed in Eq. (3). The fits resulted in  $D_A \simeq 0.034 - 0.037$  and  $a \simeq 6.64 - 7.70$ , with errors from the fit less than 0.0005 and 0.005, respectively.

The energy evolution of  $\langle \log_{10} N_\mu^{\text{meas}} \rangle$  is shown in Fig. 2, where one can note the linear behavior as proposed in Eq. (3). The fits resulted in  $D_E \simeq 0.915 - 0.928$ , with errors from the fit less than 0.0003. The energy evolution of  $\sigma[\log_{10} N_\mu^{\text{meas}}]$  is shown in Fig. 3. Note the flatness of  $\sigma[\log_{10} N_\mu^{\text{meas}}]$  and the coincidence of the  $\sigma[\log_{10} N_\mu^{\text{meas}}]$  constant value of iron initiated showers for both hadronic interaction models. These figures validate both assumptions made in Section 2 concerning  $\sigma[\log_{10} N_\mu^{\text{meas}}]$ .

The primary mass dependence of  $\sigma[\log_{10} N_\mu^{\text{meas}}]$  can be seen in Fig. 4 for three energy intervals and both hadronic interaction models. The dashed lines are the quadratic curves shown in Eq. (4) fitted to the points. The fits resulted in  $\sigma[\log_{10} N_\mu]_{\text{Fe}}$  being indeed nearly constant, varying from 0.0258 to 0.0275, with errors from the fits less than 0.003. The fit also resulted in  $b = 0.0024 \pm 0.0002$  for QGSJetII-04 and  $b = 0.0033 \pm 0.0003$  for EPOS-LHC. The simulations shown in this section confirmed all the assumptions made in Section 2.

### 4. Mass composition scenarios and the energy evolution of the $\log_{10} N_\mu$ moments

In this section we simulate the energy evolution of  $\log_{10} N_\mu^{\text{meas}}$  moments for six mass composition scenarios, which are defined by setting the fractions  $f_i(E)$  of the total flux corresponding to each particle with mass  $A_i$ . Given  $f_i(E)$  and  $A_i$  we can calculate  $\langle \log_{10} N_\mu^{\text{meas}} \rangle$  and  $\sigma[\log_{10} N_\mu^{\text{meas}}]$  as a function of energy using the procedure described in Sections 2 and 3.

The mass composition scenarios we used are divided in two groups. The first one includes the astrophysical motivated scenarios, which are labeled by the letter A. The second group includes two scenarios obtained from the  $X_{\max}$  distributions fit performed by the Pierre Auger Collaboration [11,16] and they are labeled by the letter X. Below, we present a brief description of the composition scenarios, which can be skipped by the reader that is familiar with the subject.

Scenario A1: This scenario proposes a pure proton flux. It was the first model proposed to explain the dip in the energy spectrum as the effect of pair-production in the propagation of the UHECR. This model is described in Refs. [5,8] and was also explored in Refs. [6,15] (labeled as Model B in Ref. [15]).

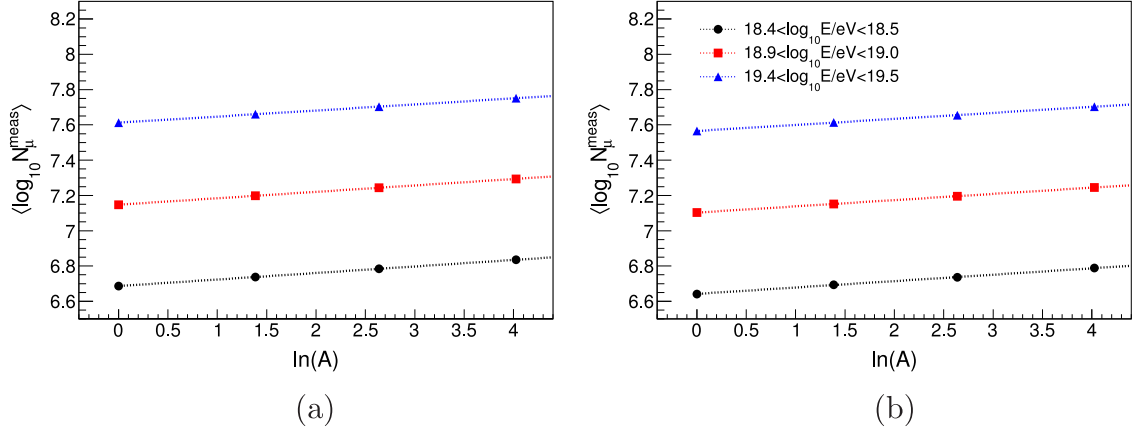


**Fig. 1.**  $\langle \log_{10} N_\mu^{\text{meas}} \rangle$  as a function of  $\ln(A)$  for both hadronic interaction models, (a) EPOS-LHC and (b) QGSJetII-04 and three energy intervals. The dotted lines are the results of the linear fit, represented in Eq. (3). The statistical error bars are smaller than the markers.

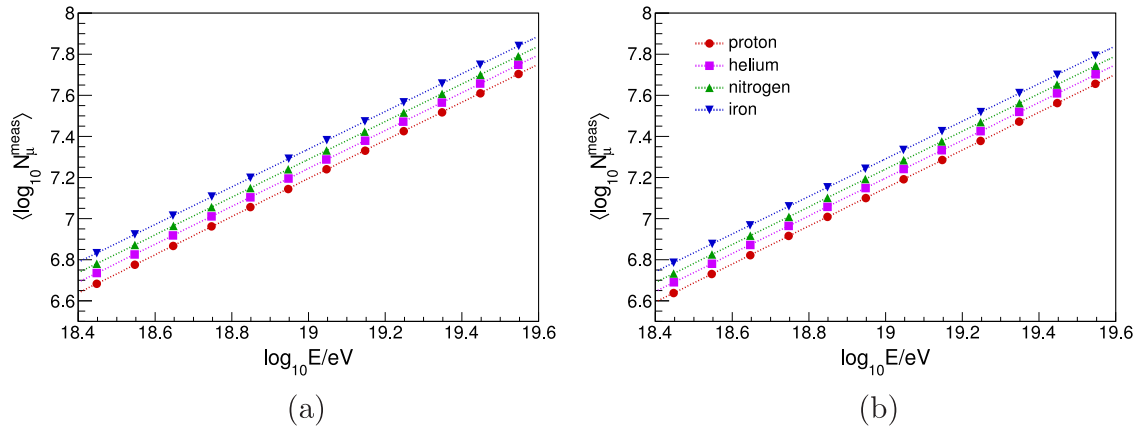


**Fig. 2.**  $\langle \log_{10} N_\mu^{\text{meas}} \rangle$  as a function of  $\log_{10}(E)$  for both hadronic interaction models, (a) EPOS-LHC and (b) QGSJetII-04, and four primaries (proton, helium, nitrogen and iron). The dotted lines are the results of the linear fit, represented in Eq. (3). The statistical error bars are smaller than the markers.

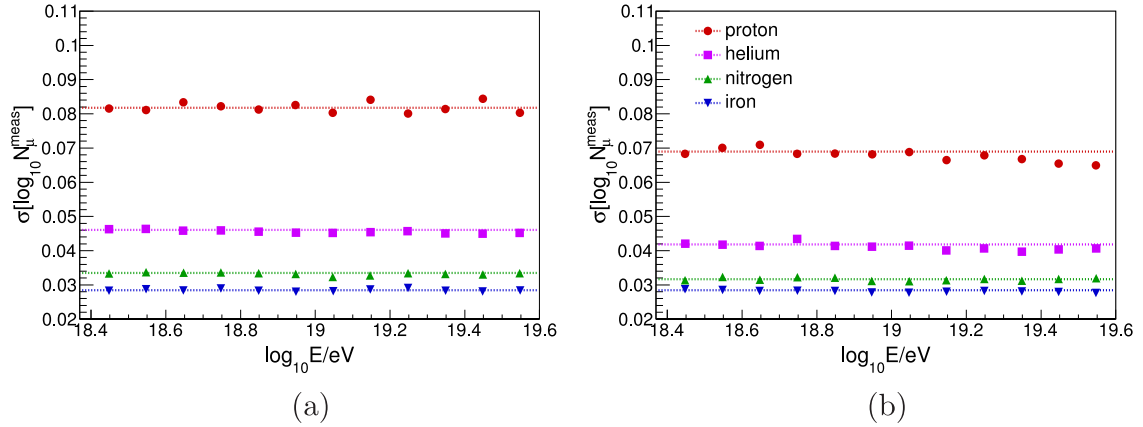


**Fig. 3.**  $\sigma[\log_{10} N_\mu^{\text{meas}}]$  as a function of  $\log_{10}(E)$  for both hadronic interaction models, (a) EPOS-LHC and (b) QGSJetII-04, and four primaries (proton, helium, nitrogen and iron). The dotted lines are the results of the fit of a constant energy function. The statistical error bars are smaller than the markers.

**Scenario A2:** This scenario assumes a mixed source composition with abundances similar to the data at lower energies. It was proposed by Allard et al. (labeled as Model A in Ref. [15]). In this model the ankle is explained as the transition in the predominance of the flux from the galactic to the extra-galactic component. The abundances are originally given for five groups of nuclei, however, in this paper the fluxes of the two heaviest groups were summed into the iron component.

**Scenario A3:** Biermann and de Souza [9] have proposed a model in which the observed cosmic ray energy spectrum from  $10^{15.0}$  to  $3 \times 10^{20.0}$  eV is explained by the galactic and only one extra-galactic source, the radio galaxy Cen A. In this model the element abundances from extra-galactic origin are similar to the galactic ones, but shifted up in energy because of the relativistic shock in the jet emanating from the active black hole. The abundances are originally given for six groups of nuclei, however, in this paper the flux of

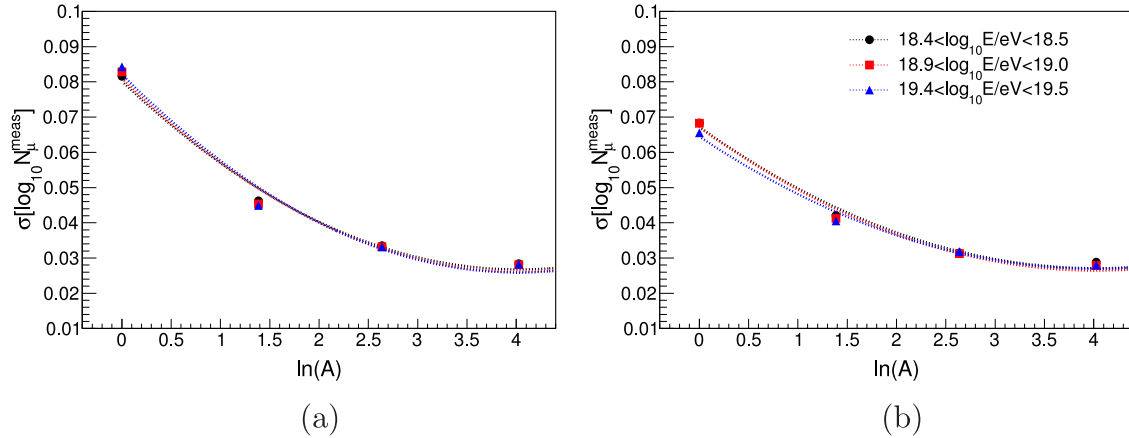


**Fig. 4.**  $\sigma[\log_{10} N_\mu^{\text{meas}}]$  as a function of  $\ln(A)$  for both hadronic interaction models, (a) EPOS-LHC and (b) QGSJetII-04, and three energy intervals. The dotted lines are the results of the fit of Eq. (4). The statistical error bars are smaller than the markers.

the element group Ne–S was summed into the nitrogen flux and the flux of the Cl–Mn group was summed into the iron group flux.

**Scenario A4:** The model proposed by Globus et al. [7] describes the whole cosmic ray spectrum by superposing a rigidity dependent galactic component and a generic extra-galactic component. This model gives an adequate description of the energy spectrum and the moments of the  $X_{\max}$  distribution measured by the Pierre Auger Observatory.

**Scenario X1:** It has been shown by the Pierre Auger Collaboration that the measured  $X_{\max}$  distributions can be well described by a combination of four components [11,16]. By fitting the  $X_{\max}$  simulated distributions to the data, the abundances of the separate components were obtained as a function of energy. This scenario is based on the abundances obtained by using the hadronic interaction model QGSJetII-04. However, the abundances obtained with Sibyll2.1 are also very close to the one we used. In order to minimize point-to-point fluctuations, we used here a smooth curve fitted to the fractions obtained in the Auger analysis [16].

**Scenario X2:** This scenario was obtained by fitting  $X_{\max}$  distributions measured by the Pierre Auger Observatory using showers simulated with the EPOS-LHC hadronic interaction model. The procedure is the same as the one adopted for Scenario X1.

The merging of components done for models A2 and A3 is necessary to allow us to use the parametrization elaborated in Section 3. Since we present in this paper only the analysis procedure, verified with simulations, this choice has no limiting consequence. Besides that, the systematic uncertainties of the abundances obtained from the scenarios are also going to be neglected here. Figs. 5 and 6 show the abundances for each scenario in the energy range from  $10^{18.4}$  to  $10^{19.6}$  eV as explained above. Scenario A1 is not shown because it assumes a 100% proton flux.

Fig. 7 shows the energy evolution of the  $\langle \log_{10} N_\mu^{\text{meas}} \rangle$  and  $\sigma[\log_{10} N_\mu^{\text{meas}}]$  for all mass composition scenarios. The error bars correspond to the one sigma fluctuation of the mean value considering the statistics from 3 years of AugerPrime data ( $3000 \text{ km}^2$  of muon detectors). The all particle flux was taken from Ref. [3]. Fig. 7a shows the mean normalized to the proton simulation for better visualization.

## 5. Discrimination between mass composition scenarios

Given the theoretical uncertainties on the  $N_\mu$  predictions and the systematic uncertainties on the energy reconstruction, the

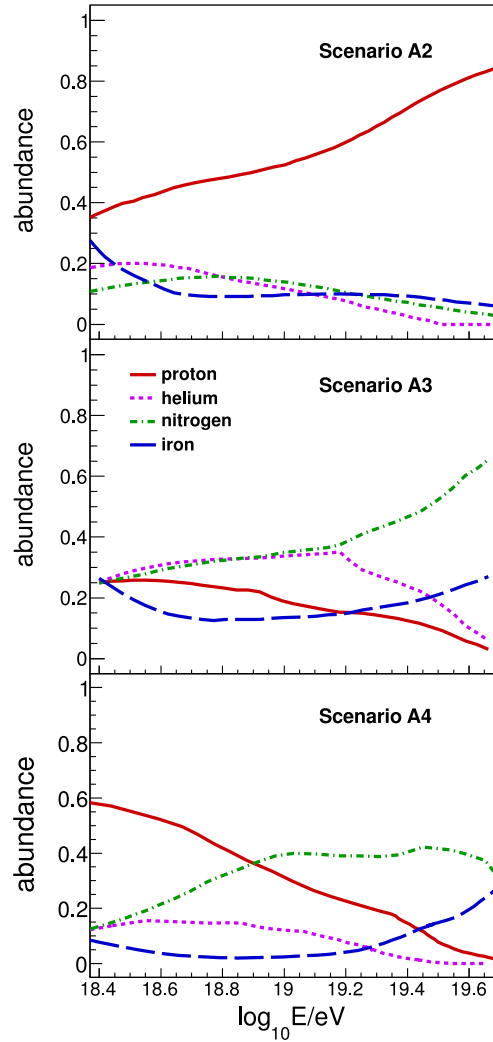


**Fig. 5.** The composition component abundances as a function of  $\log_{10}(E)$  for the mass composition scenarios A2, A3 and A4 (see text).

question we would like to answer in this section is how it is possible to discriminate between the mass composition scenarios shown above using the evolution of the  $\log_{10} N_\mu^{\text{meas}}$  moments with energy. Examining Fig. 7 it might seem easy to differentiate

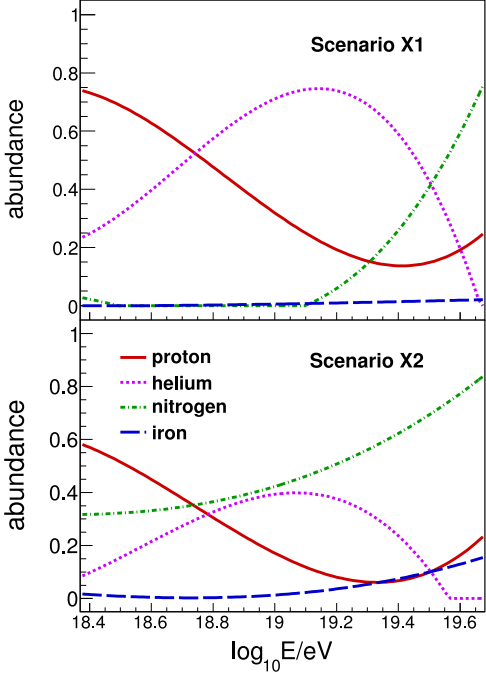


**Fig. 6.** The composition component abundances as a function of  $\log_{10}(E)$  for the mass composition scenarios X1 and X2 (see text).

the scenarios by using the absolute value or the evolution of the  $\log_{10} N_\mu^{\text{meas}}$  moments with energy. However, if we include in this figure the uncertainties in the hadronic interaction model and systematic in energy reconstruction the interpretation of the data is not straightforward.

**Fig. 8** shows how the uncertainties on the hadronic interaction model predictions and on the energy reconstruction influence the interpretation of the  $\langle \log_{10} N_\mu^{\text{meas}} \rangle$  in terms of composition. We show in this figure the extreme composition scenarios (A1 and A3), since the other four scenarios lie within them. In **Fig. 8a** we calculate  $\langle \log_{10} N_\mu^{\text{meas}} \rangle$  for scenarios A1 and A3 adding arbitrarily 20% more muons to the simulation predictions to mimic the theoretical uncertainties in the hadronic interaction model predictions [14]. Even the extreme models A1 and A3 would overlap if the uncertainty is considered. In **Fig. 8b** we calculate  $\langle \log_{10} N_\mu^{\text{meas}} \rangle$  for scenarios A1 and A3 and changed the simulated energy by  $\pm 15\%$  in order to evaluate the effect of the systematic uncertainty in the energy reconstruction. Once more it is clear that even the extreme

scenario cases cannot be distinguished anymore. Moreover a combination of both uncertainties in the  $N_\mu$  predictions and energy applied to this analysis would make the discrimination between the scenarios even harder. The conclusion is clear: the measurement of  $N_\mu$  does not lead to a straightforward interpretation of the data in terms of composition if all the uncertainties are considered.

It is worthwhile to remember here how the interpretation of the  $X_{\max}$  measurement is done. The Pierre Auger Collaboration, for example, fits  $f_i$  to the measured  $X_{\max}$  distribution in bins of energy [16]. The calculation of  $f_i$  depends on simulation and therefore on the hadronic interaction model. However, because the electromagnetic cascade of the shower dominates the determination of the  $X_{\max}$  position, the discrepancy between the hadronic interaction model  $X_{\max}$  predictions is minimized. The difference in  $\langle X_{\max} \rangle$  is at most  $20 \text{ g/cm}^2$  and in  $\sigma[X_{\max}]$  is  $6 \text{ g/cm}^2$  for the most often used hadronic interaction models (EPOS-LHC, Sibyll2.1 and QGSjetII-04) [11]. Given the small differences in the predictions of  $X_{\max}$  and its consistency with data, the fit of  $f_i$  leads to acceptable differences in the calculation of  $f_i$  for different hadronic interaction models and then to mass composition scenarios which are physically consistent.

Unfortunately, the same procedure cannot be applied to  $N_\mu$  because of the discrepancies between the hadronic interaction model predictions and the inconsistency between simulations and data. It is known that the simulations are off by at least 20% in the calculation of  $N_\mu$  [13,14]. A fit of  $f_i$  based on the  $N_\mu$  distribution would lead to non-physical results. Therefore we propose an alternative analysis to discriminate between composition scenarios. The idea is to fix  $f_i$ , choosing a mass composition scenario, and fit the data with the energy evolution of  $\log_{10} N_\mu^{\text{meas}}$  moments to search for the scenarios which better describe the data.

If the composition ( $f_i$ ) were known by an independent measurement, this procedure would allow us to calculate  $a$  and  $b$  and constrain the hadronic interaction models by limiting fundamental properties of the interactions. This hypothesis needs to be explored further by using the results from the  $X_{\max}$  measurement to fix  $f_i$ .

We propose here a procedure that allows a statistically robust test of composition scenarios against data. The method starts by using the model proposed in [Section 2](#) to predict the energy evolution of  $\langle \log_{10} N_\mu^{\text{meas}} \rangle$  and  $\sigma[\log_{10} N_\mu^{\text{meas}}]$  for a given composition scenario. Here, all the parameters of the model are fixed, except  $a$  and  $b$ . The next step is to compare these predictions with data and find the values of  $a$  and  $b$  which make the model most similar to the data. This can be done by a  $\chi^2$  minimization. The minimal values of  $\chi^2$  determine which scenario best describes the data. Since  $a$  and  $b$  take all the hadronic interaction model dependence, the

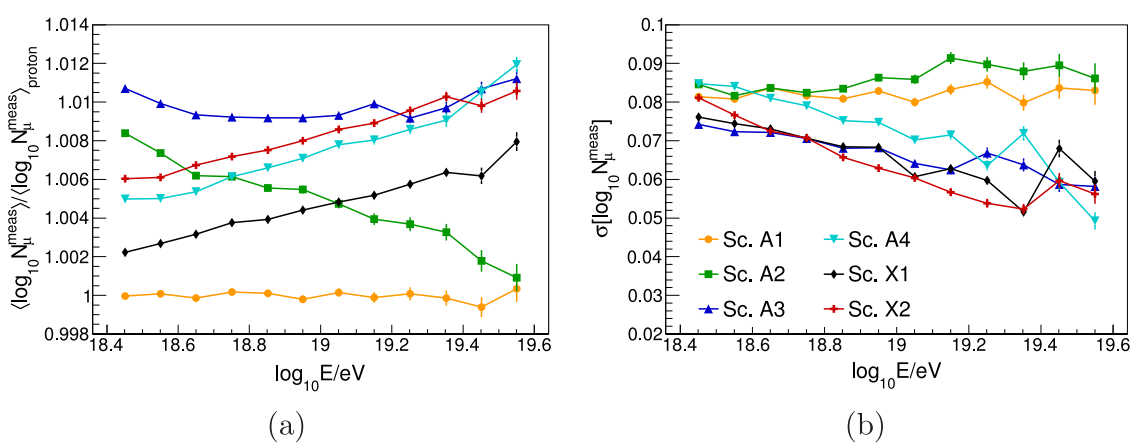


**Fig. 7.** Energy evolution of (a)  $\langle \log_{10} N_\mu^{\text{meas}} \rangle$  and (b)  $\sigma[\log_{10} N_\mu^{\text{meas}}]$  for the six composition scenarios described in the text. The values of  $\langle \log_{10} N_\mu^{\text{meas}} \rangle$  are divided by the corresponding value of pure proton composition for better visualization. The hadronic interaction model used was EPOS-LHC.

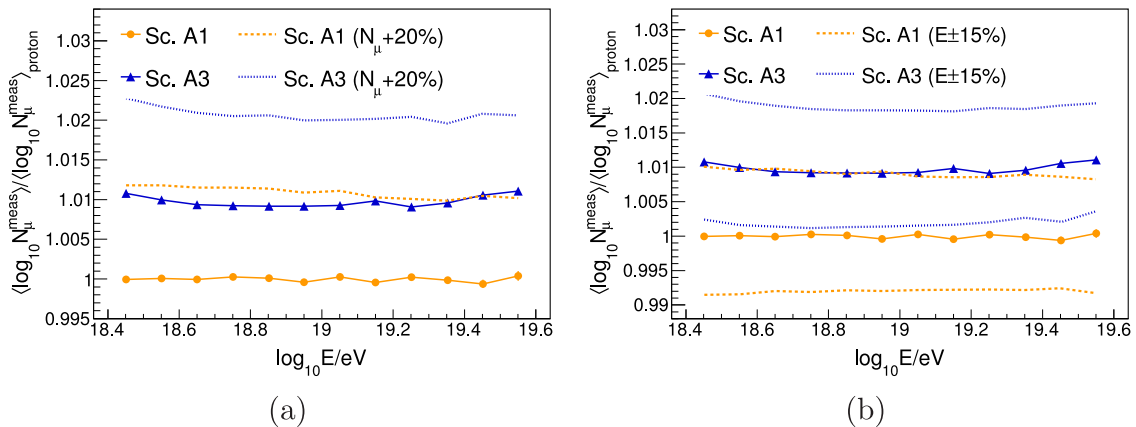


**Fig. 8.** Energy evolution of  $\langle \log_{10} N_\mu^{\text{meas}} \rangle$  for 2 mass composition scenarios, A1 and A3. The dashed lines show the effects of (a) an increase of 20% in the  $N_\mu$  and (b) a variation of  $\pm 15\%$  in energy. The values of  $\langle \log_{10} N_\mu^{\text{meas}} \rangle$  are divided by the corresponding value of pure proton composition for better visualization. The hadronic interaction model used was EPOS-LHC.

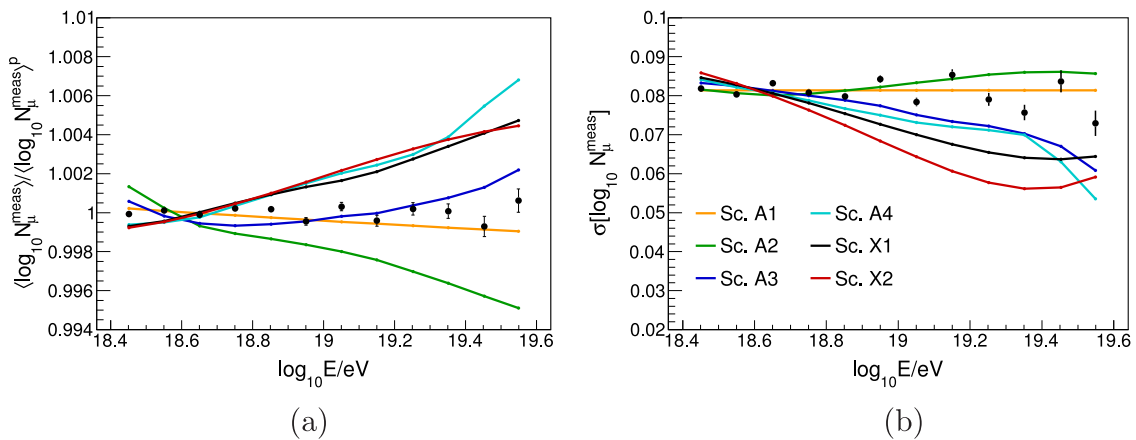


**Fig. 9.** Black dots show the simulated (a)  $\langle \log_{10} N_\mu^{\text{meas}} \rangle$  and (b)  $\sigma[\log_{10} N_\mu^{\text{meas}}]$  using scenario A1 as the true one. The colored lines show the results of the fit for each one of the test scenarios. The values of  $\langle \log_{10} N_\mu^{\text{meas}} \rangle$  are divided by the corresponding value of pure proton composition for better visualization.

composition scenario can be tested independently of hadronic interaction model limitations.

We explored this analysis proposal by choosing a composition scenario as if it would represent the true measurement, and we name it *true scenario*. We generate the  $\log_{10} N_\mu$  moments as a function of energy for the *true scenario* using the simulation described in Section 3 in order to emulate the real data. Here, the energy bins are defined by 12 intervals of width  $\Delta \log_{10}(E/\text{eV}) = 0.1$ , from  $10^{18.4}$  to  $10^{19.6}$  eV. This choice is mainly motivated by the Auger experimental acceptance, which reaches a 100% efficient trigger probability around  $10^{18.4}$  eV [26]. The number of events in each bin is determined by considering 3 years of data taken by the full array of Auger, following the energy spectrum of Ref.[3].

It is important to note that the simulations used here do not take into account any detector effects or zenith angle dependence. Although in this paper we do not intend to approach these issues because the focus here are on the general aspects of the analysis, it is clear that in practical applications of the method one should deal with these experimental difficulties. The detector effects, like resolution and limited acceptance, could be addressed by unfolding or unbiasing techniques once the detector response is well known. One example of these process is the Auger analysis of  $X_{\max}$  moments [11]. The zenith angle dependence could be addressed in a conservative approach by dividing the data in zenith angle intervals or by correcting the data using a *constant intensity cut* (CIC) method [27–29]. This later class of method has been successfully used, for example, to determine the shower size

parameter by Pierre Auger [30] and KASCADE-Grande Collaboration [31] and to correct the  $N_\mu$  parameter by KASCADE-Grande Collaboration [32]. The systematics uncertainties from these procedure are usually small (<10%) and should be taken into account in a realistic approach of our method.

In next step, we perform a  $\chi^2$  fit using the model described by Eqs. (5) and (7), with  $a$  and  $b$  as free parameters of the fit, for all the composition scenarios. The scenarios which are not the true one are named *test scenarios*. Fig. 9 shows one realization of these fits in which scenario A1 was used as the *true scenario* to generate the black dots. The fit of the  $\langle \log_{10} N_\mu^{\text{meas}} \rangle$  with energy (Fig. 9) sets the best value of  $a$  and the minimal value of  $\chi^2(a)$ . The fit of the  $\sigma[\log_{10} N_\mu^{\text{meas}}]$  with energy (Fig. 9) sets the best value of  $b$  and the minimal value of  $\chi^2(b)$ . In all fits,  $D_E = 0.920$ ,  $D_A = 0.0354$  and  $\sigma[\log_{10} N_\mu]_{\text{Fe}} = 0.0265$ . Each line in Fig. 9 is the fit of one out of the six composition scenarios. We compared all scenarios (*test scenarios*) to the *true scenario*.

A simple  $\chi^2$  comparison finds the *test scenarios* which best fit the data generated with the *true scenario*. The average value of  $\chi^2$  as a function of the fitted parameters  $a$  and  $b$  is shown in Fig. 10 for a set of 500 realizations. In this case, it is clear that the scenario A1 better describes the  $\langle \log_{10} N_\mu^{\text{meas}} \rangle$  and  $\sigma[\log_{10} N_\mu^{\text{meas}}]$  evolution with energy because of the smaller values of  $\chi_{\min}^2(a)$  and  $\chi_{\min}^2(b)$ . Fig. 11 shows the plots of  $\chi_{\min}^2(a)$  vs  $\chi_{\min}^2(b)$  for all six scenarios as the *true scenarios*. The error bars represent one standard deviation around the mean for 500 realizations. All scenarios,

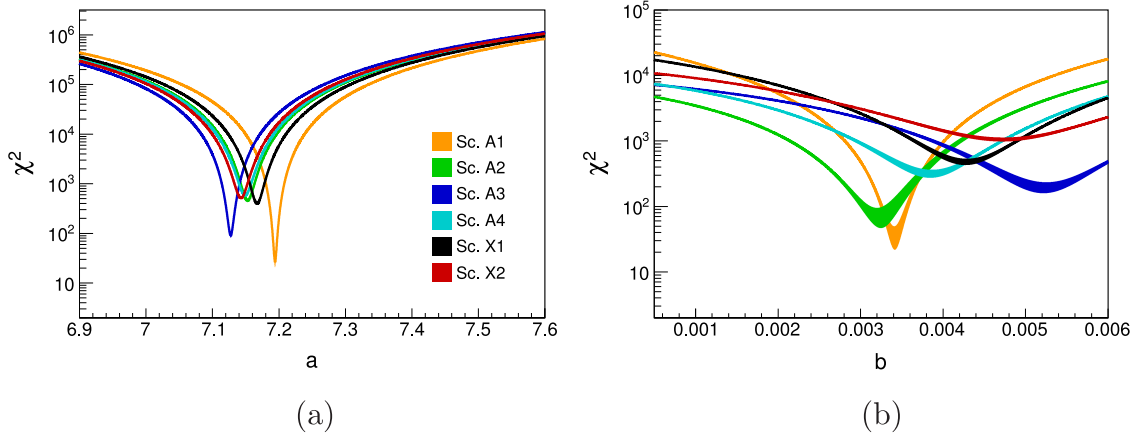


**Fig. 10.**  $\chi^2$  as a function of the parameters  $a$  (a) and  $b$  (b) for all the scenarios. The scenario A1 is the *true scenario*. The colored bands represent one standard deviation around the mean for a set of 500 realizations.

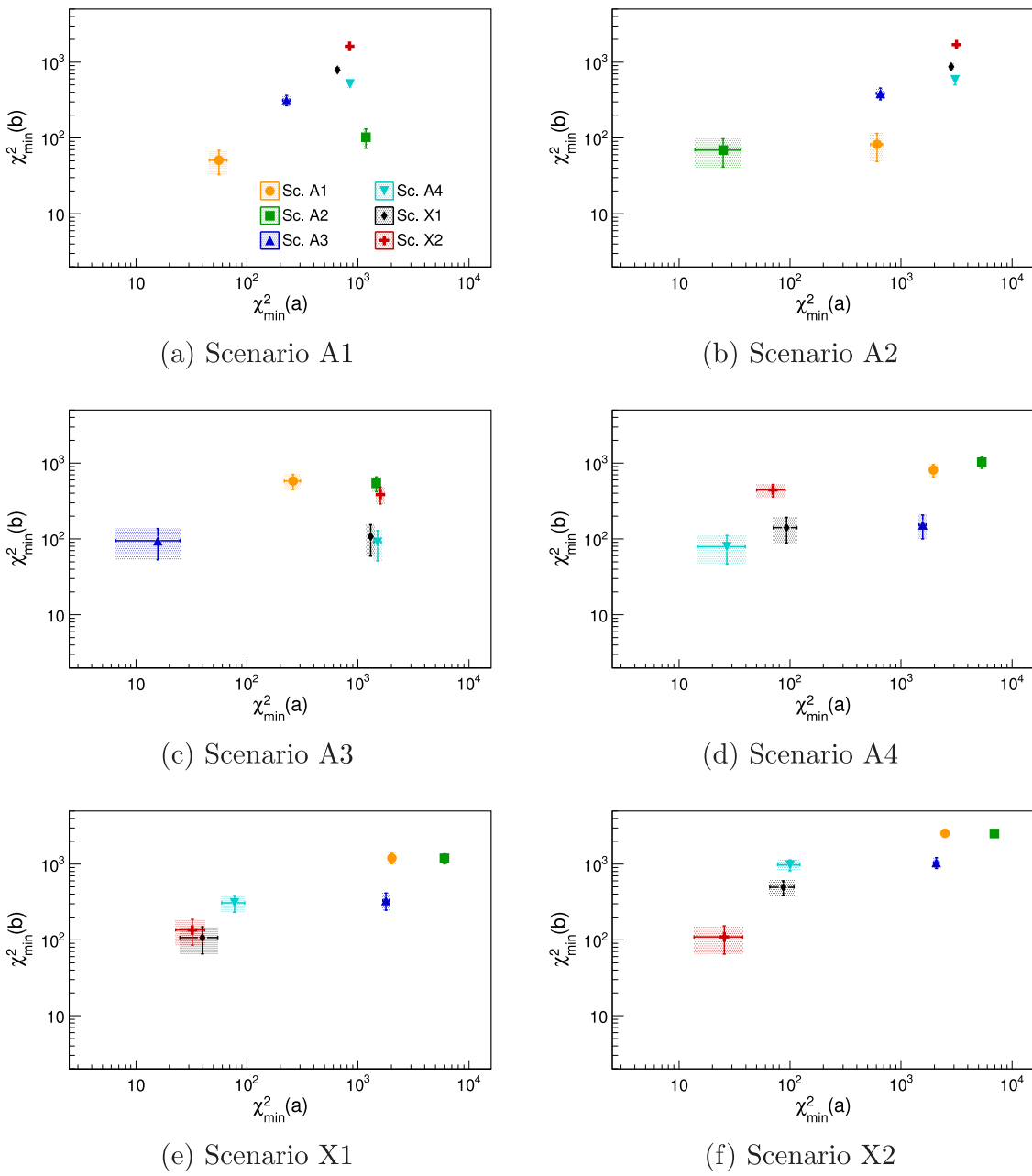


**Fig. 11.**  $\chi^2_{\min}(a)$  vs  $\chi^2_{\min}(b)$  for all composition scenarios.

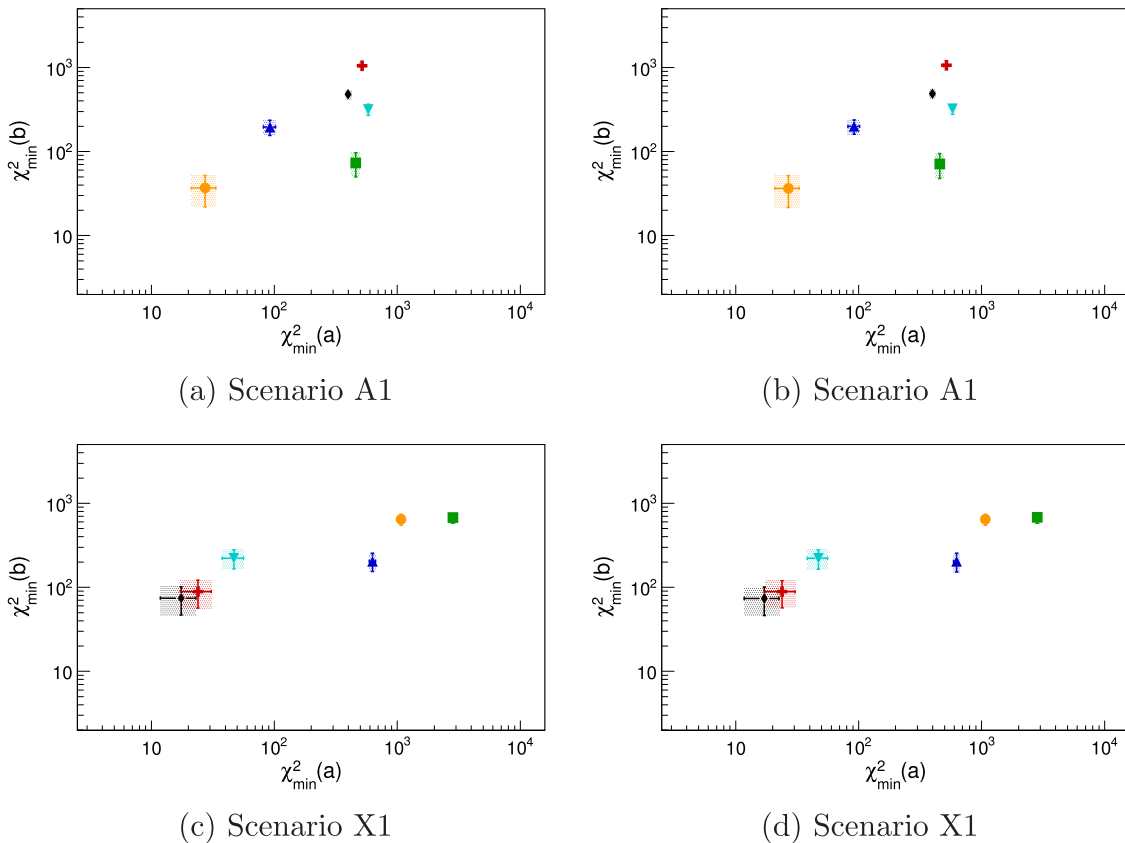


**Fig. 12.**  $\chi^2_{\min}(a)$  vs  $\chi^2_{\min}(b)$  for the true scenario A1 with (a)  $\alpha_{N_\mu} = 1.3$  and (b)  $\alpha_{N_\mu} = 1.6$  and for the true scenario X1 with (c)  $\alpha_{N_\mu} = 1.3$  and (d)  $\alpha_{N_\mu} = 1.6$  (see text).

except in X1 case, can be discriminated by the smallest  $\chi^2_{\min}(a)$  and  $\chi^2_{\min}(b)$ . In other words, the *true scenario* is the one with the  $\chi^2_{\min}(a) - \chi^2_{\min}(b)$  point closer to the left-down corner. Note that only  $\chi^2_{\min}(a)$  or only  $\chi^2_{\min}(b)$  cannot alone discriminate most of the scenarios. In the case of X1 as *true scenario* one can see that, even if it is not possible to discriminate scenario X1 and X2, it is still possible to discriminate the  $X_{\max}$  scenarios from the astrophysical ones.

### 5.1. Sensitivity to the systematic uncertainties on energy scale and absolute number of muons

As mentioned above, the greatest obstacles in interpreting  $N_\mu$  data currently are the systematic uncertainties in the theoretical description and reconstruction of air showers. In this section we demonstrate that the procedure proposed in the previous section to discriminate between composition scenarios is stable under systematic changes of absolute  $N_\mu$  prediction and of energy scale.

The systematic uncertainties in  $N_\mu$  scale were tested by applying the rescaling factor  $\alpha_{N_\mu}$  in  $N_\mu^{\text{meas}}$  generated by simulations. The examination of Eq. (3) shows that a rescaling factor on  $N_\mu$  corresponds to an additive term in  $a$ . This is how the systematic effect on  $N_\mu^{\text{meas}}$  is incorporated in the simple description of  $\langle \log_{10} N_\mu^{\text{meas}} \rangle$ . Eq. (4) shows that  $b$  does not depend on  $\alpha_{N_\mu}$ . If only  $\langle \log_{10} N_\mu^{\text{meas}} \rangle$  changes by an additive term when  $\alpha_{N_\mu}$  is applied, it is clear that  $\chi^2_{\min}(a)$  and  $\chi^2_{\min}(b)$  are independent of  $\alpha_{N_\mu}$ . Fig. 12 shows the values of  $\chi^2_{\min}(a)$  and  $\chi^2_{\min}(b)$  for true scenarios A1 and X1 and  $\alpha_{N_\mu} = 1.3$  and 1.6, as examples. One can see that the values of  $\chi^2_{\min}(a)$  and  $\chi^2_{\min}(b)$  are stable under systematic changes in  $N_\mu^{\text{meas}}$ .

The energy scale effect was tested by including a rescaling factor  $\alpha_E$  in simulated energy of each shower. The same analysis of Eqs. (3) and (4) reveals that  $a$  and  $b$  accommodate the sys-

tematic effects in energy as additive terms. All additive terms are canceled in the  $\chi^2$  comparison resulting in the independence of the conclusions under systematic effects. In Fig. 13 we show the  $\chi^2_{\min}(a)$  and  $\chi^2_{\min}(b)$  for true scenarios A1 and X1 and for  $\alpha_E = 0.85$  and 1.15, which represents a systematic uncertainties of 15% in energy. Again, it can be observed that the values of  $\chi^2_{\min}(a)$  and  $\chi^2_{\min}(b)$  would not lead to a different conclusion, and therefore, the results of the method would be stable under energy shifts.

## 6. Conclusion

In this paper, we have analyzed the muon content of air showers, proposed a parametrization of the first two moments of the number of muons with energy and primary particle mass and showed how the measured mean and  $\sigma$  of  $\log_{10} N_\mu$  can be used to discriminate between composition scenarios.

We proposed a model to describe  $\langle \log_{10} N_\mu^{\text{meas}} \rangle$  and  $\sigma[\log_{10} N_\mu^{\text{meas}}]$  as a function of energy and primary particle mass ( $A$ ). This model was conceived to keep the most relevant hadronic interaction uncertainties concentrated in only two parameters ( $a$  and  $b$ ). We have validated the model with Monte Carlo simulation of the air shower and its capability to describe the  $\log_{10} N_\mu^{\text{meas}}$  moments was proven.

Six composition scenarios were considered. The particle flux predicted by these scenarios was transformed into the corresponding  $\langle \log_{10} N_\mu^{\text{meas}} \rangle$  and  $\sigma[\log_{10} N_\mu^{\text{meas}}]$  evolution with energy. The  $\langle \log_{10} N_\mu^{\text{meas}} \rangle$  and  $\sigma[\log_{10} N_\mu^{\text{meas}}]$  evolution with energy was fitted using the proposed parametrization. A comparison of the  $\langle \log_{10} N_\mu^{\text{meas}} \rangle$  and  $\sigma[\log_{10} N_\mu^{\text{meas}}]$  model using a simple  $\chi^2$  test allows the discrimination between the scenarios. The discrimination is effective even considering the systematic uncertainties on the  $N_\mu$  prediction and on energy scale uncertainty.

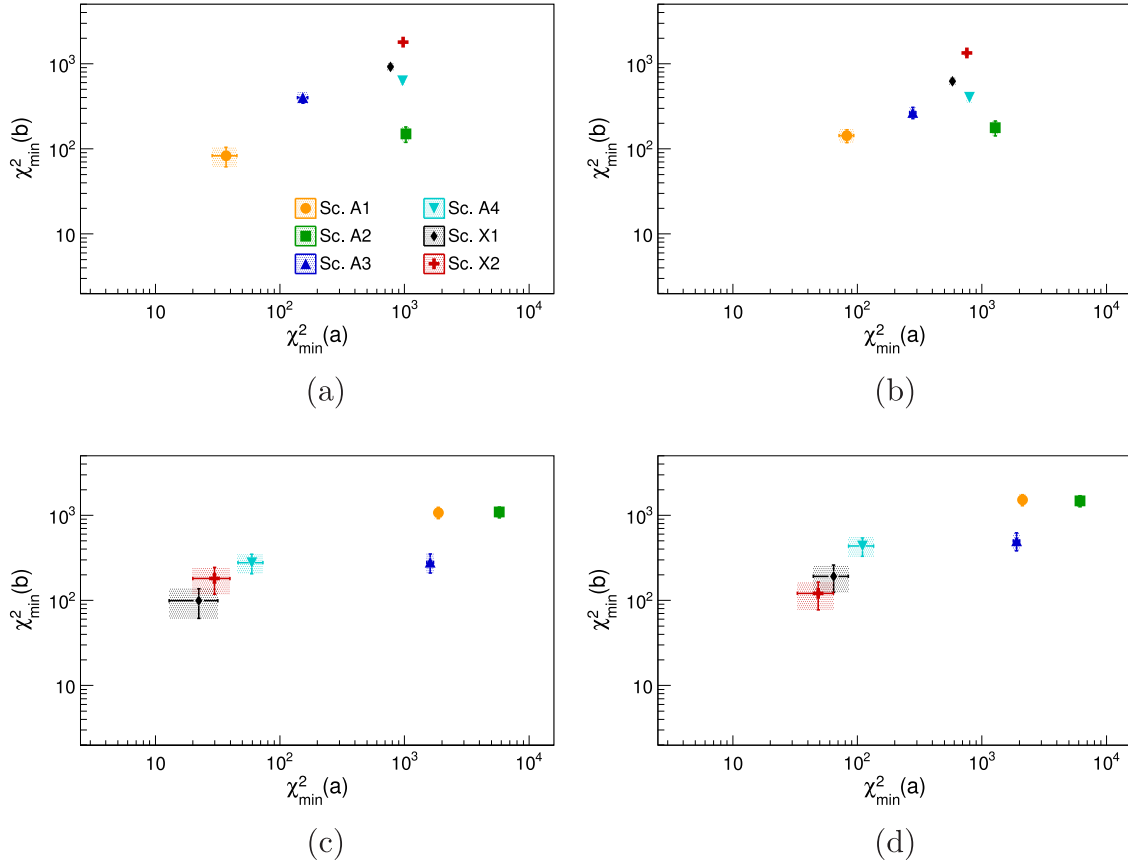


**Fig. 13.**  $\chi^2_{\min}(a)$  vs  $\chi^2_{\min}(b)$  for the true scenario A1 with (a)  $\alpha_E = 0.85$  and (b)  $\alpha_E = 1.15$  and for the true scenario X1 with (c)  $\alpha_E = 0.85$  and (d)  $\alpha_E = 1.15$  (see text).

The effect of the systematic in the  $N_\mu$  number and energy reconstruction was studied for constant values of the uncertainty with energy. This choice is justified by the narrow energy interval used in the analysis. Abrupt changes of the systematic uncertainties with energy could change the conclusion drawn here since  $\log_{10} N_\mu^{\text{meas}}$  is assumed to be fixed in the proposed model.

The upgrade of Telescope Array [33] and Pierre Auger Observatory [34], to be constructed in the next few years, will for the first time allow precise measurements of the muon component of air showers for energies above  $10^{18}$  eV. This will open up a new window of analyses and tests in astroparticle physics. Once data is acquired, the parametrization proposed here could be tested and if proven to be right, the analysis method proposed in Section 5 could be used to find the most probable composition scenario in the energy range from  $10^{18.4}$  to  $10^{19.6}$  eV.

## Acknowledgments

We thank Stéphane Coutu and Carola Dobrigkeit for the review of the manuscript on behalf of the Pierre Auger Collaboration. RRP thanks the financial support given by FAPESP (2014/10460-1). RC and MP gratefully acknowledge the financial support by Fundação para a Ciência e Tecnologia (SFRH/BPD/73270/2010) and OE, FCT-Portugal, CERN/FIS-NUC/0038/2015. VdS thanks the support of the Brazilian population via CNPq and FAPESP (2010/07359-6, 2014/19946-4).

## Appendix A. Parametrization of $R(E, X_{\max})$

As mentioned in Section 3, the parametrization of  $R(E, X_{\max})$  can be done by means of full air shower simulations. In this paper, we choose CORSIKA [21] as the full Monte Carlo code.

First, a set of 200 CORSIKA (version 7.4000) showers for each primary (proton, helium, nitrogen and iron), fixed energy ( $E = 10^{18.5}, 10^{19.0}, 10^{19.5}$  eV) and high energy hadronic interaction model (EPOS-LHC [24] and QGSJetII-04 [25]) were generated. The low energy hadronic interaction model is Fluka [35] in all cases. Furthermore, the zenith angle was set fixed to  $38^\circ$  for all showers. This is clearly a simplification, and then it should be stressed that, in a more realistic analysis, the  $N_\mu$  zenith angle dependence must be treated.

In Fig. A.1 the factor  $R$  is shown as a function of  $X_{\max}$  for all primaries, one primary energy,  $10^{19.0}$  eV, and one hadronic interaction model, EPOS-LHC. The observed behavior suggests a linear parametrization of the form,

$$R(E, X_{\max}) = p_1(E) \cdot X_{\max} + p_0(E), \quad (\text{A.1})$$

where  $p_0$  and  $p_1$  have to be also parametrized as a function of energy. The values of  $p_0$  and  $p_1$  for each primary and energy were determined from the linear fit, shown in Fig. A.1 by a dotted red line.

In Fig. A.2  $p_0$  and  $p_1$  are shown as a function of logarithmic energy for all primaries and the hadronic interaction model EPOS-LHC, as an example. Again, we are able to perform a linear parametrization of  $p_0$  and  $p_1$  as a function of  $\log_{10}(E)$ , in the form

$$\begin{aligned} p_0(E) &= \alpha_0 \cdot \log_{10}(E/\text{eV}) + \beta_0, \\ p_1(E) &= \alpha_1 \cdot \log_{10}(E/\text{eV}) + \beta_1. \end{aligned} \quad (\text{A.2})$$

The dotted lines in Fig. A.2 show the function from Eq. (A.2) fitted to the point obtained from CORSIKA simulations. The values of  $\alpha_0$ ,  $\beta_0$ ,  $\alpha_1$  and  $\beta_1$  for all primaries and hadronic interaction models are presented in Table A.1.

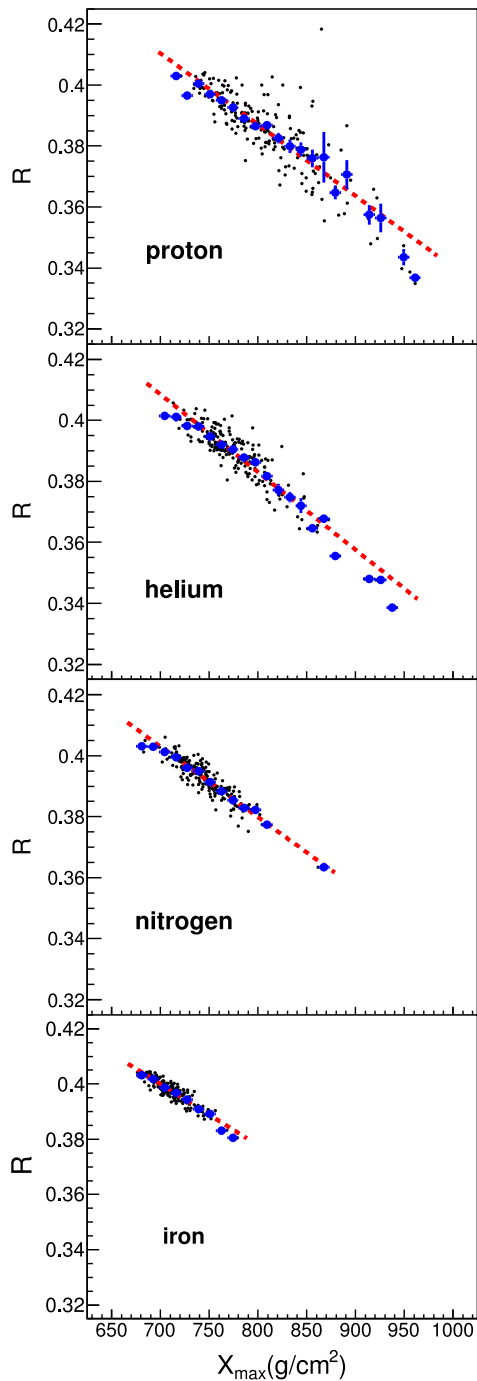


**Fig. A.1.** Conversion factor  $R$  as a function of  $X_{\max}$  for  $E = 10^{19.0}$  eV showers with EPOS-LHC as hadronic interaction model. The black dots are individual showers, the blue circles are the profile and dotted red line is the linearfit. (For interpretation of the references to color in this figure legend, the reader is referred to the web version of this article.)

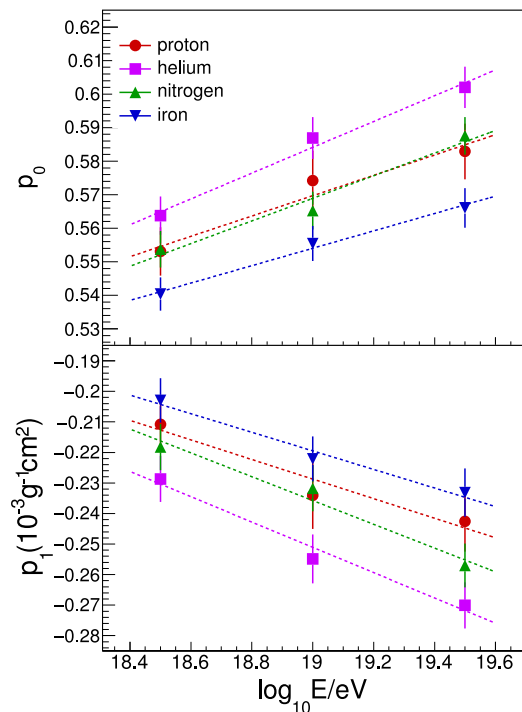


**Fig. A.2.**  $p_0$  and  $p_1$  as a function of  $\log_{10}(E)$  (see text) for EPOS-LHC as the hadronic interaction model. The dashed lines are the linear fits represented in Eq. (A.2).

A comparison between  $\log_{10} N_{\mu}^{\text{meas}}$  distributions achieved directly from CORSIKA showers and from the simulated method described in this work can be seen in Fig. A.3. The energy is fixed at  $E = 10^{19.0}$  eV and the hadronic interaction model is EPOS-LHC. The discrepancies in the mean values and in the  $\sigma$  of the distributions are less than 2% and 5% respectively, for any combination of primary and hadronic interaction model. Indeed, considering the differences between the approaches assumed by both software, CORSIKA and CONEX, these observed discrepancies are really satisfactory. Among the several physical effects which are treated differently we can highlight the lack of geomagnetic field and muon multiple scattering in CONEX.

Although there is a small discrepancy between our method's and CORSIKA's  $\log_{10} N_{\mu}^{\text{meas}}$  distributions, we do not expect to find any loss in the development of this paper. This can be assured because the method proposed here is not dependent on the comparison between our simulations and any other set of simulated showers.

**Table A1**  
Fitted parameters  $\alpha_0$ ,  $\beta_0$ ,  $\alpha_1$  and  $\beta_1$  given in Eq. (A.2).

Had. int. model	Primary	$\alpha_0$	$\beta_0$	$\alpha_1(10^{-5} \text{ g}^{-1}\text{cm}^2)$	$\beta_1(10^{-5} \text{ g}^{-1}\text{cm}^2)$
EPOS-LHC	proton	0.0303	-0.00635	-3.20	38.0
	helium	0.0385	-0.147	-4.14	53.6
	nitrogen	0.0337	-0.0721	-3.90	50.5
	iron	0.0259	0.0613	-3.04	35.8
QGSJetII-04	proton	0.0216	0.130	-2.04	17.3
	helium	0.0143	0.264	-1.20	1.35
	nitrogen	0.0167	0.209	-1.60	9.94
	iron	0.0245	0.0427	-2.99	38.5

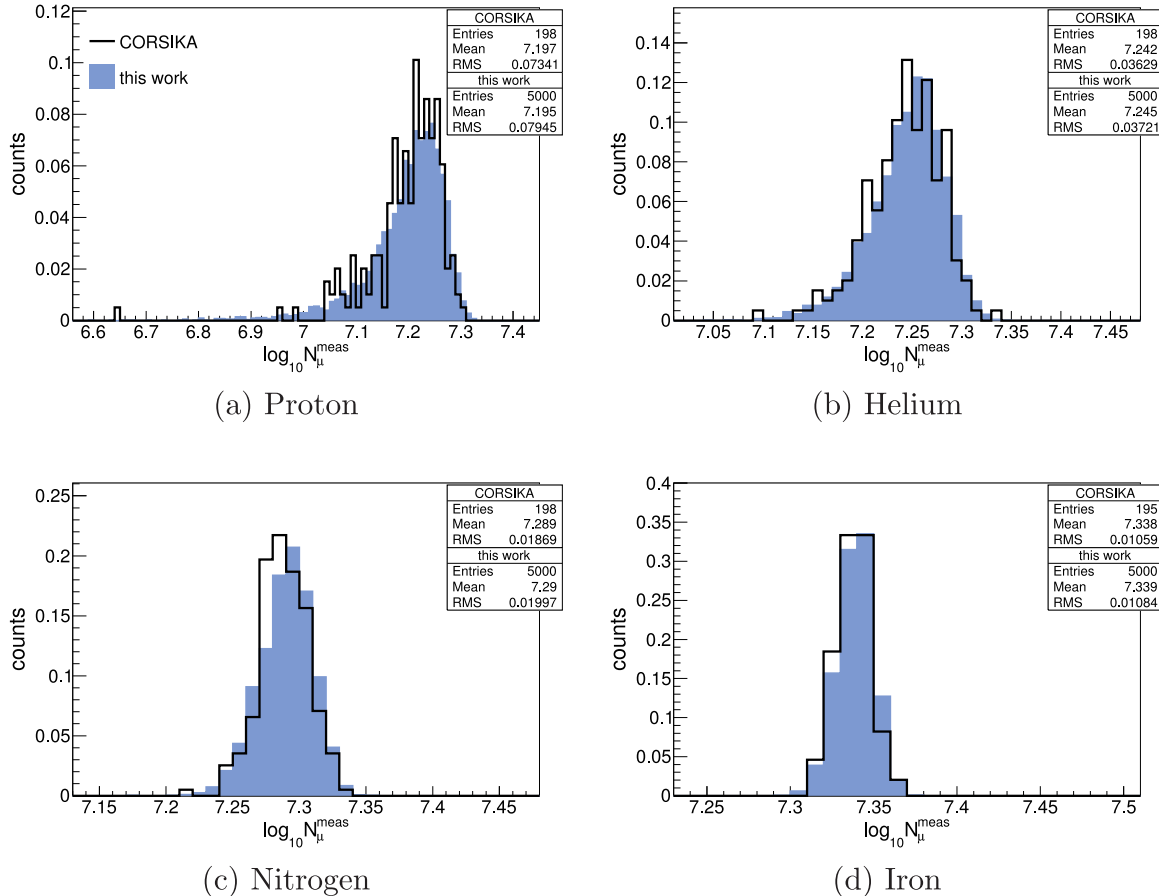


**Fig. A.3.** Comparison between the normalized  $\log_{10} N_\mu^{\text{meas}}$  distributions generated by CORSIKA and by this work's algorithm. The energy is  $E = 10^{19.0}$  eV and the hadronic interaction model is EPOS-LHC. The primary particles are (a) proton, (b) helium, (c) nitrogen and (d) iron.

## References

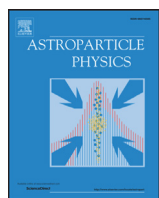
- [1] R. Abbasi (The HiRes Collaboration), Measurement of the flux of ultra high energy cosmic rays by the stereo technique, *Astropart. Phys.* 32 (1) (2010) 53–60. [0904.4500](#), doi:[10.1016/j.astropartphys.2009.06.001](#).
- [2] J. Abraham (The Pierre Auger Collaboration), Measurement of the energy spectrum of cosmic rays above  $10^{18}$  eV using the Pierre Auger Observatory, *Phys. Lett. B* 685 (4–5) (2010) 239–246. [1002.1975](#), doi:[10.1016/j.physletb.2010.02.013](#).
- [3] A. Schulz, **Measurement of the Energy Spectrum of Cosmic Rays above  $3 \times 10^{17}$  eV with the Pierre Auger Observatory**, in: *Proceedings of the 33rd ICRC*, 2013.
- [4] T. Abu-Zayyad (The Telescope Array Collaboration), The cosmic-ray energy spectrum observed with the surface detector of the telescope array experiment, *Astrophys. J.* 768 (1) (2013) L1, doi:[10.1088/2041-8205/768/1/L1](#).
- [5] D. Allard, et al., UHE nuclei propagation and the interpretation of the ankle in the cosmic-ray spectrum, *Astron. Astrophys.* 443 (2005) L29–L32. [astro-ph/0505566](#), doi:[10.1051/0004-6361:200500199](#).
- [6] V. Berezinsky, A. Gazizov, S. Grigorieva, On astrophysical solution to ultrahigh energy cosmic rays, *Phys. Rev. D* 74 (4) (2006) 043005, doi:[10.1103/PhysRevD.74.043005](#).
- [7] N. Globus, D. Allard, E. Parizot, A complete model of the CR spectrum and composition across the Galactic to Extragalactic transition, *Phys. Rev. D* 92 (2015) 021302(R). [1505.01377](#), doi:[10.1103/PhysRevD.92.021302](#).
- [8] V. Berezinsky, A. Gazizov, S. Grigorieva, Dip in UHECR spectrum as signature of proton interaction with CMB, *Phys. Lett. B* 612 (3–4) (2005) 147–153, doi:[10.1016/j.physletb.2005.02.058](#).
- [9] P.L. Biermann, V. de Souza, Centaurus a: the extragalactic source of cosmic rays with energies above the knee, *Astrophys. J.* 746 (1) (2012) 72. [1106.0625](#), doi:[10.1088/0004-637X/746/1/72](#).
- [10] J. Abraham (The Pierre Auger Collaboration), *Phys. Rev. Lett.* 104 (9) (2010) 091101, doi:[10.1103/PhysRevLett.104.091101](#).
- [11] A. Aab (The Pierre Auger Collaboration), Depth of maximum of air-shower profiles at the Pierre Auger Observatory. I. measurements at energies above  $10^{17.8}$  eV, *Phys. Rev. D* 90 (12) (2014) 122005, doi:[10.1103/PhysRevD.90.122005](#).
- [12] K.-H. Kampert, M. Unger, Measurements of the cosmic ray composition with air shower experiments, *Astropart. Phys.* 35 (10) (2012) 660–678. [1201.0018](#), doi:[10.1016/j.astropartphys.2012.02.004](#).
- [13] G.R. Farrar, **The muon content of hybrid events recorded at the Pierre Auger Observatory**, in: *Proceedings of the 33rd ICRC*, 2013.
- [14] A. Aab (The Pierre Auger Collaboration), Muons in air showers at the Pierre Auger Observatory: mean number in highly inclined events, *Phys. Rev. D* 91 (2015) 032003, doi:[10.1103/PhysRevD.91.032003](#).
- [15] D. Allard, E. Parizot, A.V. Olinto, On the transition from galactic to extragalactic cosmic-rays: spectral and composition features from two opposite scenarios, *Astropart. Phys.* 27 (1) (2007) 61–75. [astro-ph/0512345](#), doi:[10.1016/j.astropartphys.2006.09.006](#).
- [16] A. Aab (The Pierre Auger Collaboration), Depth of maximum of air-shower profiles at the Pierre Auger Observatory. II. composition implications, *Phys. Rev. D* 90 (12) (2014) 122006, doi:[10.1103/PhysRevD.90.122006](#).
- [17] J. Matthews, A. Heitler model of extensive air showers, *Astropart. Phys.* 22 (5–6) (2005) 387–397, doi:[10.1016/j.astropartphys.2004.09.003](#).
- [18] J. Alvarez-Muñiz, et al., Hybrid simulations of extensive air showers, *Phys. Rev. D* 66 (3) (2002) 033011. [astro-ph/0205302](#), doi:[10.1103/PhysRevD.66.033011](#).
- [19] A. Aab (The Pierre Auger Collaboration), *Nucl. Instrum. Meth. A* 798 (2015) 172–213, doi:[10.1016/j.nima.2015.06.058](#).
- [20] H. Kawai (The Telescope Array Collaboration), Telescope Array Experiment, *Nucl. Phys. B Proc. Suppl.* 175–176 (2008) 221–226, doi:[10.1016/j.nuclphysbps.2007.11.002](#).
- [21] D. Heck, et al., **CORSIKA: A Monte Carlo Code to Simulate Extensive Air Showers**, Technical Report, Forschungszentrum Karlsruhe GmbH, Karlsruhe, 1998.
- [22] J.A. Ortiz, G. Medina-Tanco, V. de Souza, Longitudinal development of extensive air showers: hybrid code SENECA and full Monte Carlo, *Astropart. Phys.* 23 (5) (2005) 463–476. [astro-ph/0411421](#), doi:[10.1016/j.astropartphys.2005.02.007](#).
- [23] T. Bergmann, et al., One-dimensional hybrid approach to extensive air shower simulation, *Astropart. Phys.* 26 (6) (2007) 420–432, doi:[10.1016/j.astropartphys.2006.08.005](#).
- [24] K. Werner, T. Pierog, Extended air shower simulations using EPOS, in: *AIP Conference Proceedings*, vol. 928, AIP, 2007, pp. 111–117, doi:[10.1063/1.2775903](#).
- [25] S. Ostapchenko, Monte Carlo treatment of hadronic interactions in enhanced Pomeron scheme: QGSJET-II model, *Phys. Rev. D* 83 (1) (2011) 014018. [1010.1869](#), doi:[10.1103/PhysRevD.83.014018](#).
- [26] J. Abraham (The Pierre Auger Collaboration), Trigger and aperture of the surface detector array of the Pierre Auger Observatory, *Nucl. Instrum. Meth. A* 613 (1) (2010) 29–39, doi:[10.1016/j.nima.2009.11.018](#).

- [27] J. Hersil, et al., Observations of extensive air showers near the maximum of their longitudinal development, Phys. Rev. Lett. 6 (1) (1961) 22–23, doi:[10.1103/PhysRevLett.6.22](https://doi.org/10.1103/PhysRevLett.6.22).
- [28] D.M. Edge, et al., The cosmic ray spectrum at energies above  $10^{17}$  eV, J. Phys. A 6 (1973) 1612, doi:[10.1088/0305-4470/6/10/019](https://doi.org/10.1088/0305-4470/6/10/019).
- [29] M. Nagano, et al., Energy spectrum of primary cosmic rays between  $10^{14.5}$  and  $10^{18}$  eV, J. Phys. G 10 (1984) 1295–1310, doi:[10.1088/0954-3899/18/2/022](https://doi.org/10.1088/0954-3899/18/2/022).
- [30] C. Di Giulio, Energy calibration of data recorded with the surface detectors of the Pierre Auger Observatory, in: Proceedings of the 31st ICRC, Lódz, Poland, 2009.
- [31] W.D. Apel (The KASCADE-Grande Collaboration), Cosmic ray energy reconstruction from the S(500) observable recorded in the KASCADE-grande air shower experiment, Astropart. Phys. 77 (2016) 21–31, doi:[10.1016/j.astropartphys.2015.12.002](https://doi.org/10.1016/j.astropartphys.2015.12.002).
- [32] J.C. Arteaga-Velazquez, The energy spectrum of primary cosmic rays reconstructed with the KASCADE-grande muon data, in: Proceedings of the 31st ICRC, Lódz, Poland, 2009.
- [33] H. Sagawa, Telescope array extension: TA x 4, in: Proceedings of the 34th ICRC, 2015.
- [34] R. Engel, Upgrade of the Pierre Auger Observatory (AugerPrime), in: Proceedings of the 34th ICRC, 2015.
- [35] G. Battistoni, et al., The FLUKA code: description and benchmarking, in: AIP Conference Proceedings, vol. 896, 2007, pp. 31–49.

## 6 A new air-shower observable to constrain hadronic interaction models



Contents lists available at ScienceDirect



## A new air-shower observable to constrain hadronic interaction models

Raul R. Prado\*, Vitor de Souza

*Instituto de Física de São Carlos, Universidade de São Paulo, São Carlos, Brazil*



### ARTICLE INFO

#### Article history:

Received 24 January 2017

Revised 26 April 2017

Accepted 19 May 2017

Available online 30 May 2017

#### Keywords:

Extensive air showers

Muons

Hadronic interaction models

### ABSTRACT

The energy spectrum of muons at ground level in air showers is studied and a new observable is proposed to constrain hadronic interaction models used in air shower simulations. An asymmetric Gaussian function is proposed to describe the muon ground energy spectrum and its parameters are studied regarding primary particle, energy and hadronic interaction models. Based on two realistic measurements of the muon density at a given distance from the shower axis, a new observable ( $r_\mu$ ) is defined. Considering realistic values of detector resolutions and number of measured events, it is also shown  $r_\mu$  can be successfully used to constrain low and high energy hadronic interaction models. The study is focused in the energy range between  $10^{17.5}$  and  $10^{18.0}$  eV because of the importance of this interval for particle physics and astrophysical models. The constraining power of the new observable is shown to be large within current experimental capabilities.

© 2017 Elsevier B.V. All rights reserved.

### 1. Introduction

The interaction of ultra high energy cosmic rays with atmospheric nuclei allows us to access hadronic interactions at energies much beyond the reach of man-made accelerators. However several properties of the cosmic ray phenomena and of the detection techniques impose limitations on the available information to study the highest energetic interactions. Experiments are only able to measure the air shower produced by the interaction of the cosmic particles with the nucleus of atoms in the atmosphere. The study of elementary properties of particle physics is done by relating global shower parameters to the properties of the hadronic interactions.

The depth at which the shower reaches its maximum number of particles ( $X_{\max}$ ) and the muon component are the most used shower features related to properties of particle interactions. At the same time, they are also strongly sensitive to the type of the shower primary particle [1]. Given that the primary particle type cannot be determined on event-by-event basis, different primary compositions must be considered in the study of the interaction properties. Usually, the large possibility of primary particles, from proton to iron nuclei, makes it impossible to disentangle the mass of the cosmic particle from particle interaction properties.

This paper proposes an analysis procedure to constrain hadronic interaction models by the measurements of the muon density by two different detectors. The idea proposed here is to compare the

predictions of the models to measurements based on the muon density at ground level. It will be shown in Section 4 that the muon ground energy spectrum has valuable information, which allow to discriminate among different hadronic interaction models.

Hadronic interaction models used in Monte Carlo simulations of air showers are limited to phenomenological approaches tested and tuned to collider data [2]. Three hadronic models for high energy interaction ( $>80$  GeV) and three hadronic models for low energy interaction ( $<80$  GeV) were investigated. A new and realistic air-shower observable based on two measurements of the muon density by different detectors is proposed in this paper and it is demonstrated to be powerful enough to constrain the hadronic interaction models.

The analysis procedure proposed here does not aim to infer properties of the particle interactions, instead, the new proposed parameter has power to test the predictions of the hadronic interaction models within realistic experimental conditions. By comparing the prediction of the models to future measurements of the new parameter, it will be possible to select the best model and guide the way towards a better understanding of the underlying assumptions taken by that model.

The work is based on Monte Carlo simulations of air showers. The new proposed parameter is studied in the energy range from  $10^{17.5}$  to  $10^{18.0}$  eV. The energy range is limited in order to minimize the effect of systematic uncertainties in energy reconstruction and also because of the importance of this range, which is the transition energy range from collider data to the extrapolation domain. It is shown that the new parameter can be used to test hadronic interaction models without knowledge on the primary composition.

\* Corresponding author.

E-mail address: [raul.prado@usp.br](mailto:raul.prado@usp.br) (R.R. Prado).

The paper is organized as follows: [Section 2](#) describes the simulations, [Section 3](#) shows a study on the energy spectra of muons at the ground level, [Section 4](#) proposes the new parameter and studies its behavior with relation to primary mass, energy and detector properties, [Section 5](#) quantifies the constraining power of the new parameter and [Section 6](#) concludes the work.

## 2. Simulations

Extensive air showers were simulated using the Monte Carlo code CORSIKA v7.500 [3]. The applied thinning factor was  $10^{-2}$  for the electromagnetic component and  $10^{-4}$  for the hadronic component, with the maximum weight for any particle set to 100. It was verified that the choice of this thinning configuration does not result in a bias in the present analysis. The energy of the primary particles was sampled continuously between  $10^{17.5}$  and  $10^{18.0}$  eV, following a power law energy spectrum with index  $-3$ . The arrival directions were sampled following a uniform distribution in solid angle, up to a maximum zenith angle of  $60^\circ$ . Three primaries were simulated: proton, nitrogen nucleus and iron nucleus. The minimum energy of particles simulated in air showers were set to 0.3 GeV for hadrons and muons, and 0.003 GeV for electrons and photons. Three hadronic interaction models were used for high energies interactions ( $>80$  GeV): QGSJetII-04 [4], EPOS-LHC [5,6] and Sibyll2.3 [7], and three for low energies ( $<80$  GeV): FLUKA [8], GHEISHA [9] and UrQMD [10]. For each selected combination of hadronic interaction model and primaries particle, 1200 showers were generated. The ground altitude (1400 m above sea level) was chosen to be the one at the Pierre Auger Observatory.

The energy spectrum of muons at ground level is the shower feature to be considered in this paper. The energy spectra were built by collecting from the simulated air showers all muons reaching ground in a lateral distance between 425 and 475 m from the shower axis. Although a full detector reconstruction is not applied, in [Section 4.1](#) the detector effects are taken into account by artificial smearing the shower observables around its simulated values. Detector thresholds and geometry are considered as well.

To sample showers at the same stage of development, the commonly used  $DX$  parameter is used.  $DX$  is the slant atmospheric depth between the shower maximum and the ground. It is given by

$$DX = \frac{X_{\text{gr.vert}}}{\cos \theta} - X_{\text{max}}, \quad (1)$$

where  $X_{\text{gr.vert}}$  is the vertical slant depth of the ground,<sup>1</sup>  $\theta$  is the zenith angle of the shower axis and  $X_{\text{max}}$  is the depth in which the shower reaches its maximum. For each simulated event, the  $\theta$  corresponds to the true zenith angle as set in the input of the simulation and  $X_{\text{max}}$  was taken directly from the Gaisser–Hillas function fitted to the longitudinal energy deposit profile.

## 3. Characterization of the muon ground energy spectrum

In this section, the simulations described in [Section 2](#) are used to characterize the energy spectrum of muons at ground level and to study its relations with primary mass and hadronic interaction models.

[Fig. 1](#) shows examples of the ground energy spectrum of muons for six simulated events, which differ by the primary particle and the shower geometry. The low and high energy hadronic interaction models are FLUKA and QGSJetII-04, respectively. Examples have been selected to illustrate the general shape of the muon spectrum for different primary particles and extreme values of  $DX$ . The left-hand column shows deep showers, with relatively small

$DX$  values, while the right-hand column shows shallow showers, with relatively high values of  $DX$ . The normalization and the mean of the distributions are clearly different but the overall shape is very similar.

As shown by the red lines in [Fig. 1](#), the ground energy spectrum of muons is well described by the following asymmetric Gaussian function

$$\frac{dN_\mu}{dx} = \begin{cases} N_0 \exp \left[ -\frac{1}{2} \left( \frac{x-\eta}{\sigma} \right)^2 \right], & \text{if } x < \eta \\ N_0 \exp \left[ -\frac{1}{2} \left( \frac{x-\eta}{\alpha\sigma} \right)^2 \right], & \text{if } x > \eta \end{cases} \quad (2)$$

where  $x = \log_{10}(E/\text{GeV})$ .  $N_0$  is the normalization parameter and it is correlated with the total number of muons in the shower.  $\eta$  is the mode of the energy distribution, and it is strongly correlated with the average energy of muons reaching ground between 425 and 475 m distance from the shower axis.  $\sigma$  and  $\alpha$  give the width of the distribution,  $\alpha$  being the parameter that measures the degree of asymmetry of the distribution.

Muon energy spectra of all simulated showers were fit by the function presented in [Eq. \(2\)](#), in which  $N_0$ ,  $\eta$ ,  $\sigma$  and  $\alpha$  were taken as free parameters. The fitting was performed using a binned maximum likelihood method with Poissonian probability distribution functions.

Since the ground energy spectrum of muons is well described by the asymmetric Gaussian function, one may study its dependencies on the energy, primary particle and hadronic interaction models through the evolution of the parameters  $N_0$ ,  $\eta$ ,  $\sigma$  and  $\alpha$  with  $DX$ . [Fig. 2](#) shows the  $DX$  evolution of the four parameters for three different energy intervals, [Fig. 3](#) for three primary particles and [Fig. 4](#) for five combinations of high and low energy hadronic interaction models.

It is clear from [Fig. 2](#) that the normalization ( $N_0$ ) is the only property of ground muon energy spectrum which shows a significant dependence on the primary energy. As expected,  $N_0$  also depends strongly on the primary particle and hadronic interaction model (see [Figs. 3](#) and [4](#)), which reflects the very known behavior of number of muons in air showers. Concerning the peak position of the distributions,  $\eta$ , a strong evolution with  $DX$  is observed, revealing the shift of the average energy of muons to higher values with increasing  $DX$ . Besides normalization and peak positions, changes on the overall shape of the energy spectrum of muons can be evaluated through the parameters  $\sigma$  and  $\alpha$ . These parameters clearly show a very weak evolution with  $DX$ , and a nearly null dependence on the primary energy and primary particle and a relatively very small dependence on the hadronic interaction models.

The analysis of [Fig. 4](#) also repeats known though less popular lessons: the effect of low energy hadronic interaction models are as important as the high energy one regarding the description of the muonic component in air-shower simulations [11]. The differences of  $N_0$  between QGSJetII-04/FLUKA and QGSJetII-04/UrQMD or GHEISHA are of the same order or larger than the largest difference between the high energy interaction models. The average energy of muons, correlated with  $\eta$ , is larger for GHEISHA, followed by UrQMD and then FLUKA. The differences in  $\eta$  due to the low energy hadronic interaction models are as large as the differences due to the high energy hadronic interaction models. Regarding  $\sigma$  and  $\alpha$  parameters, one can see in [Fig. 4](#) they show the same weak  $DX$  evolution for all the hadronic model combinations. Furthermore, the effect of low energy hadronic models is again clear as shown by the difference between FLUKA and GHEISHA, or UrQMD.

Finally, the analysis of [Fig. 4](#) also opens new possibilities. It turns out that  $\eta$  is strongly sensitive to the hadronic interaction models, and at the same time, it does not show any significant dependence on the primary energy and on the primary particle. The lack of primary energy dependence is important experimen-

<sup>1</sup>  $X_{\text{gr.vert}} = 870 \text{ g/cm}^2$  for the Pierre Auger Observatory.

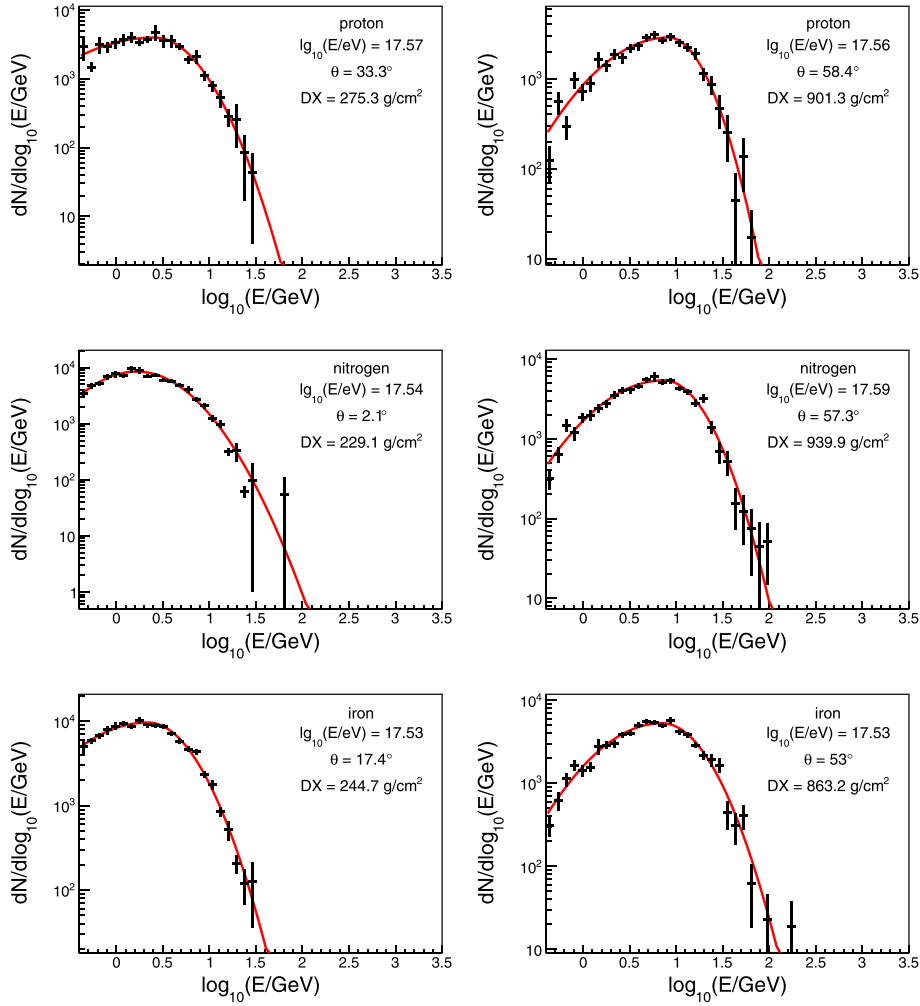


**Fig. 1.** Example of the ground muon energy spectrum for six simulated showers. Shower parameters are shown in each panel. The energy spectra were built by collecting from the air-shower simulation all muons hitting the ground in a lateral distance between 425 and 475 m from the shower axis. The low and high energy hadronic interaction models are FLUKA and QGSjetII-04, respectively. Red lines are the result of fitting Eq. (2) to the data points. (For interpretation of the references to color in this figure legend, the reader is referred to the web version of this article.)

tally to eliminate effects from the experimental energy scale, while the lack of primary particle dependence is an essential property to disentangle the hadronic interaction effects from the primary composition determination. The evolution of  $\eta$  with  $DX$  is simple (linear) and strong, which makes easy to study showers in different evolution stages.

All of these are indications that accessing experimentally the information carried by  $\eta$  could be successfully used to constrain the hadronic interaction models. In the next section a new observable which is strongly correlated to  $\eta$  is studied and its constraining power in realistic experimental conditions is tested.

#### 4. An observable to test hadronic interaction models

Accessing  $\eta$  directly is not possible for any running or planned UHECR experiment. Therefore, instead of proposing an unrealistic parameter, this study starts from a realistic experimental scenario and aims to find an observable which correlates to  $\eta$ . A generic experimental set-up is considered with two muon detector arrays with different amount of shielding leading to two energy thresholds. With such an experimental set-up, it is possible to measure the integral of the energy spectrum or the energy density of muons above two energy thresholds.

Using the simulations described in Section 2 the density of muons in the lateral distance from 425 to 475 m from the shower axis was calculated for a surface ( $S_\mu^{\text{sur}}$ ) and a buried ( $S_\mu^{\text{bur}}$ ) detectors and a new parameter is defined:

$$r_\mu = \sec^\beta \theta \frac{S_\mu^{\text{bur}}}{S_\mu^{\text{sur}}}, \quad (3)$$

where  $\theta$  is the zenith angle of the primary particle. The term  $\sec^\beta \theta$  compensates the zenith dependence on the energy threshold and the effective area of the buried detectors. The surface detector ( $S_\mu^{\text{sur}}$ ) is considered to have  $10 \text{ m}^2$  and the buried detector ( $S_\mu^{\text{bur}}$ ) to have  $30/\cos\theta \text{ m}^2$ , which are motivated by water-Cherenkov stations and flat buried scintillators respectively.  $\beta$  was determined to minimize the primary mass dependence of  $r_\mu$ . In Fig. 5 the  $r_\mu$  dependence on  $\beta$  is shown for one hadronic interaction models, which justify the choice of  $\beta = 0.6$  as the value that minimizes the difference between primaries. The detector features considered is described in the next section.

Figs. 6 and 7 show the distributions of  $r_\mu$  for several energy thresholds of the buried detector. Three cases are shown in which the vertical muon energy threshold of the buried detector ( $E_{\text{vert},\mu}^{\text{th}}$ ) is changed. The effective energy threshold for a muon with incident zenith angle  $\theta_\mu$  is  $E_{\text{vert},\mu}^{\text{th}}/\cos\theta_\mu$ . For the surface detectors, the energy threshold is kept fixed at 0.3 GeV. Fig. 6 compares the

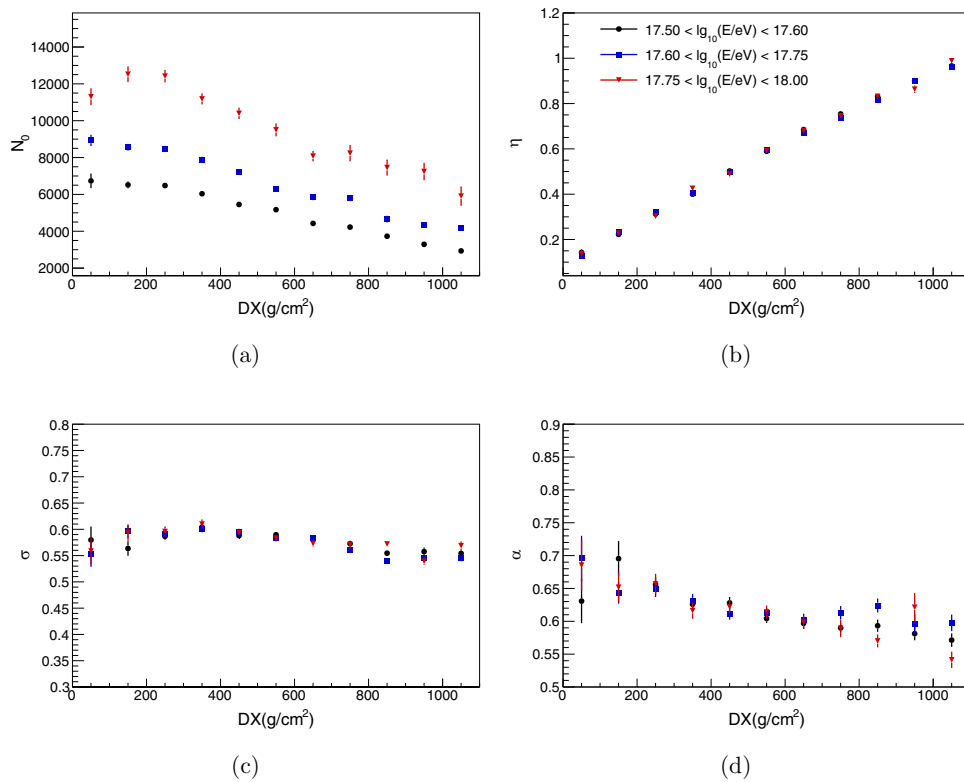


**Fig. 2.** (a)  $N_0$ , (b)  $\eta$ , (c)  $\sigma$  and (d)  $\alpha$  as a function of  $DX$  for three energy intervals. Same number of p, N and Fe showers are considered. The hadronic interaction models used are FLUKA and QGSjetII-04.

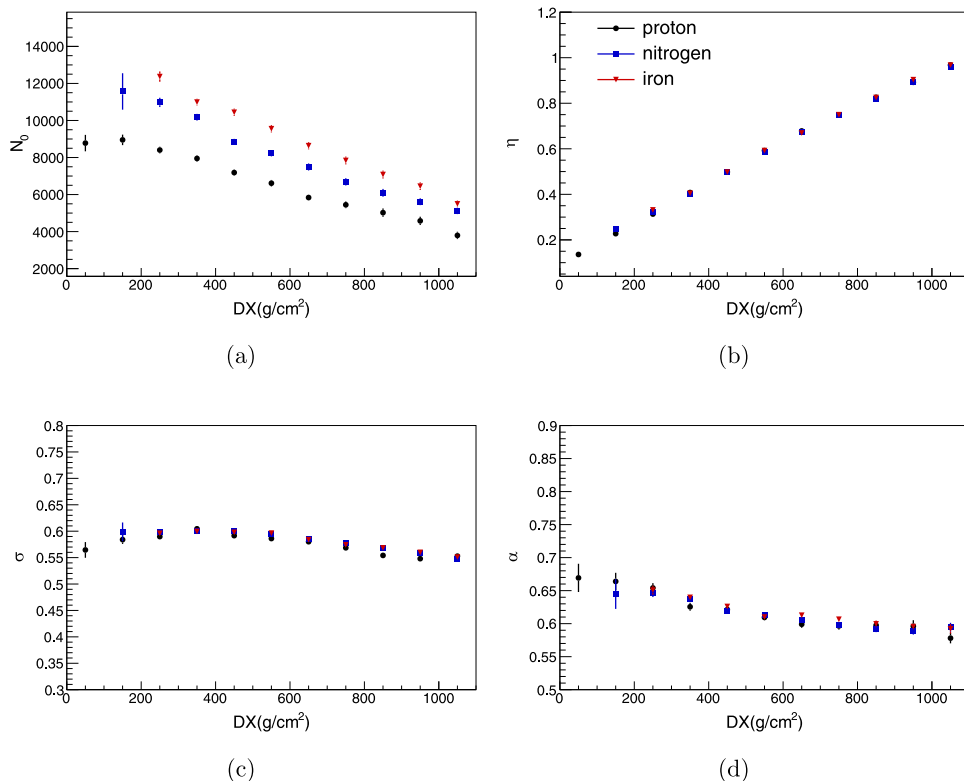


**Fig. 3.** (a)  $N_0$ , (b)  $\eta$ , (c)  $\sigma$  and (d)  $\alpha$  as a function of  $DX$  for three primary particles. The energy interval for all primaries is  $17.5 < \log_{10}(E/eV) < 18.0$ . The hadronic interaction models used are FLUKA and QGSjetII-04.

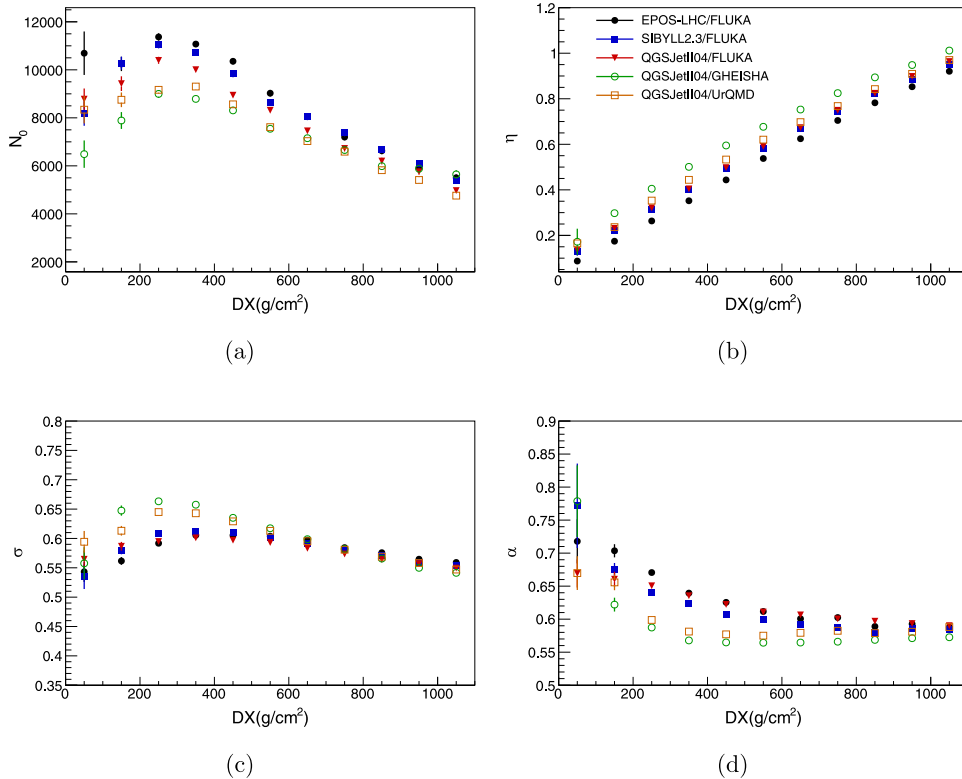


**Fig. 4.** (a)  $N_0$ , (b)  $\eta$ , (c)  $\sigma$  and (d)  $\alpha$  as a function of  $DX$  for five combinations of hadronic interaction models. The energy interval for all primaries is  $17.5 < \log_{10}(E/eV) < 18.0$ . Same number of p, N and Fe showers are considered.

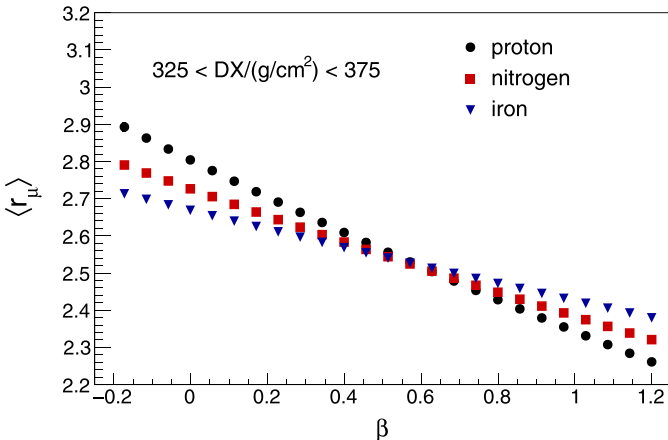


**Fig. 5.**  $\langle r_\mu \rangle$  as a function of  $\beta$  for one small  $DX$  interval and for three different primaries.  $\beta = 0.6$  was chosen to minimize the dependence of  $r_\mu$  with primary particle.

distributions for different high energy hadronic interaction models and Fig. 7 for different low energy hadronic interaction models. The different degrees of separation of the hadronic interaction models with different energy threshold is clear, pointing to the possibility to constrain the hadronic interaction models using  $r_\mu$ . In the next sections, the constraining power of  $r_\mu$  is estimated and its correlation with  $\eta$  is shown.

#### 4.1. $r_\mu$ Determination including detector characteristics

In this section, the effect of detector geometry, muon energy thresholds, detector resolutions and systematic uncertainties on  $r_\mu$  are studied. To include the detector features in the proposed analysis, the general characteristics of the muon detectors of the Pierre Auger Observatory are considered. A surface detector with  $10 m^2$  of effective area is considered to measure muons with energies above 0.3 GeV. Its general characteristics are inspired in the AugerPrime [12–14] design of water-Cherenkov stations with plastic scintillators on top. A second detector is considered based on

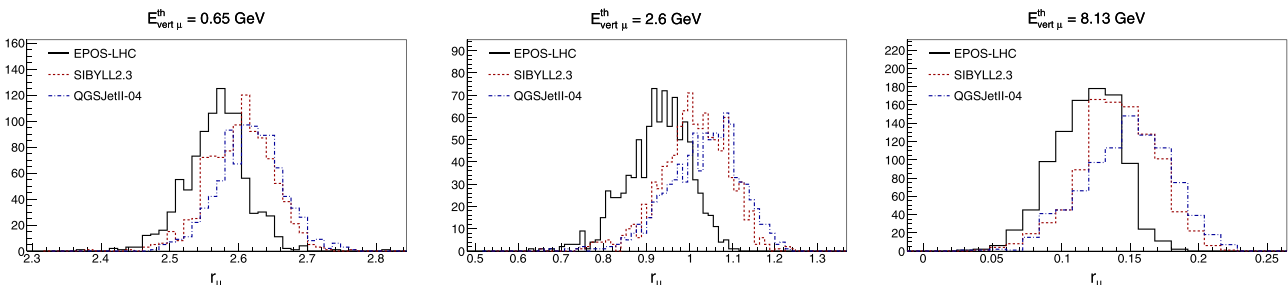


**Fig. 6.**  $r_\mu$  distributions of the three high energy hadronic interaction models. Each panel shows the distributions for a given energy thresholds of the buried detector,  $E_{\text{vert},\mu}^{\text{th}} = 0.65, 2.6, 8.13$  GeV from left to right. Low energy hadronic interaction model is FLUKA.

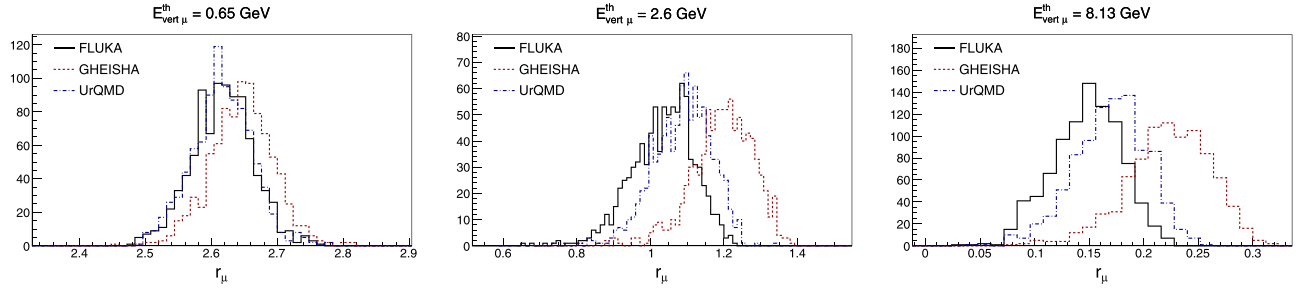


**Fig. 7.**  $r_\mu$  distributions of the three low energy hadronic interaction models. Each panel shows the distributions for a given energy thresholds of the buried detector,  $E_{\text{vert},\mu}^{\text{th}} = 0.65, 2.6, 8.13 \text{ GeV}$  from left to right. High energy hadronic interaction model is QGSjetII-04.

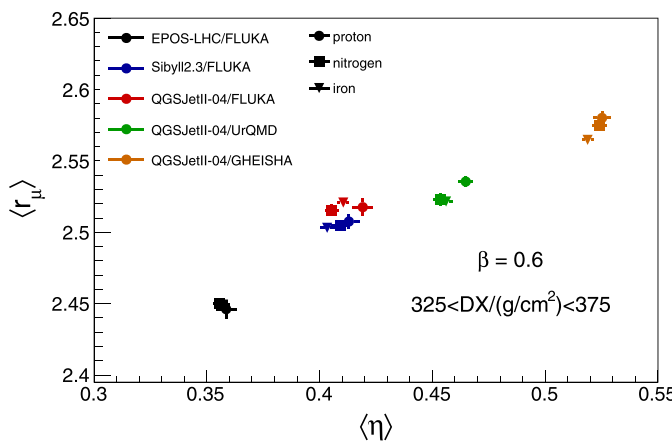


**Fig. 8.** Mean  $r_\mu$  as a function of  $\langle \eta \rangle$  for  $325 < DX/\text{g/cm}^2 < 375$ .  $\beta$  was set to 0.6. See Eqs. (2) and (3) for definitions of the parameters. Detectors effective area and threshold were considered according to Section 4.1. Five combinations of hadronic interaction models is shown for three primary particles. A nearly linear correlation is seen and a clear separation of many hadronic interaction models is visible.

the general characteristics of the Auger AMIGA detector [15,16]. Those are  $30 \text{ m}^2$  flat scintillator detectors buried 2.5 m below the ground. The muon energy threshold for the buried detectors depends on the incident zenith angle of the particle and it is given by  $E_{\text{th}} = \beta \rho h / \cos \theta_\mu$ , where  $\beta = 1.808 \text{ MeV cm}^2 \text{ g}^{-1}$  is the fractional energy loss per depth of standard rock,  $\rho = 1.8 \text{ g cm}^{-3}$  is the soil density,  $h = 2.5 \text{ m}$  is the vertical depth of the detectors and  $\theta_\mu$  is the zenith incidence angle of the muon. Because of its flatness, the effective collection area of the detector decrease by a factor  $\cos \theta$ , where  $\theta$  is the zenith angle of the shower. The reconstruction of the muon density by an AMIGA-like detector has been shown to be satisfactorily possible for events with  $\theta < 45^\circ$  [17–19].

From now on, the results were obtained by considering the detector features shown above to calculate the muon density from the simulated air showers explained in Section 2. In this way, the most important properties of the detectors are considered without the need to perform a full detector simulation.

Fig. 8 shows the relation between the average value of  $r_\mu$  ( $\langle r_\mu \rangle$ ) and the average value of  $\eta$  ( $\langle \eta \rangle$ ) for showers with  $325 < DX/\text{g/cm}^2 < 375$  according to the detector properties explained above. Five combinations of low and high energy hadronic interaction models are shown in different colors and three primaries are shown in different marker styles. From Fig. 8, one can see a nearly linear relation between  $\langle r_\mu \rangle$  and  $\langle \eta \rangle$ . Furthermore, the relatively large separation between the hadronic interaction model combinations by  $\langle r_\mu \rangle$  is clear, which shows  $r_\mu$  is a good observable to constrain hadronic interaction properties.

The resolutions on the muon density reconstruction were taken into account by applying a Gaussian smearing on the true signal

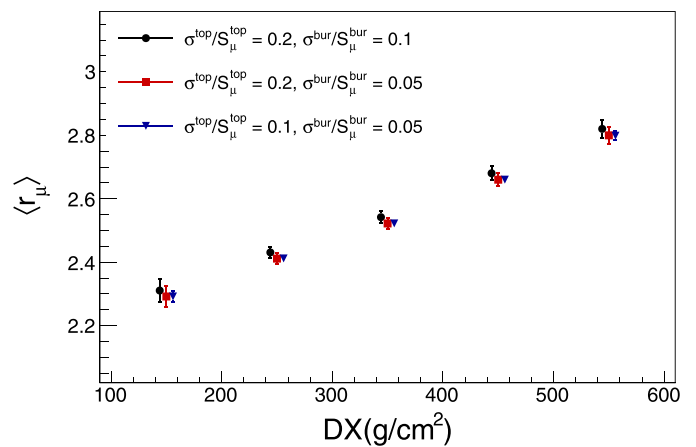


**Fig. 9.**  $\langle r_\mu \rangle$  as a function of  $DX$  for different values of  $S_\mu^{\text{sur}}$  and  $S_\mu^{\text{bur}}$  resolution. The mean value  $\langle r_\mu \rangle$  is calculated over 2000 realizations in which the detector resolution was applied to each simulated shower. Points were artificially shifted in  $DX$  for clarity.

obtained from the simulations.  $S_\mu^{\text{sur}}$  resolution was considered to vary in the range from 10% to 20% [12,14] and  $S_\mu^{\text{bur}}$  resolution in the range from 5% to 10% [18,19]. Fig. 9 shows the effect of the resolution in the calculation of  $\langle r_\mu \rangle$ . The Gaussian smearing were performed 2000 times and the  $\langle r_\mu \rangle$  is shown as a function of  $DX$ . The standard deviation of  $r_\mu$  distributions is shown by the error bars. Three cases are shown in which the resolution on both  $S_\mu^{\text{sur}}$  and  $S_\mu^{\text{bur}}$  vary. The systematic effect of the detector resolution in the determination of  $\langle r_\mu \rangle$  is smaller than 5%.

Besides the experimental resolutions, systematic uncertainties on  $S_\mu^{\text{sur}}$  and  $S_\mu^{\text{bur}}$  can be originated from the detection and reconstruction procedures. Typically the most significant systematic uncertainty on muon density measurements are due to systematic uncertainties on the shower energy determination, which affects both  $S_\mu^{\text{sur}}$  and  $S_\mu^{\text{bur}}$  in the same magnitude. To evaluate the effect of systematic uncertainties on  $r_\mu$ , the simulated  $S_\mu^{\text{sur}}$  and  $S_\mu^{\text{bur}}$  were shifted artificially and the resulting  $r_\mu$  were calculated. First it was considered the shifts on  $S_\mu^{\text{sur}}$  and  $S_\mu^{\text{bur}}$  are totally correlated, which means the same magnitude and direction. This case represents the energy reconstruction uncertainty effect. Fig. 10 shows the  $r_\mu$  as a function of  $DX$ , for one hadronic interaction models combination, for different cases in which  $S_\mu^{\text{sur}}$  and  $S_\mu^{\text{bur}}$  were shifted by a factor  $1 + \delta^{\text{top}}$  and  $1 + \delta^{\text{bur}}$  respectively. In Fig. 10 left panel it is shown the effect of a 10% shift on both muon density at the same direction. Clearly, correlated systematic uncertainties on  $S_\mu^{\text{sur}}$  and  $S_\mu^{\text{bur}}$  have an insignificant effect on  $r_\mu$ . In Fig. 10 right panel it is shown the effect of systematic shifts of 2.5% on  $S_\mu^{\text{sur}}$  and  $S_\mu^{\text{bur}}$  in opposite directions. The magnitude of the  $\langle r_\mu \rangle$  deviation is of order 0.05.

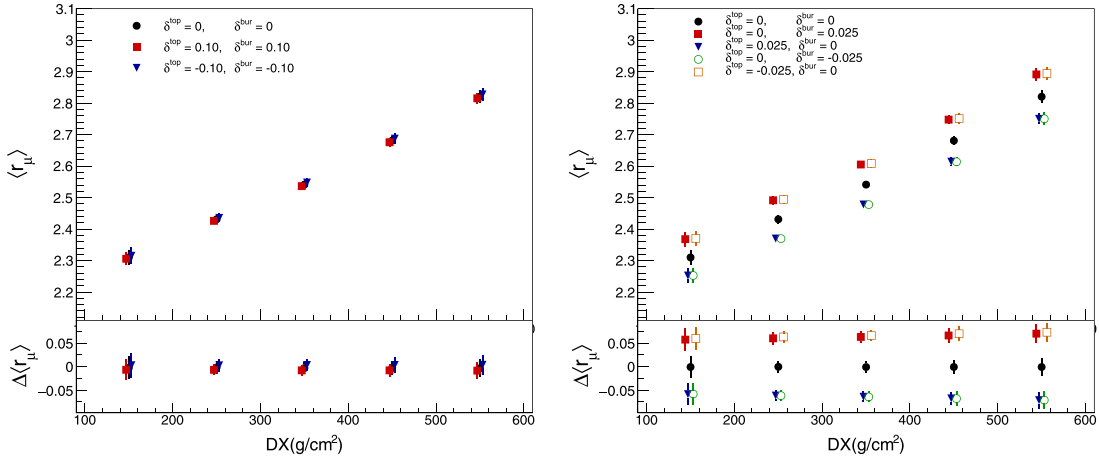


**Fig. 10.**  $\langle r_\mu \rangle$  as a function of  $DX$  for different combinations of the systematic uncertainties on  $S_\mu^{\text{sur}}$  and  $S_\mu^{\text{bur}}$ .  $\delta^{top}$  and  $\delta^{bur}$  are defined in Section 4.1. All simulated primary particles are included (p, N, Fe). Bottom panel shows the difference with relation to the average value. The hadronic interaction model combination used is QGSJetII-04/FLUKA. Points were artificially shifted in  $DX$  for clarity.

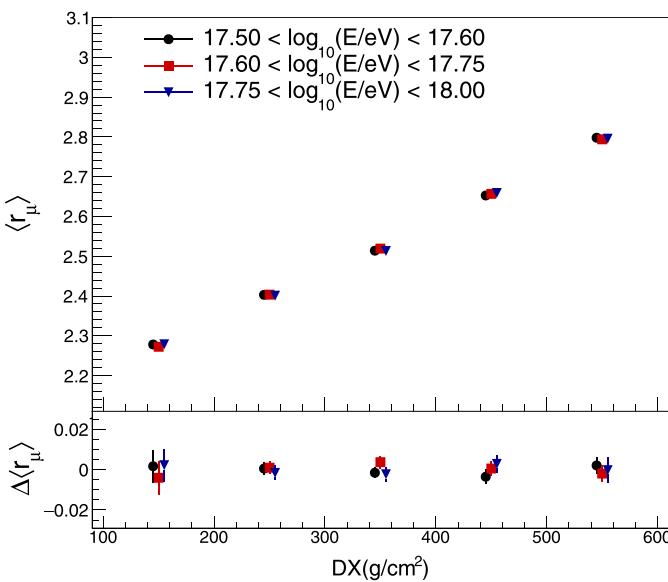


**Fig. 11.**  $\langle r_\mu \rangle$  as a function of  $DX$  for three energy intervals. All simulated primary particles are included (p, N, Fe). Bottom panel shows the difference with relation to the average value. The hadronic interaction model combination used is QGSJetII-04/FLUKA. Points were artificially shifted in  $DX$  for clarity.

The consequences of this deviation on the separation between different hadronic interaction models is discussed in Section 5.

#### 4.2. $r_\mu$ Dependence on primary mass and energy

For the following analysis, the  $DX$  range was defined to preserve a good statistics in all  $DX$  bins and it goes from 100 to 600 g/cm $^2$  divided in 5 bins of 100 g/cm $^2$ . The upper bound of 600 g/cm $^2$  is highly influenced by the shower zenith angle limitation at  $\theta < 45^\circ$  due to the buried detector features.

Fig. 11 shows the evolution of  $\langle r_\mu \rangle$  as a function of  $DX$  for different energy ranges. All simulated primary particles are included (p, N and Fe). Hadronic interaction model combination here is QGSJetII-04/FLUKA. A better visualization of the differences in  $\langle r_\mu \rangle$  is seen in the bottom panel of Fig. 11, where  $\Delta r_\mu$  are the differences with relation to the average value of  $\langle r_\mu \rangle$  for the three energy ranges considered. The differences of  $\langle r_\mu \rangle$  in all energy intervals is smaller than 1% for the entire  $DX$  range. The energy independence of  $\langle r_\mu \rangle$

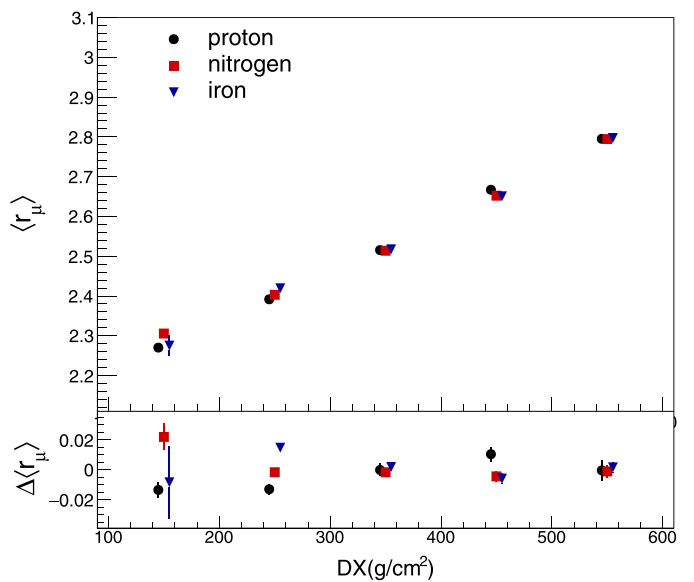


**Fig. 12.**  $\langle r_\mu \rangle$  as a function of  $DX$  for three primary particles (pr, N, Fe). All simulated energies are included. Bottom panel shows the difference with relation to the average value. The hadronic interaction model combination used is QGSJetII-04/FLUKA. Points were artificially shifted in  $DX$  for clarity.

is expected, since  $S_\mu^{\text{sur}}$  and  $S_\mu^{\text{bur}}$  evolve similarly with energy in the range from  $10^{17.5}$  to  $10^{18.0}$  eV. The lack of energy dependence is an advantage because it allows the analysis of events in a large energy interval, increasing significantly the available statistics. Furthermore, it also contributes to diminishing any effect due to the experimental energy scale.

The primary mass dependence of the  $\langle r_\mu \rangle$  is shown in Fig. 12. The hadronic interaction model combination shown is again QGSJetII-04/FLUKA. Very similar results were obtained for all combinations of models. The bottom panel shows the  $\Delta\langle r_\mu \rangle$ . The observed primary mass dependence is below 2%. The dependence of  $\langle r_\mu \rangle$  with the primary particle was minimized by choosing  $\beta = 0.6$ . The lack of  $\langle r_\mu \rangle$  dependence on the primary particle is a great advantage because it disentangles the study of the hadronic interaction properties from the determination of the primary particle type.

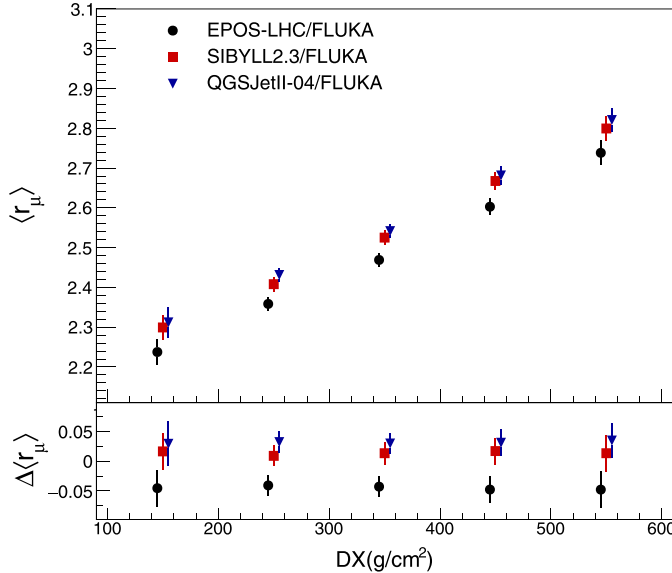


**Fig. 13.**  $\langle r_\mu \rangle$  as a function of  $DX$  for three high energy hadronic interaction models. All simulated energies are included. All simulated primary particles are included (p, N, Fe). Bottom panel shows the difference with relation to the average value. Low energy hadronic interaction model is FLUKA. The detector resolution is set to 20% for  $S_\mu^{\text{sur}}$  and 10% for  $S_\mu^{\text{bur}}$ . Points were artificially shifted in  $DX$  for clarity.

## 5. Results: constraining hadronic interaction models with $r_\mu$ parameter

In this section, the capacity to constrain hadronic interaction models by measuring  $r_\mu$  is demonstrated by studying the  $DX$  evolution of  $\langle r_\mu \rangle$  for different combinations of low and high energy hadronic models. Detector resolution is taken into account as explained above. The effect of a limited number of events is considered here. The total number of simulated air showers used (3500) is approximately the number of hybrid events to be measured by the Pierre Auger Observatory infill array in 2 years of operation. The infill array consists of 750 m spaced water-Cherenkov stations spread over an area of 23.5 km<sup>2</sup>. In this same area the AMIGA-Grande and AugerPrime muon detectors are going to be installed. Considering the duty cycle of the fluorescence detectors to be 14%, the total exposure of this experimental set-up is 4.32 km<sup>2</sup>.sr.yr. Taking into account the cosmic-rays flux between  $10^{17.5}$  and  $10^{18.0}$  eV, the expected number of events to be measured per year is 1806.

Figs. 13 and 14 show the  $\langle r_\mu \rangle$  as a function of  $DX$  for different combinations of hadronic interaction models. In Fig. 13 the three high energy hadronic models are shown in combination with one low energy hadronic interaction model: FLUKA. In Fig. 14 the three low energy hadronic models are shown in combination with one high energy hadronic interaction model: QGSJetII-04. The bottom panels show the  $\Delta\langle r_\mu \rangle$ . The worst case for the detector resolution was considered: 10% for  $S_\mu^{\text{bur}}$  and 20% for  $S_\mu^{\text{sur}}$ . Figs. 13 and 14 show that even with a relatively poor detector resolution a clear separation between hadronic interaction models is achieved. In Fig. 13 it is observed that EPOS-LHC can be distinguished from QGSJetII-04 and Sibyll2.3, while in Fig. 14 it is seen that GHEISHA can be distinguished from UrQMD and FLUKA.

To better quantify the discriminating power of  $\langle r_\mu \rangle$ , the commonly used Merit Factor can be used. It is defined as:

$$\text{Merit Factor} = \frac{|\langle r_\mu \rangle_a - \langle r_\mu \rangle_b|}{\sqrt{\sigma_a^2 + \sigma_b^2}}, \quad (4)$$

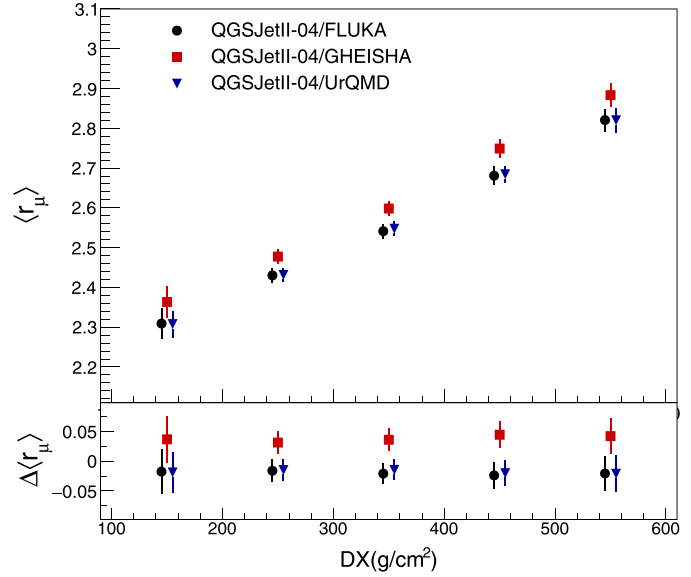


**Fig. 14.**  $\langle r_\mu \rangle$  as a function of  $DX$  for three low energy hadronic interaction models. All simulated energies are included. All simulated primary particles are included (p, N, Fe). Bottom panel shows the difference with relation to the average value. High energy hadronic interaction model is QGSJetII-04. The detector resolution is set to 20% for  $S_\mu^{\text{sur}}$  and 10% for  $S_\mu^{\text{bur}}$ . Points were artificially shifted in  $DX$  for clarity.

where  $a$  and  $b$  refer to any two hadronic interaction model combination and the  $\sigma$ 's are the standard deviations of  $\langle r_\mu \rangle$ .

Fig. 15 shows the Merit Factor as a function of  $DX$  for the same experimental resolutions and statistics described above. The left-hand panel refers to hadronic model combinations with different high energy models, and on the right-hand panel with different low energy models. The best Merit Factor is 3.0 between EPOS-LHC and QGSJetII-04 and 2.3 between FLUKA and GHEISHA.

Figs. 16 and 17 show the Merit Factor as a function of the number of events and detector resolution for one particular  $DX$  bin:  $300 < DX/(g/cm^2) < 400$ . The resolutions on  $S_\mu^{\text{sur}}$  and  $S_\mu^{\text{bur}}$  were re-scaled by a common factor  $f$ , being that  $\sigma_{\text{bur}} = 0.1fS_\mu^{\text{bur}}$  and  $\sigma_{\text{top}} = 0.2fS_\mu^{\text{top}}$ . The effect of the number of events was calculated by re-scaling the standard deviation of the muon densities by a factor  $\sqrt{N_{\text{sim}}/N}$ , where  $N_{\text{sim}}$  is the number of simulated showers and  $N$  is the number of showers in each case.

Fig. 16 shows that it is possible to reach large Merit Factor values (>5) for the separation between EPOS-LHC and QGSJetII-04/Sibyll2.3 using a reasonably small number of events (<6000) considering realistic detector resolutions ( $\sigma_{\text{bur}}/S_\mu^{\text{bur}} < 0.06$  and  $\sigma_{\text{top}}/S_\mu^{\text{top}} < 0.13$ ). On the other hand, the separation between Sibyll2.3 and QGSJetII-04 is small for any resolutions and number of events, which is expected because of their similar values of  $\eta$ . The same conclusions can be drawn about the low energy hadronic interactions models from Fig. 17.  $\langle r_\mu \rangle$  provides a very good separation between FLUKA and GHEISHA/UrQMD, but the separation power is limited for GHEISHA and UrQMD.

## 6. Conclusions

This paper studies the ground muon energy spectrum of air showers and proposes an analysis procedure to constrain hadronic interaction models used in Monte Carlo simulations. In Section 3, it was shown that the energy distribution of muons at ground level can be well described by an asymmetric Gaussian function with four parameters. The study of the evolution of the four parameters with  $DX$  concluded that the overall shape of the energy spectrum of muons does not depend strongly on the combination of low and

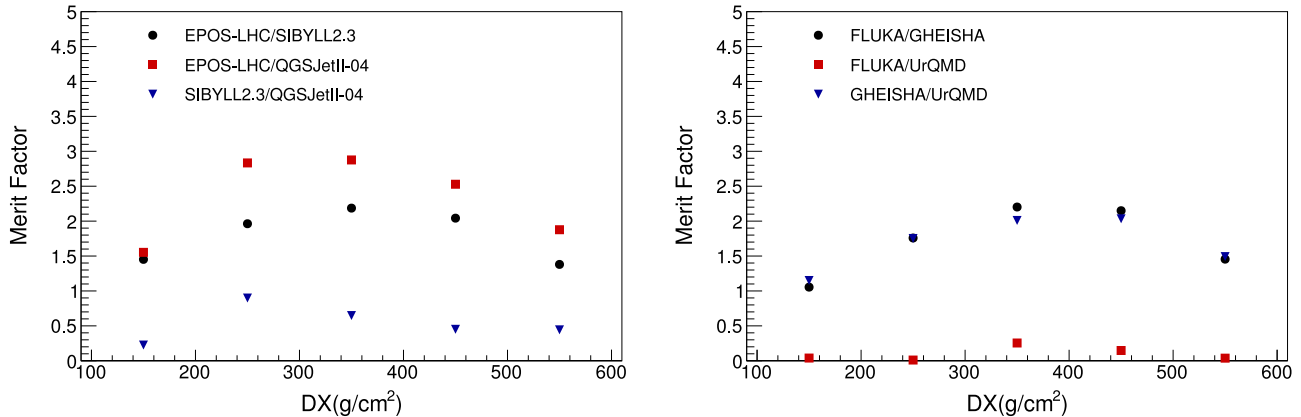


**Fig. 15.** Merit Factor calculated for two different hadronic interaction model combination as a function of  $DX$ . Left panel shows the cases in which the high energy hadronic interaction models are different and the low energy one is the same, FLUKA. The legend indicates the two hadronic models considered to calculate the Merit Factor. Right panel shows the cases in which the low energy hadronic interaction models are different and the high energy one is the same, QGSJetII-04.

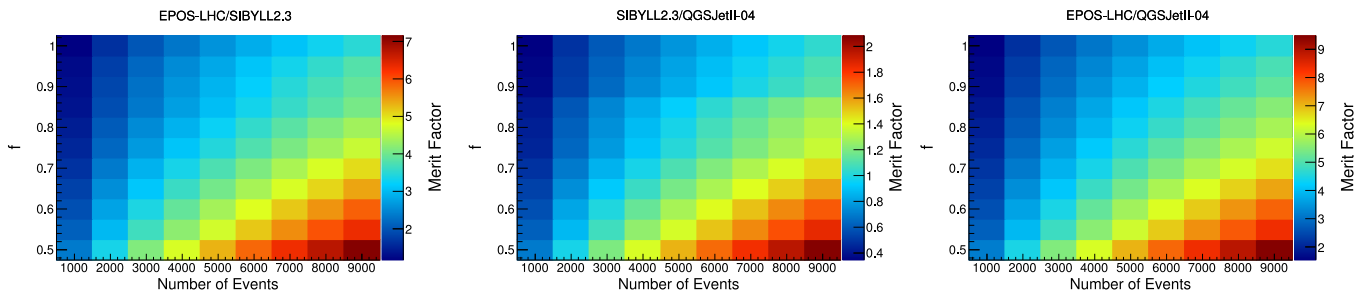


**Fig. 16.** Merit Factor as a function of the number of events and detector resolution. Detector resolution are defined as  $\sigma_{bur} = 0.1fS_\mu^{bur}$  and  $\sigma_{top} = 0.2fS_\mu^{top}$ . The Merit Factor is given in the color scale. (For interpretation of the references to color in this figure legend, the reader is referred to the web version of this article.)

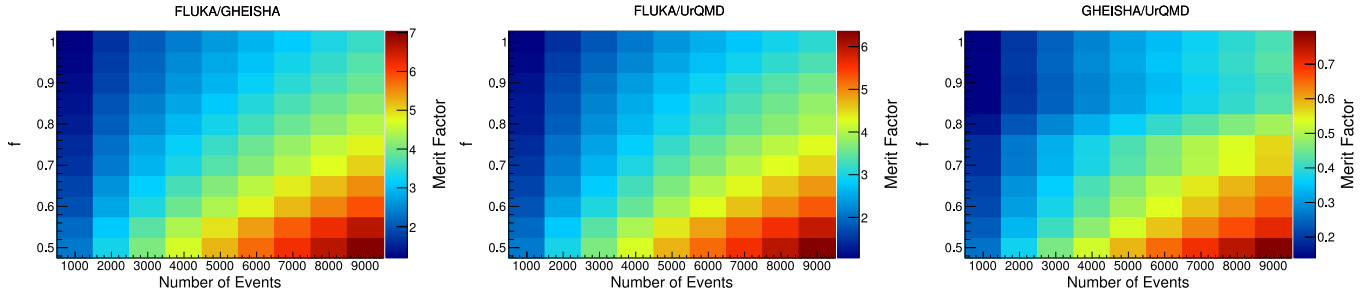


**Fig. 17.** Merit Factor as a function of the number of events and detector resolution. Detector resolution are defined as  $\sigma_{bur} = 0.1fS_\mu^{bur}$  and  $\sigma_{top} = 0.2fS_\mu^{top}$ . The Merit Factor is given in the color scale. (For interpretation of the references to color in this figure legend, the reader is referred to the web version of this article.)

high energy hadronic interactions models. Also, it was verified that the average muon energy, or the parameter  $\eta$ , is sensitive to the model combination and presents a strong evolution with  $DX$ .

However,  $\eta$  is not an easy parameter to be measured. Therefore in Section 4 a new and experimentally motivated parameter ( $r_\mu$ ) is proposed and its correlation with  $\eta$  is shown.  $r_\mu$  dependencies on the primary mass and energy were proven to be insignificant which allows on to disentangle the composition and the hadronic interaction studies as well as minimize the effect of systematic uncertainties in the energy reconstruction.

The general properties of the current and proposed muon detectors of the Pierre Auger Observatory are considered to study  $r_\mu$  under realistic experimental limitations. Section 5 shows that the discrimination power of  $r_\mu$  is significantly large. EPOS-LHC can be separated from Sibyll2.3 and QGSJetII-04 with large Merit Factor ( $>5$ ) using a reasonably small number of events ( $<6000$ ). Sibyll2.3 and QGSJetII-04 show similar average muon energy at ground and therefore can, in the best case, be discriminated with Merit Factor  $\sim 2$  with about 9000 events. As for the low energy hadronic

models, FLUKA can be separated from GHEISHA and UrQMD with large Merit Factor ( $>5$ ) using a reasonably small number of events ( $<6000$ ). GHEISHA and UrQMD can, in the best case, be discriminated with Merit Factor  $\sim 0.8$  with about 9000 events. It was shown that correlated systematic uncertainties on  $S_\mu^{sur}$  and  $S_\mu^{bur}$  have insignificant influence on  $\langle r_\mu \rangle$ . Uncorrelated opposite systematics of order of 2.5% can generate a systematic uncertainty on  $\langle r_\mu \rangle$  of the same order of the separation between the hadronic interaction models. This means that for a realistic application of  $r_\mu$  analysis, the systematic uncertainties on the muon densities measured by the two detectors have to be correlated (more realistic case). If the systematic uncertainties of the two detectors are in opposite directions (less realistic case) they have to be smaller than 2.5% in order to keep the discrimination power of the hadronic interaction models.

It was also shown that  $r_\mu$  is a very robust parameter which can be used irrespective of ignorance of the primary mass composition to test the hadronic interaction models. Constraints imposed by an analysis based on  $r_\mu$  can in a short period of time contribute to the

solution of the know problems with muon production in extensive air shower [20,21].

## Acknowledgements

The authors would like to thank Roger Clay for the review of the manuscript on behalf of the Pierre Auger Collaboration. RRP thanks the financial support given by FAPESP (2014/10460-1). VdS thanks the support of the Brazilian population via CNPq and FAPESP (2015/15897-1, 2014/19946-4).

## References

- [1] K.-H. Kampert, M. Unger, Measurements of the cosmic ray composition with air shower experiments, *Astropart. Phys.* 35 (10) (2012) 660–678, doi:[10.1016/j.astropartphys.2012.02.004](https://doi.org/10.1016/j.astropartphys.2012.02.004).
- [2] R. Engel, D. Heck, T. Pierog, Extensive air showers and hadronic interactions at high energy, *Annu. Rev. Nucl. Part. Sci.* 61 (1) (2011) 467–489, doi:[10.1146/annurev.nucl.012809.104544](https://doi.org/10.1146/annurev.nucl.012809.104544).
- [3] D. Heck, et al., CORSIKA: A Monte Carlo Code to Simulate Extensive Air Showers, Technical Report FZKA 6019, Forschungszentrum Karlsruhe GmbH, Karlsruhe, 1998.
- [4] S. Ostapchenko, Monte Carlo treatment of hadronic interactions in enhanced Pomeron scheme: QGSJET-II model, *Phys. Rev. D* 83 (1) (2011) 014018, doi:[10.1103/PhysRevD.83.014018](https://doi.org/10.1103/PhysRevD.83.014018).
- [5] K. Werner, T. Pierog, Extended air shower simulations using EPOS, in: AIP Conference Proceedings, 928, AIP, 2007, pp. 111–117, doi:[10.1063/1.2775903](https://doi.org/10.1063/1.2775903).
- [6] T. Pierog, I. Karpenko, J.M. Katzy, E. Yatsenko, K. Werner, EPOS LHC: Test of collective hadronization with data measured at the CERN large hadron collider, *Phys. Rev. C* 92 (2015) 034906, doi:[10.1103/PhysRevC.92.034906](https://doi.org/10.1103/PhysRevC.92.034906).
- [7] F. Riehn, R. Engel, A. Fedynitch, T.K. Gaisser, T. Stanev, A new version of the event generator Sibyll, in: Proceedings of the 34th International Cosmic Ray Conference (ICRC), The Hague, Netherlands, 2015, p. 558.
- [8] A. Ferrari, P.R. Sala, A. Fasso, J. Ranft, FLUKA: A Multi-Particle Transport Code, Technical Report CERN-2005-10 (2005), INFN/TC\_05/11, SLAC-R-773,
- [9] H.C. Fesefeld, Simulation of Hadronic Showers, Physics and Applications, Technical Report PITHA 85-02, RWTH, Aachen, Germany, 1985.
- [10] M. Bleicher, E. Zabrodin, C. Spieles, S.A. Bass, C. Ernst, S. Sof, L. Bravina, M. Belkacem, H. Weber, H. Stöcker, W. Greiner, Relativistic hadron-hadron collisions in the ultra-relativistic quantum molecular dynamics model, *J. Phys. G* 25 (1999) 1859, doi:[10.1088/0954-3899/25/9/308](https://doi.org/10.1088/0954-3899/25/9/308).
- [11] C. Meurer, J. Blumer, R. Engel, A. Haungs, M. Roth, Muon production in extensive air showers and its relation to hadronic interactions, *Czech. J. Phys.* 56 (1) (2006) A211–A219, doi:[10.1007/s10582-006-0156-9](https://doi.org/10.1007/s10582-006-0156-9).
- [12] R. Engel, for the Pierre Auger Collaboration, upgrade of the Pierre Auger Observatory (AugerPrime), in: Proceedings of the 34th International Cosmic Ray Conference (ICRC), The Hague, Netherlands, 2015, p. 686.
- [13] A. Aab, et al. (The Pierre Auger Collaboration), The Pierre Auger Observatory Upgrade - Preliminary Design Report (2016).
- [14] J.G. Gonzalez, R. Engel, M. Roth, Mass composition sensitivity of combined arrays of water cherenkov and scintillation detectors in the EeV range, *Astropart. Phys.* 74 (2016) 37–46, doi:[10.1016/j.astropartphys.2015.09.003](https://doi.org/10.1016/j.astropartphys.2015.09.003).
- [15] F. Sanchez, For the Pierre Auger Collaboration, in: Proceedings of the 32nd International Cosmic Rays Conference (ICRC), Beijing, China, 2011.
- [16] A. Aab, et al., (The Pierre Auger Collaboration), prototype muon detectors for the AMIGA component of the pierre auger observatory, *J. Instrum.* 11 (02) (2016) P02012, doi:[10.1088/1748-0221/11/02/P02012](https://doi.org/10.1088/1748-0221/11/02/P02012).
- [17] A.D. Supanitsky, A. Etchegoyen, I. Allekotte, M.G. Berisso, M.C. Medina, Underground muon counters as a tool for composition analyses, *Astropart. Phys.* 29 (2008) 461–470, doi:[10.1016/j.astropartphys.2008.05.003](https://doi.org/10.1016/j.astropartphys.2008.05.003).
- [18] D. Ravignani, A.D. Supanitsky, A new method for reconstructing the muon lateral distribution with an array of segmented counters, *Astropart. Phys.* 65 (2015) 1–10, doi:[10.1016/j.astropartphys.2014.11.007](https://doi.org/10.1016/j.astropartphys.2014.11.007).
- [19] D. Ravignani, A.D. Supanitsky, D. Melo, Reconstruction of air shower muon densities using segmented counters with time resolution, *Astropart. Phys.* 82 (2016) 108–116, doi:[10.1016/j.astropartphys.2016.06.001](https://doi.org/10.1016/j.astropartphys.2016.06.001).
- [20] A. Aab, et al., (The Pierre Auger Collaboration), muons in air showers at the pierre auger observatory: mean number in highly inclined events, *Phys. Rev. D* 91 (2015) 032003, doi:[10.1103/PhysRevD.91.032003](https://doi.org/10.1103/PhysRevD.91.032003).
- [21] A. Aab, et al., (The Pierre Auger Collaboration), Testing hadronic interactions at ultrahigh energies with air showers measured by the pierre auger observatory, *Phys. Rev. Lett.* 117 (19) (2016) 192001, doi:[10.1103/PhysRevLett.117.192001](https://doi.org/10.1103/PhysRevLett.117.192001).



# 7 Hadron production in pion-carbon interactions

## (TO REVIEW)

In this chapter we present the analysis of hadron production in  $\pi^-$ -C interactions measured by the NA61/SHINE experiment at CERN SPS. In Sec. 3.1.2 we have stressed the importance of  $\pi^\pm$ -air interactions for the air shower development and, in particular, for the muon production. The carbon target was selected here because of its similarity with air nuclei in terms of nuclear mass.

Our goal is to measure the production spectra of  $\pi^\pm$ ,  $K^\pm$ ,  $p(\bar{p})$ ,  $\Lambda(\bar{\Lambda})$  and  $K_S^0$ . Although our measurements of the  $p(\bar{p})$  spectra can impact directly the current understanding of the air shower physics, all the particle spectra measured here will be surely valuable for the testing of the hadronic interaction models and for the tuning of their next generation. Besides that, the  $\Lambda(\bar{\Lambda})$  and  $K_S^0$  spectra have also an important role on reducing the systematic uncertainties on the  $p(\bar{p})$  one.

The unprecedent  $\pi^-$ -C data analyzed here was taken by the NA61/SHINE detector at two beam energies, 158 and 350 GeV/c. Its large acceptance that covers a large region of the forward phase space makes the NA61/SHINE the ideal detector for this kind of study. A previous analyze of the  $\pi^-$ -C data with the measurements of resonance mesons was published in Ref. [2]. In particular, the measured  $\rho^0$  spectra also has a great impact on air shower physics.

The analysis presented in this chapter can be essentially split in two parts. One of them is dedicated to the measurements of the  $\pi^\pm$ ,  $K^\pm$  and  $p(\bar{p})$  spectra and the other to the  $\Lambda(\bar{\Lambda})$  and  $K_S^0$  spectra. The former will be labelled along the text as the *charged hadron analysis* and its most challenging step includes the particle identification through the measurements of the deposit energy of the particles. On the other hand, the analysis of the latter group of particles will be labelled by  *$V^0$  analysis*, being the signal extraction based on  $m_{\text{inv}}$  spectra the most challenging step. Although the two analysis were in practice done separately, the analysis steps that are conceptually the same will be presented here only once.

The charged hadron analysis was already in development at the time this work started. The previous stages of the analysis can be seen in Refs. [3–6]. Particularly, the event and track selection used here was based on previous works of Martin Ruprecht [1] and the  $dE/dx$  fit strategy was based on previous works of Hans Dembinski. Concerning the  $V^0$  analysis, there was no previous development and the role analysis was done by

the author of this thesis, in collaboration with Michael Unger. A preliminary stage of the present analysis was published in Ref. [7].

## 7.1 NA61/SHINE experiment

(TO REVIEW)

(more references)

The NA61/SHINE [8] is a fixed target experiment located in the North Area of the CERN SPS. Its proposal was accepted in 2006, a pilot run took place in 2007 and the first physics run in 2009. Most of its detector components were inherited from the NA49 experiment [9], which was shut down in 2003.

The physics programme of NA61/SHINE is very rich, including heavy ion, neutrino and cosmic ray physics. All these different fields have in common the need for precise hadron production measurements, which can be provided by NA61/SHINE experiment. The main goals of the heavy ion programme is the study of the properties of the onset of deconfinement (discovered by NA49 []) and the search for the critical point of strongly interacting matter []. Concerning the neutrino physics programme, the hadron production spectra in hadron-nucleus collisions measured by NA61/SHINE are required to improve the neutrino flux predictions for the T2K experiment [10]. Finally, the goal of the cosmic rays physics programme is to study the properties of the  $\pi$ -C interactions, which is of highly value for the better understanding of the extensive air shower physics and, in particular, the muon production (see Chap. 3 for more details).

Its large acceptance is the main experimental feature of the NA61/SHINE detector. A set of five Time Projection Chambers (TPCs) can provide a high efficiency charged particle tracking. A magnetic field partially covering the TPCs allows the reconstruction of the particle momenta and charge while the energy loss measurements by the TPCs allows for the particle identification. In Fig. 1 we show the configuration of the beam detectors as set for the  $\pi^-$ -C data taken and in Fig. 2 we show the configuration of the main part of the NA61/SHINE detector. The coordinate system used in all NA61/SHINE analysis is also shown in Fig. 2. The axis defined by the beam direction is represented by the z coordinate, while the x-y plane is the perpendicular to this direction.

A brief description of the beam and the detector components relevant for the present analysis follows in the next sections. Some important components, like the Time-of-Flight detectors, are not described here for the sake of brevity. A detailed description of the experiment is given in Ref. [8].

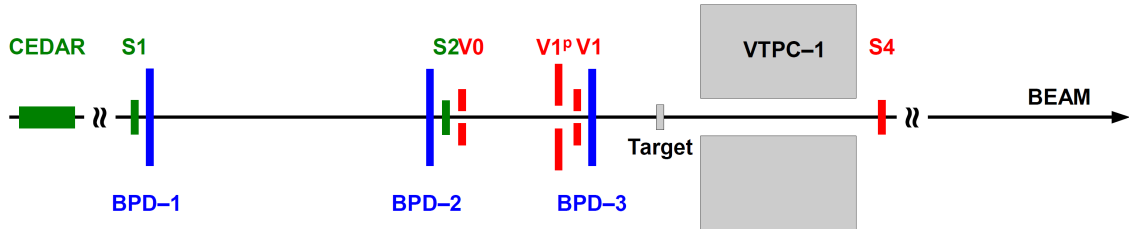


Figure 1

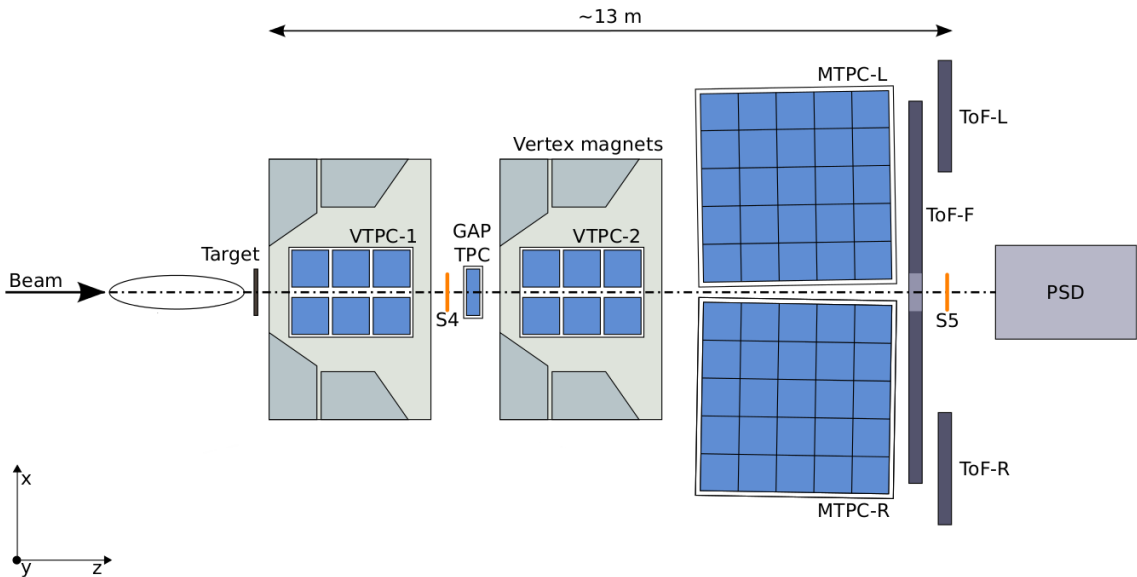


Figure 2

### 7.1.1 Beam

The CERN SPS is able to provide to the North Area experiments primary proton or ion beams of maximum energy of 450 GeV/u. To generate the  $\pi^-$  secondary beam, a primary proton beam of 400 GeV/c from SPS is first collided against a 10 cm long beryllium target. This collision occur about 500 m upstream the NA61/SHINE detector.

The secondary charged particles produced are then transported through the H<sub>2</sub> beamline. During the transportation, a number of collimators and magnets are responsible for selecting the momentum of the beam particles as well as controlling their intensity and trajectory. For the data analyzed in this work, the  $\pi^-$  beam was generated with two beam momenta, 158 and 350 GeV/c.

### 7.1.2 Beam detectors and trigger system

The beam detectors and the components of the trigger system are shown in Fig. 1. Most of them are placed upstream of the target, being the S4 the only exception. A set of three plastic scintillation counters are labelled as S1, S2 and S4. The components V0, V1 and V1<sup>p</sup> are called veto detectors and they are also scintillation counters but with a role in

the beam trajectory. These veto detectors are used in the trigger system in anti-coincidence so the beam particles that pass away from the expected beam trajectory are removed.

Two trigger modes defined based on the scintillation counter measurements are relevant for this work. The first one is the *beam trigger*, denoted in this text as T1 and defined as  $S1 \wedge S2 \wedge \overline{V0} \wedge \overline{V1} \wedge \overline{V1^p}$ , which means that S1 and S2 are considered in coincidence and V0, V1 and  $V1^p$  in anti-coincidence. The second relevant trigger is the *interaction trigger*, denoted as T2 and defined as  $T1 \wedge \overline{S4}$ . The S4 detector in anti-coincidence removes events in which a beam particle crossed the target without interacting. Evidently, a small fraction of the inelastic interactions can produce a high energy particle that reaches S4 and in these cases, the event is not accepted. The consequent biased is taken into account on the Monte Carlo correction step (see Sec. 7.7).

The three Beam Position Detectors, indicated as BPD in Fig. 1, are proportional chambers that are able to measure the transversal position of the beam particles. Two important functions of the BPDs are to constrain the transversal position of the interaction vertex and to define the incident angle of the beam particle on the target. Besides that, the information about the spread of the beam particles on the transverse plane is used as a offline cut to assure the selection of good quality events (see Sec. 7.3).

A further beam detector is the CEDAR, that is also shown in Fig. 1. It is a Cherenkov detector and its functionality is to identify the beam particle. After the secondary beam particles are selected and transported to the NA61/SHINE detector, the purity of the  $\pi^-$  beam is about 95% and 100% for the 158 and 350 GeV/c case, respectively. The CEDAR information is also used as an offline cut to assure that the interacting particle is indeed a  $\pi^-$ .

### 7.1.3 Time projection chambers

In Fig. 2 one can see the position of the five TPCs, which form the main part of the NA61/SHINE detector. Two of them are the vertex TPCs, called VTPC-1 and VTPC-2. Placed in between VTPC-1 and VTPC-2 there is the GAP-VTPC (or only GTPC). The two remain ones are the left and right components of the main TPCs, which are called MTPC-L and MTPC-R.

The VTPC-1 and VTPC-2 are located inside two superconducting dipole magnet. The produced magnetic field is responsible for bending the particle trajectories, which allows us to measure the sign of the particle charge as well as the its momentum. To optimize the geometrical acceptance, the intensity of the magnetic field is set depending on the beam energy. For the  $\pi^-$ -C data taken at 158 and 350 GeV/c, the magnetic field was set to 1.5 and 1.1 T in te first and second magnets, respectively.

All the TPCs are filled with a gas mixture of Ar/CO<sub>2</sub> in the proportion of 90/10

for the VTPCs and GPTC and 95/5 for the MTPCs. The particle tracking is possible by collecting the electrons freed by the ionization of the gas atoms because of the passage of the charged particle. These electrons are drifted along the  $y$  direction under the influence of the electric field and collected by a set of readout pads on the top of the TPCs. The electrons collected in the pads are grouped in time to form the so-called clusters. While the position of the pads gives the  $x$  and  $z$  coordinates of the cluster position, the  $y$  coordinate is reconstructed by its drifting time. By combining the position of many clusters measured along the TPCs, we can reconstruct the trajectory of the charged particles. The combination of the clusters associated to one particle is called track.

Besides the particle tracking, the TPCs can also measure its ionization energy loss. These measurements are done by combining the total charge of all the clusters that compose a track and a unique value of  $dE/dx$  is defined for each particle. The  $dE/dx$  measurements allow the main particle identification procedure applied in NA61/SHINE analysis and we give more details about that in Sec. 7.5.2. A technical description of the TPCs of the NA61/SHINE can be found in Refs. [8, 11].

## 7.2 Data and simulation sets

(DONE)

The  $\pi^- + C$  data were collected by NA61/SHINE in 2009 at two beam energies: 158 and 350 GeV. The carbon target consisted of an isotropic graphite plate with 2 cm thickness along the beam axis, with density of  $\rho = 1.84 \text{ g/cm}^3$ . The target position was set to 80 cm upstream of VTPC-1. To estimate the contribution of interactions that occur with the detector material, about 10% of the data were taken with the target removed. In Sec. 7.8 we describe the procedure used to subtract the effect of the out-of-target interactions from the measured spectra. The calibration of the  $\pi^- + C$  data followed the standard NA61/SHINE procedure, described in Ref. [12].

The Monte Carlo simulation sets used in this analysis were created by first generating the primary interactions using hadronic interaction models and then by passing the produced particles through a detailed detector simulation based on GEANT3 (???) package [13]. Three hadronic interaction models were used: EPOS 1.99 [14], DPMJET 3.06 [15] and QGSJET II-04 [16]. For each beam energy and hadronic interaction model, a simulation set was produced with approximately the same number of events as in data. Both data and simulations were reconstructed by the standard NA61/SHINE reconstruction chain [17].

## 7.3 Event selection

(DONE)

The event selection can be divided into upstream and event cuts. The upstream cuts are based on the beam detector measurements and, since these detectors are not implemented in the Monte Carlo simulations, these cuts were applied only to the data. The upstream cuts are:

- (i) the CEDAR cut to identify the beam particle type and then remove the contributions from non-pion particles;
- (ii) the WFA cut that uses the time information from the S1 detector to exclude events in which a second beam particle was detected within a time interval shorter than 2  $\mu\text{s}$ ;
- (iii) the BPD cut that uses the information from the three BPD detectors to assure a good quality measurements of the beam position at the target plan.

More details about the upstream cuts can be found in Ref. [1].

The event cuts that were applied to both data and simulations are:

- (i) the trigger cut to select events of the T2 type (see Sec. 7.1.2 for the trigger definitions);
- (ii) the main vertex cut to remove events in which the main vertex was not properly fitted in the event reconstruction;
- (iii) the main vertex z-position cut to remove events in which the z coordinate of the fitted main vertex is farer than 17 cm from the main vertex position measured by the BPD detectors.

The main vertex z-position cut (item (iii)) was applied to reduce the contribution of interactions that occur out of the target. Because of the resolution on the fitted main vertex z position, a small fraction of interaction which occurred in the target are also removed by this cut. This bias effect is estimated and corrected in the Monte Carlo correction step (see Sec. 7.7). In Tab. 1 we show the number of events after the event selection for the data and simulation sets.

## 7.4 Phase space binning

(DONE)

Both charged hadron and  $V^0$  analysis were performed by splitting the data into 2-dimensional phase space bins of the  $p$  and  $p_T$  variables. For the charged hadron analysis an unique phase space binning was defined. The  $p$  intervals are nearly uniform in  $\log p$ . Only small adjustments were done to move the crossing points of the energy deposit function of different particles closer to the center of the bins. Since some of these bins

Table 1 – Number of events after the event selection for the data and simulation sets and for both beam momenta, 158 and 350 GeV/c.

	158 GeV/c	350 GeV/c
Data (target inserted)	$2.78 \times 10^6$	$2.59 \times 10^6$
Data (target removed)	$6.80 \times 10^3$	$6.12 \times 10^3$
EPOS 1.99	$3.59 \times 10^6$	$3.04 \times 10^6$
DPMJET 3.06	$3.89 \times 10^6$	$3.46 \times 10^6$
QGSJET II-04	$3.56 \times 10^6$	$2.95 \times 10^6$

in the crossing regions will be removed from the analysis (see Sec. 7.5.6), this strategy has shown effective to reduce the number of removed bins. The average width of the  $p$  intervals is  $\Delta \log p = 0.1$ . Concerning the  $p_T$  intervals, the bin width increases with  $p_T$ , being the width of the shorter and the longer ones  $\Delta p_T = 0.1$  and  $\Delta p_T = 0.5$ , respectively. In Fig. 3 we show the phase space binning used for the charged hadron analysis.

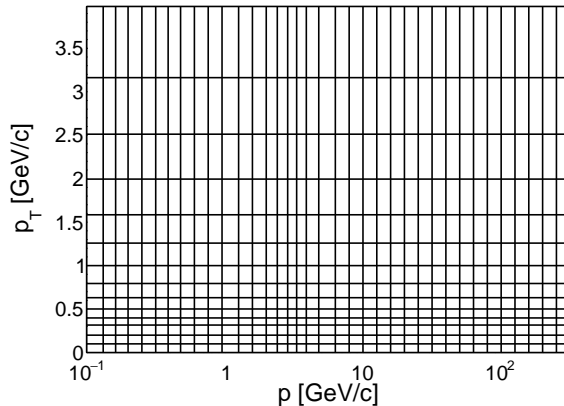


Figure 3 – Illustration of the phase space binning used for the charged hadron analysis.

Because the  $V^0$  analysis is done independently for the three target particles, the phase space binning is not required to be unique. However, because the statistics is similar for  $\Lambda$  and  $\bar{\Lambda}$ , the same binning was define for these two particles. For either  $\Lambda(\bar{\Lambda})$  or  $K_S^0$  the  $p$  intervals vary from  $\Delta \log p = 0.2$  to 0.3. Concerning the  $p_T$  intervals, the widths vary from  $\Delta p_T = 0.2$  to 0.8. In Fig. 4 we show the binning used for the  $V^0$  analysis.

## 7.5 Particle identification for the charged hadron analysis

### (DONE)

In this section we present the particle identification analysis to obtain the spectra of  $\pi^\pm$ ,  $K^\pm$  and  $p(\bar{p})$ . This step is done in a track basis through the  $dE/dx$  measurements, being the aim here to determine the fraction of tracks which correspond to each particle type on every phase space bin. The track selection is first described in Sec. 7.5.1 and a brief overview of the  $dE/dx$  measurements is then given in Sec. 7.5.2.

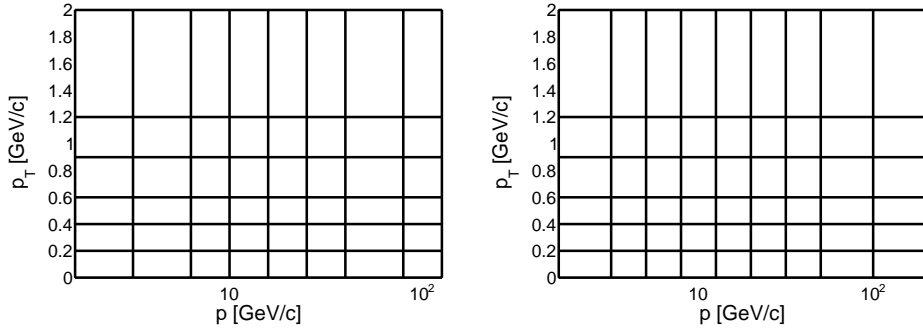


Figure 4 – Illustration of the phase space binning used for the  $V^0$  analysis. The plot on the left show the binning used for  $\Lambda$  and  $\bar{\Lambda}$  and the plot on the right show the binning used for  $K_S^0$ .

The  $dE/dx$  measurements only allow the particle identification to be done statistically by fitting the  $dE/dx$  distributions with a combination of particle types. Because of the complicated dependence of the  $dE/dx$  distributions on the particle momentum, track properties (e.g. number of clusters) and detector properties (e.g. resolution and calibration), the  $dE/dx$  fit turns to be a very challenging step. The first requirement to perform it is the development of an appropriate  $dE/dx$  model, described in Sec. 7.5.3.

Having in hands the  $dE/dx$  model, the measured  $dE/dx$  distributions can be fitted to determine the particle fractions. However, the usual large number of model parameters, added to the overlap of the  $dE/dx$  distributions of different particles in certain phase space regions, can make this fit very hard to perform. Our fit strategy developed to overcome these difficulties is shown in Sec. 7.5.4 and the results of the fit in Sec. 7.5.5. A new tool developed in this work to evaluate the fit performance and estimate bias and statistical uncertainties of the fit is presented in Sec. 7.5.6. This tool is called Simulated Data Emsembles and it is also used to define cuts on problematic phase space bins and to compute correction factors. Finally, in Sec. 7.5.7 we show the results of the particle identification analysis, including the particle fractions of  $\pi^\pm$ ,  $K^\pm$  and  $p(\bar{p})$ .

### 7.5.1 Track selection

#### (DONE)

A set of selection criteria were applied to the measured tracks aiming to ensure the quality of their reconstruction. The list of selection criteria is the following.

- (i) The reconstructed track must be contained in the detector acceptance, that is defined based on two criteria. First, Monte Carlo simulations are used to define regions of the  $(\phi, p, p_T)$  phase space in which the selection efficiency is larger than 90%. Second, the measured tracks are used to define regions of the same phase space in which the tracks hit directly the S4 detector [1].

- (ii) The total number of clusters on the track must be greater than or equal to 25.
- (iii) The sum of clusters on both VTPCs must be greater than or equal to 12, or the number of cluster on the GTPC must be greater than or equal to 6.
- (iv) The distance between the extrapolated track to the interaction plane and the interaction point must be smaller than 4 cm on the both horizontal and vertical plane.

The acceptance selection (item (i)) is important because it was observed that the Monte Carlo simulations cannot describe accurately the detector efficiency in the phase space regions in which this efficiency is relatively low (<90%). Since the detector acceptance is the dominant effect to be corrected at the Monte Carlo correction step, this discrepancy between data and simulations could significantly bias the resultant spectra if the acceptance selection was not applied.

After the track selection, the measured tracks were split into two subsets called Right Side Tracks (RST) and Wrong Side Tracks (WST). The former group is defined as the tracks that bend away from the beam axis, while the latter as the tracks that bend towards the beam axis. Given the track  $\phi$  angle and its charge  $q$ , the two groups can be defined by the sign of the product  $q \times \cos(\phi)$ , where RST have positive sign and WST have negative ones. The distinction between this two track topologies is motivated by the fact that a right and a wrong side track with the same  $p$  and  $p_T$  cross different regions of the detector, which in turn have important implications on the particle identification step based on the  $dE/dx$  measurements (see Sec. 7.5). In Fig. 5 we illustrate the RST and WST definitions.

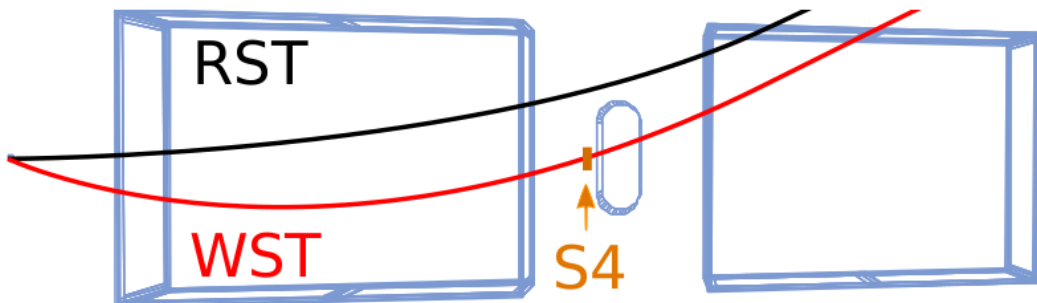


Figure 5 – (DO IT) [1]

### 7.5.2 $dE/dx$ measurements

(DONE)

The  $dE/dx$  is defined as the energy lost by the particle to the medium per unit of length. In NA61/SHINE, the  $dE/dx$  is measured by the TPCs, which collect the freed

electrons from the ionization of the gas by the passage of the charged particles. The determination of the  $dE/dx$  from the signal recorded at the TPCs requires a complex and detailed procedure that has been very well established by the NA49 and NA61/SHINE experiment along the last decades. Since the detailed description is out of the scope of this text, only the general idea and the most important aspects will be presented in the next paragraphs. More complete and detailed approaches can be found in Refs. [18–20].

Several processes can contribute to the energy loss of charged particle due to its interaction with atoms of the gas in the TPCs, being the emission of electrons by ionization the most relevant one. The electrons emitted are drifted through the chamber and collected in the readout pads, which records the signal as ADC charges. A cluster is defined as a set of consecutive charges. The total charge measured for each cluster is related to the  $dE/dx$  of each track. However, numerous detector effects have to be corrected at the cluster level before grouping the clusters in one unique  $dE/dx$  value. The simplest correction accounts for the geometrical differences due to the particle incident angle in the pad and the pad widths. More complicated corrections account for differences in the electronic gain and gas pressure/temperature of the pads, differences in the sector gains and losses of electrons during the drift in the chambers and in the readout pad. A detailed description of the correction procedure can be found in Ref. [21].

The track  $dE/dx$  is then determined by the combination of the corrected charges from all track clusters. Because of the well known Landau-like shape of the energy loss probability distribution, the average and the variance of the measured charges are not well behaved for typical number of clusters ( $\sim 20\text{--}150$ ). This makes the simplest approach, by defining the track  $dE/dx$  as the average charge over all cluster, not suitable. To overcome this issue and to obtain a satisfactory  $dE/dx$  resolution, the method of the truncated mean is applied, in which only a subset of the clusters is selected to compute the average. The selected clusters are defined by ordering the values of the charge and then selecting the ones inside a given fractional interval. For the NA61/SHINE experiment it was found the optimal interval being the 50% of the clusters with the smallest charges [20].

It is important to point out that, although the  $dE/dx$  associated to a track is proportional to the energy lost by the particle, these two quantities are not exactly the same. This means that the measured  $\langle dE/dx \rangle$  as a function of  $p$  does not follow the expected Bethe-Bloch function, but it does behave in a very similar way. Because of this similarity, the functional form of the Bethe-Bloch function is used here to parametrize the  $\langle dE/dx \rangle$  evolution with  $p$ . In Fig. 6 we show the distribution of the measured  $dE/dx$  as a function of the track  $p$  together with the  $\langle dE/dx \rangle$  parametrization for several particle types. This parametrization was developed for this analysis and it is an important element for the  $dE/dx$  model and the  $dE/dx$  fit presented in Secs. 7.5.3 and 7.5.4.

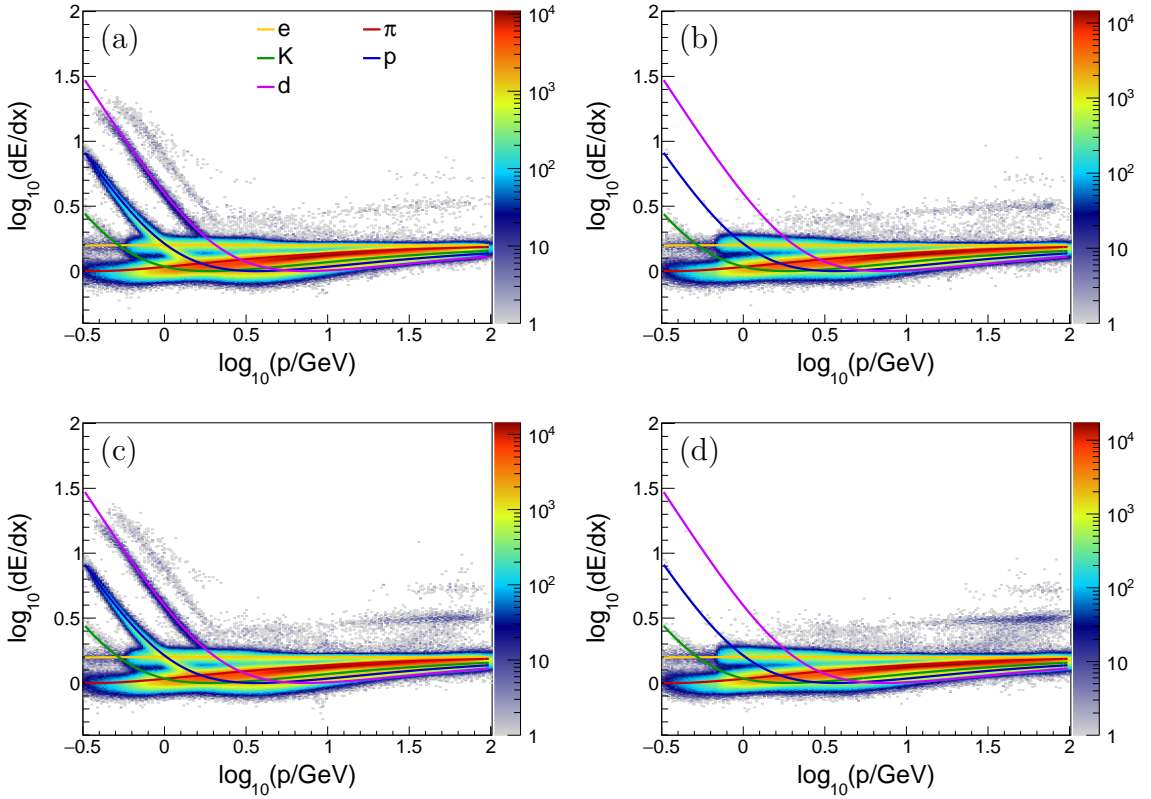


Figure 6 –  $dE/dx$  data used in this analysis. Positively and negatively charged tracks are shown respectively in (a) and (b) for the  $158 \text{ GeV}/c$  data set, and in (c) and (d) for the  $350 \text{ GeV}/c$  one. The solid curves show the  $\langle dE/dx \rangle$  parametrization for each particle type. (**noise rejection**)

### 7.5.3 $dE/dx$ model

(**DONE**)

To perform the  $dE/dx$  fit, a model to describe the  $dE/dx$  distributions of different particle types as a function of their momenta is required. While experiments like ALICE [22] and CMS [23] opt for modeling the  $dE/dx$  distributions with templates [24, 25], the NA49 and NA61/SHINE experiments traditionally adopt an analytic model, which will also be adopted by us. Although the model chosen for our analysis is based on previous studies from NA49 and NA61/SHINE collaborations [19, 20], it contains particular features that we have found to be the most suitable for the present analysis.

For clarification, we first present the notation adopted along this text. The particle types are represented by the index  $i$ , which can be one of the five particles  $i = e, \pi, K, p$  or  $d$ . The positive and negative charges are indexed by  $j$ , so that  $j = +$  or  $-$ . In addition,  $n_{\text{cl}}$  is used to represent the number of cluster of a track and the  $dE/dx$  is replaced by  $\varepsilon$  for shortening.

The first element of our  $dE/dx$  model is the probability density function of  $\varepsilon$  for a given particle type and charge, which is called here  $f_{i,j}(\varepsilon)$ . Because  $\varepsilon$  is obtained by

averaging the measured charge over a certain number of clusters, it is natural to assume that the shape of  $f_{i,j}(\varepsilon)$  depends on  $n_{\text{cl}}$ . To be more precise, the width of  $f_{i,j}(\varepsilon)$  (or the  $\varepsilon$  resolution) should decrease with increasing  $n_{\text{cl}}$ , and vice-versa. Furthermore, the mean of  $f_{i,j}(\varepsilon)$  is expected to evolve with the particle momentum  $p$  by following a Bethe-Bloch-like function. Given its  $n_{\text{cl}}$  and  $p$  dependences,  $f$  can be taken as a conditional probability function, so it can be written as  $f_{i,j}(\varepsilon|p, n_{\text{cl}})$ .

It has been verified that  $f_{i,j}(\varepsilon|p, n_{\text{cl}})$  can be well represented by an asymmetric Gaussian function [20]. Thus, we can write

$$f_{i,j}(\varepsilon|p, n_{\text{cl}}) = \frac{1}{\sqrt{2\pi}\sigma_{i,j}} \exp \left[ -\frac{1}{2} \left( \frac{\varepsilon - \mu_{i,j}}{\delta \sigma_{i,j}} \right)^2 \right], \quad (7.1)$$

with

$$\delta = \begin{cases} 1-d, & \varepsilon \leq \mu_{i,j} \\ 1+d, & \varepsilon > \mu_{i,j}, \end{cases} \quad (7.2)$$

where  $\mu$  is the mode of the distribution,  $\sigma$  is its resolution and  $d$  is the asymmetry parameter. The  $p$  and  $n_{\text{cl}}$  dependence are implicit on the parameters  $\mu$  and  $\sigma$ , as will be explained next. The mode  $\mu$  is related to the mean of  $\varepsilon$  ( $\langle \varepsilon \rangle$ ) by

$$\mu_{i,j} = \langle \varepsilon \rangle_{i,j} - \frac{\sigma_{i,j}}{\sqrt{2\pi}} \left[ (1+d)^2 - (1-d)^2 \right]. \quad (7.3)$$

The Bethe-Bloch parametrizations shown as colored curves in Fig. 6 give the  $\langle \varepsilon \rangle$  as a function of  $p$  for a given particle type. In this model, this parametrization is used for reference and the value of  $\langle \varepsilon \rangle$  from the parametrization is denoted by  $\langle \varepsilon \rangle^{\text{BB}}$ . To account for deviations from  $\langle \varepsilon \rangle^{\text{BB}}$ , our model includes a set of parameters called *calibration constants*, which are denoted by  $X$ . These parameters act as logarithmic shifts of the  $\langle \varepsilon \rangle$  around  $\langle \varepsilon \rangle^{\text{BB}}$  and they can in principle be applied to each particle and charge separately. However, to reduce the complexity of the model, we assume one global calibration constant for each charge that follows the  $\langle \varepsilon \rangle$  of the  $\pi$  distribution and individual calibration constants for the other particle types, which are common for both charges. The  $\langle \varepsilon \rangle$  for a given  $i$  and  $j$  is then given by

$$\langle \varepsilon \rangle_{i,j} = \begin{cases} \langle \varepsilon \rangle_i^{\text{BB}} e^{X_i^j} & (i = \pi) \\ \langle \varepsilon \rangle_i^{\text{BB}} e^{X_\pi^j} e^{X_i^j} & (i \neq \pi). \end{cases} \quad (7.4)$$

In total, the model includes 6 calibration constants:  $X_\pi^+$ ,  $X_\pi^-$ ,  $X_e$ ,  $X_K$ ,  $X_p$  and  $X_d$ . The  $\langle \varepsilon \rangle$  from Eq. (7.4) is used in Eq. (7.3) to compute  $\mu_{i,j}$ , which is in turn used in Eq. (7.1) to compute  $f_{i,j}(\varepsilon|p, n_{\text{cl}})$ .

The last ingredient of Eq. (7.1) to be described is the resolution  $\sigma_{i,j}$ . Its  $n_{\text{cl}}$  dependence is assumed to be of the form  $\sigma \sim 1/\sqrt{n_{\text{cl}}}$ . Besides that  $\sigma_{i,j}$  is also assumed to depend on the  $\langle \varepsilon \rangle$  by a power law relation. The overall scale of  $\sigma_{i,j}$  is given by its

normalization parameter  $\sigma_0$ , which is actually defined separately for each charge ( $\sigma_0^j$ ). The final expression for the resolution is,

$$\sigma_{i,j} = \frac{\sigma_0^j}{\sqrt{n_{\text{cl}}}} \langle \varepsilon \rangle_{i,j}^\alpha, \quad (7.5)$$

in which 3 more parameters are included to the model:  $\sigma_0^+$ ,  $\sigma_0^-$  and  $\alpha$ .

By combining Eqs. (7.2) to (7.5) with the Eq. (7.1), we obtain the probability density function of  $\varepsilon$  for each particle  $i$  and charge  $j$ . Apart from the 6 calibration constants, the model also includes a set of 4 *shape parameters*:  $\sigma_0^+$ ,  $\sigma_0^-$ ,  $\alpha$  and  $d$ . Altogether, there are 10 parameters that can be used as free parameters to perform the fit of the  $\varepsilon$  distributions.

#### 7.5.4 $dE/dx$ fit strategy

##### (DONE)

The fitting procedure is performed by means of a binned maximum-likelihood method. In the general case 10 particle fractions (5 particle types and 2 charges) and 10 model parameters are taken as free parameters of the fit. Special cases in which one or more particle fraction are fixed to zero will be described later.

The  $\varepsilon$  data is first divided in bins of  $\log_{10}\varepsilon$  of width  $\Delta \log_{10}\varepsilon = 0.01$ . The index  $k$  will be used to indicate these  $\log_{10}\varepsilon$  bins. By using the standard Poissonian probability distribution function in which  $n_{j,k}$  and  $\nu_{j,k}$  are the observed and expected number of tracks in a given bin  $k$  and charge index  $j$ , the log-likelihood is then written as

$$l_0 = 2 \ln L = 2 \sum_{j=+,-} \sum_{k=1}^K (\nu_{j,k} - n_{j,k} \ln \nu_{j,k}), \quad (7.6)$$

where  $K$  is the number of  $\log_{10}\varepsilon$  bins and the constant terms were neglected.

The expected number of tracks  $\nu_{j,k}$  is computed by using the  $\varepsilon$  model. Since  $f_{i,j}(\varepsilon|p, n_{\text{cl}})$  depends on  $p$  and  $n_{\text{cl}}$ , the model has to be convoluted with the  $p$  and  $n_{\text{cl}}$  distributions of the measured tracks. To do that, the measured tracks are first split in bins of the variables  $q = \log_{10} p$  and  $z = 1/\sqrt{n_{\text{cl}}}$ . These variables were chosen to provide a better sampling of the data along the bins. The distributions of the original variables,  $p$  and  $n_{\text{cl}}$ , contain undersampled tails which are not suitable for the convolution procedure.

Being  $l$  and  $m$  respectively the indexes for the bins of the variables  $q$  and  $z$ , the number of measured tracks in one  $(q,z)$  bin, for a given charge  $j$ , is denoted by  $N_{j,l,m}$  and the center of the bins are denoted by  $\hat{q}_l$  and  $\hat{z}_m$ . In the next step, the partial cumulative distribution function in one  $k$  bin relative to one  $(q,z)$  bin is computed as

$$F_{i,j,k,l,m} = \int_{\text{kth bin}} f_{i,j}(\varepsilon|\hat{q}_l, \hat{z}_m) d\varepsilon, \quad (7.7)$$

where the limits of the integral are given by the  $\log_{10}\varepsilon$  limits of the  $k$ th bin. Note that, instead of the original  $p$  and  $n_{\text{cl}}$  variables, the variables  $q$  and  $z$  were used to evaluate  $f$ .

The total cumulative distributions  $C_{i,j}$  is computed by summing the contributions of all  $(q,z)$  bins, weighted by its respective number of measured tracks, as

$$C_{i,j} = \sum_{l=1}^L \sum_{m=1}^M N_{j,l,m} F_{i,j,k,l,m}, \quad (7.8)$$

where  $L$  and  $M$  are the number of  $l$  and  $m$  bins, respectively. The number of mathematical operations in this step can become very large depending on how large are  $L$  and  $M$ . As a consequence, the computing time can be unpracticably long. On the other hand, too small number of bins can imply in an undesirable loss of precision in the results of the fit. In this works, it was found that  $L = 5$  and  $M = 15$  are suitable choices. The limits of the  $q$  and  $z$  binning were defined automatically by using the smallest and the largest values found on data.

Finally, the expected number of tracks in one  $k$  bin of charge  $j$  is computed by summing the contributions of all particle types weighted by its respective fraction  $Y_{i,j}$ ,

$$\nu_{j,k} = \sum_{i=e,\pi,K,p,d} Y_{i,j} C_{i,j}. \quad (7.9)$$

This expression is then combined to Eq. (7.6) to determine  $l_0$ .

In addition to  $l_0$ , the final log-likelihood function,  $l$ , will also include terms of Gaussian constraints for the model parameters [26]. These are, by definition, Gaussian probabilities functions that multiplies the likelihood function. In terms of the log-likelihood functions, these constraints turn into quadratic terms of the form  $[(b - b_c)/\sigma_b]^2$  added to  $l$ , where  $b$  can be one of the model parameters and  $b_c$  and  $\sigma_b$  are its estimated mean value and standard deviation, respectively. It is important to constrain the model parameters because the number of tracks in the  $\varepsilon$  distribution can be eventually very low for a number of phase space bins. In these cases, the lack of statistics combined to the large number of free parameters can make the fit impracticable if the constraints are not applied. Furthermore, the constraints are also important, even for bins with large statistics, in which the proximity of the position of  $\varepsilon$  distributions for two particles can create a partial degeneracy between the respective calibration constants, and consequently generate large instabilities in the fitting procedure.

The  $b_c$  and  $\sigma_b$  were estimated by performing the fit without including the Gaussian constraints and then evaluating the mean and standard deviation of the fitted model parameters using the phase space bins in which the fit converged properly. By construction the mean value of the calibration constants are zero. An additional term was included to constrain the difference between global calibration constants for both charges ( $X_\pi^+$  and  $X_\pi^-$ ) aiming to avoid solutions in which one of the charges is largely shifted with relation

to the other. The sum of the constraints on the model parameters are given by,

$$c_m = \left( \frac{X_\pi^+}{0.01} \right)^2 + \left( \frac{X_\pi^-}{0.01} \right)^2 + \left( \frac{X_e}{0.005} \right)^2 + \left( \frac{X_K}{0.005} \right)^2 + \left( \frac{X_p}{0.005} \right)^2 + \left( \frac{X_\pi^+ - X_\pi^-}{0.01} \right)^2 + \\ \left( \frac{\sigma_0^+ - 0.4}{0.2} \right)^2 + \left( \frac{\sigma_0^- - 0.4}{0.2} \right)^2 + \left( \frac{\alpha - 0.75}{0.1} \right)^2 + \left( \frac{d - 0.05}{0.03} \right)^2 \quad (7.10)$$

Because of the very low fraction of deuterons, their fractions ( $Y_{d,+}$  and  $Y_{d,-}$ ) may not be well determined by the fit. As a consequence, we observed that for a number of phase space bins the fitted deuteron fractions do not make physical sense, which leads to a bias on the other particle fractions. To avoid this problem, the parameters  $Y_{d,+}$  and  $Y_{d,-}$  were also constrained. Their mean value is set to zero and their standard deviation to 0.02. Since the fraction for deuterons is always expected to be smaller than 0.01, the constraints are assumed not to bias the fit, being important only to forbid non-physical results. The term added is given by

$$c_d = \left( \frac{Y_{d,+}}{0.02} \right)^2 + \left( \frac{Y_{d,-}}{0.02} \right)^2. \quad (7.11)$$

The final log-likelihood function to be maximized is then given by

$$l = l_0 + c_m + c_d, \quad (7.12)$$

where  $l_0$ ,  $c_m$  and  $c_d$  are given by Eqs. (7.6), (7.10) and (7.11).

The maximization of  $l$  was performed by using the MINUIT package [27]. When fitting models with large number of free parameters, it is important to define suitable starting parameters to assure the convergence of the maximization and reduce the computing time needed for that. The starting parameters here are defined by means of preliminary fitting phases, in which a simplified fitting procedure is performed. In the first phase, only the model parameters are set free for the likelihood maximization and the fractions are computed in each step, for a given set of model parameters, by an analytic minimization of the  $\chi^2$ . In the second phase, the model parameters are fixed to the values obtained by the solution of the first phase and the fractions are obtained by the likelihood fit, which is performed separately for each charge. The starting parameters for the main fit is given by the model parameters obtained in the first phase and the fractions obtained in the second phase.

To simplify the fit and reduce the uncertainties on the fraction of particle of interest ( $\pi^\pm$ ,  $K^\pm$  and  $p(\bar{p})$ ), the fractions of deuterons and electrons were fixed to zero for phase space bins with momentum above a certain limit. These limits were defined based on their asymptotic behavior observed by performing the fit setting all fractions free and the values are 3 and 70 GeV/c for deuterons and electrons, respectively.

The RST and WST subsets were fitted separately (see ?? for the definitions). This is motivated by the fact that, for the same phase space interval, these two types of tracks are detected by different parts of the TPCs. Since the model parameters, mainly the calibration constants, are related to detector features, it is expected that the solutions of RST and WST present differences on the fitted parameters.

Since the number of tracks measured with the target removed is too small, the fitting procedure described above is not suitable for the this dataset. The complexity of the model (or the large number of free parameters) combined with the poor statistics would strongly reduce the precision of the results, or even prevent the convergence of the maximization algorithm. To overcome this problem, the particle fractions from the target removed data were obtained by means of  $\chi^2$  minimization, in which all the model parameters were fixed to the value obtained from the target inserted dataset fit. Since the model prediction is linear on the particle fraction, the minimization could be performed analytically.

### 7.5.5 $dE/dx$ fit results

#### (TO REVIEW)

Examples of the fitted  $dE/dx$  distributions are shown in Figs. 7 and 27. Although the fit was performed by the maximum likelihood method, the  $\chi^2/\text{ndf}$  can still be used to evaluate the goodness of fit. In Figs. 8 and 28, we show the  $\chi^2/\text{ndf}$  distributions. One can see that the  $\chi^2/\text{ndf}$  follow the expected trend, with average value around 1 and few bins with  $\chi^2/\text{ndf} \sim 2 - 2.5$ . Therefore, we conclude that the  $dE/dx$  model provides a good description of the data.

Examples of the calibration constants obtained by the fit of the RST and 158 GeV/c data set are shown in Fig. 9. The remaining cases are shown in Figs. 29 to 31. As expected, in general they exhibit small deviations from zero. Furthermore, we can observed a systematic dependence with the phase space region, in particular with  $p_T$ . This dependence makes evident that there is indeed small differences on the  $dE/dx$  calibration in different regions of the TPCs. Therefore we can conclude that a single Bethe-Bloch parametrization, would not provide a suitable description of the  $dE/dx$  data, thus justifying the cinlusion of the calibration constants. Addionally, the RST and WST results are different, which proves the necessity of performing the  $dE/dx$  fit separately for both data sets.

Examples of the shape parameters for the RST and 158 GeV/c data set are shown in Fig. 10 and the remaining cases are shown in Figs. 32 to 34. The parameters  $\sigma_0^+$  and  $\sigma_0^-$  present only a weak phase space dependence, exhibiting values centered at 0.4, and rarely smaller than 0.35 or larger than 0.5. Concerning the parameters  $\alpha$  and  $d$ , a peculiar behavior is observed: a region of mid- $p$  and mid- $p_T$  clearly stands out from the average

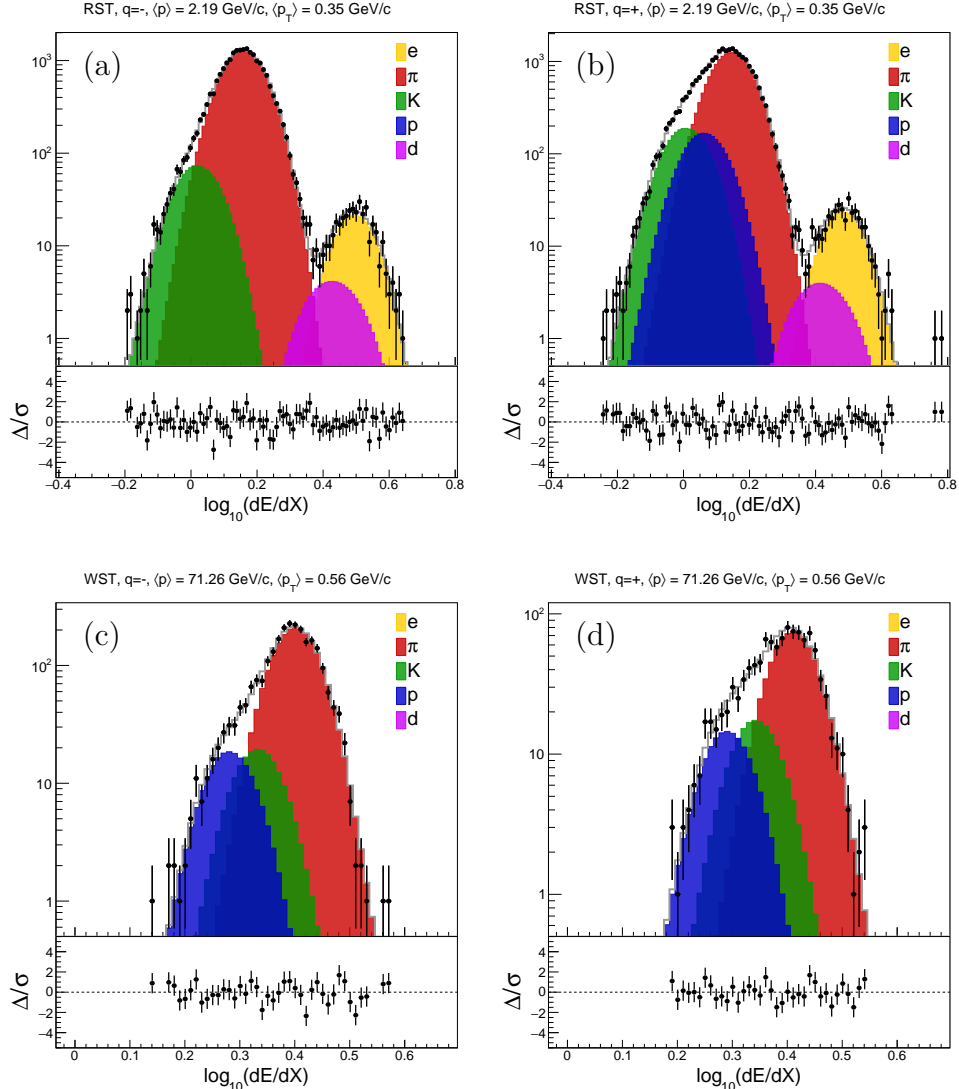


Figure 7 – Examples of the fitted  $dE/dx$  distributions from the 158  $\text{GeV}/c$  dataset. On the top, the distributions of the (a) negatively and (b) positively charged tracks are shown for one phase space bin of the RST subset. On the bottom, the distributions of the (c) negatively and (d) positively charged tracks are shown for a different phase space bin of the WST subset. The values of the  $\langle p \rangle$  and  $\langle p_T \rangle$  for each phase space bin is indicated on the top of each plot. The black dots show the observed number of tracks, while the colored distributions are the results of the  $dE/dx$  fit or each particle type. On the bottom of each plot, we show the residual of the fit, defined as the difference between the observed and the expected number of tracks from the result of the fit, divided by the uncertainty of the observed number.

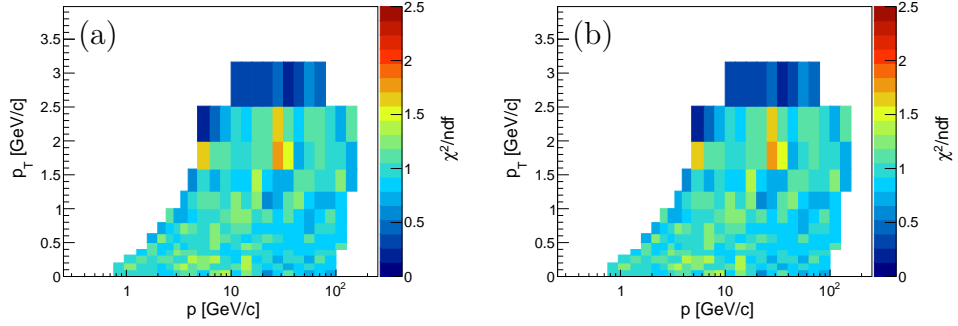


Figure 8 –  $\chi^2/\text{ndf}$  of the  $dE/dx$  fit for the 158 GeV/ $c$  data set. The RST and WST are shown in (a) and (b), respectively.

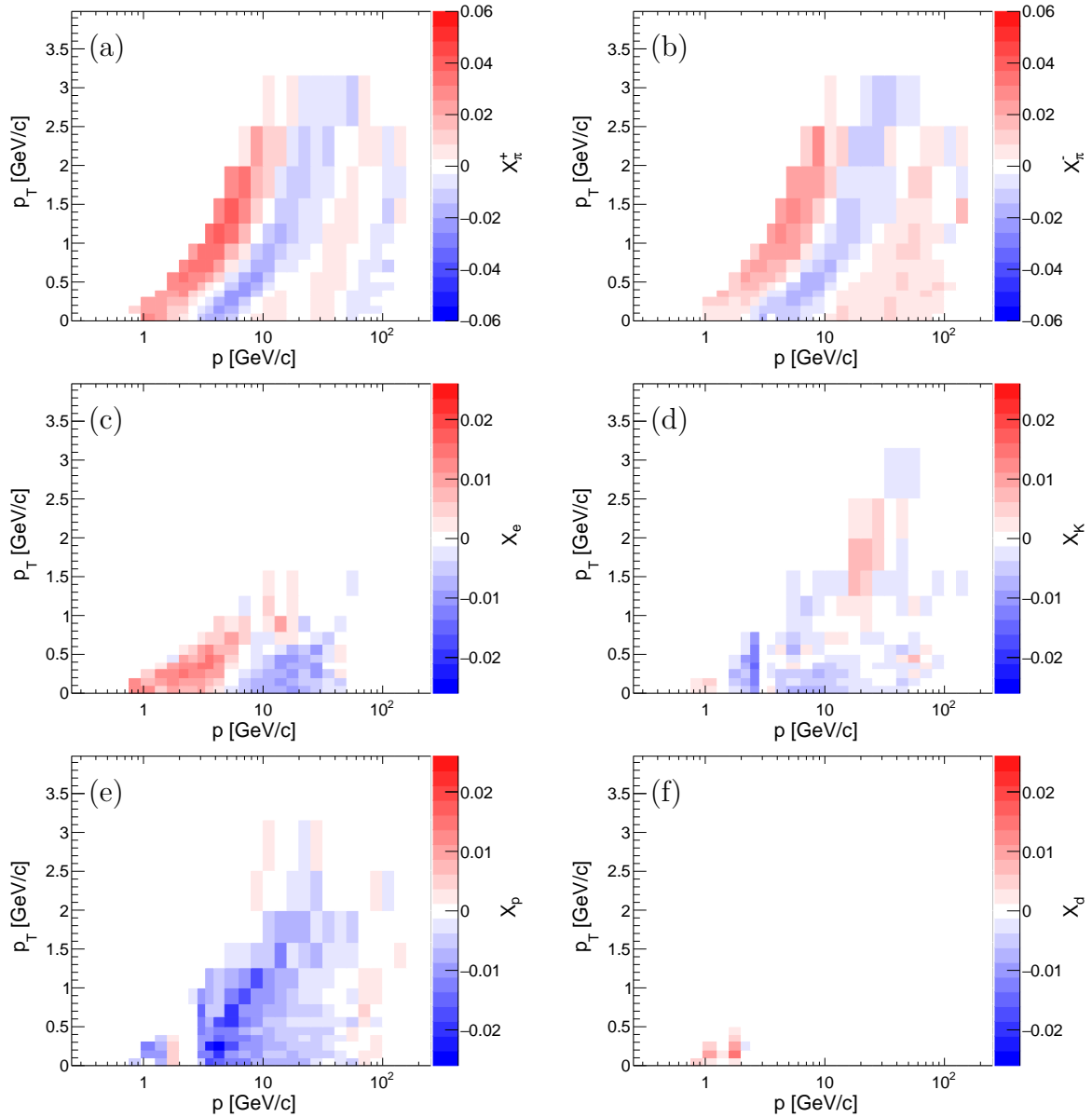


Figure 9 – Calibration constants obtained from the  $dE/dx$  fit of the RST and 158 GeV/ $c$  data set.

behavior. In this region, the asymmetry parameter  $d$  assumes negative values and the exponent  $\alpha$  assume values smaller than the average. Since the source of this behavior is not well understood, a contribution to the systematic uncertainties due to that will be estimated. For that, the  $dE/dx$  fit was repeated with the parameters  $\alpha$  and  $d$  fixed to their average values, one at a time, and the differences on the particles fractions were taken as the systematic uncertainty. See Sec. 7.8.2 for more the details.

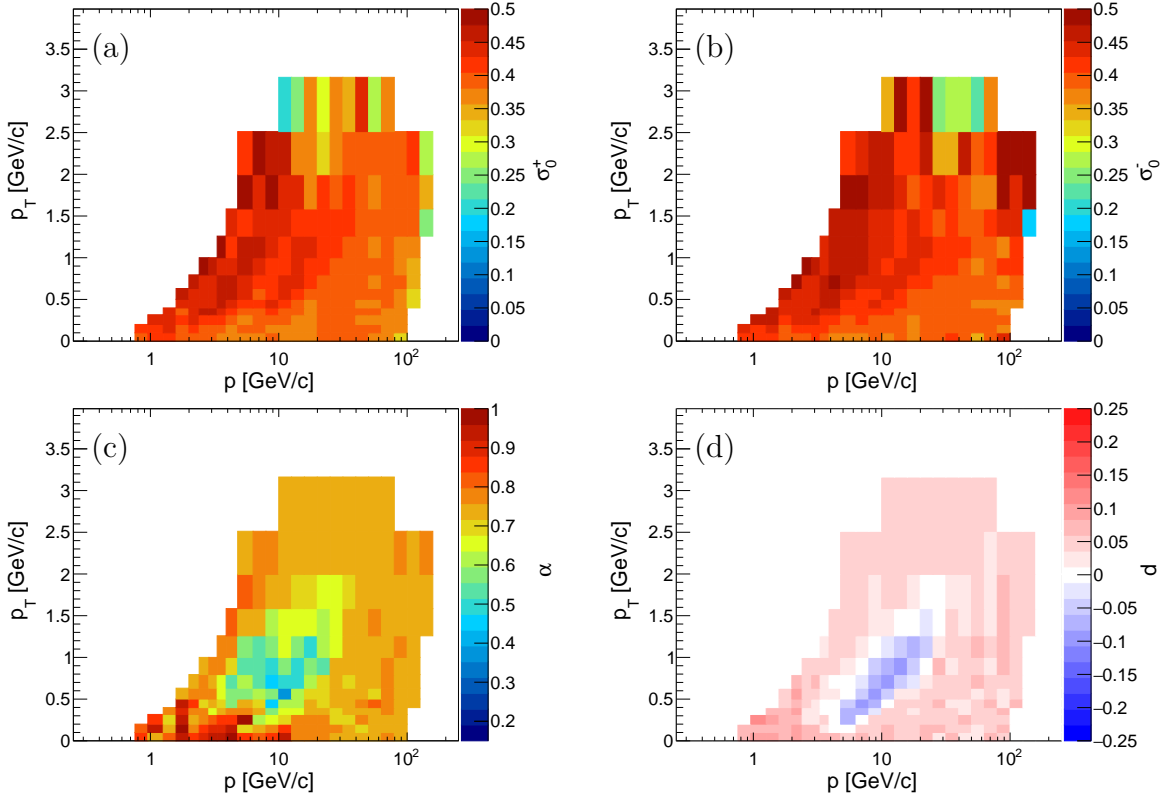


Figure 10 – Shape parameters obtained from the  $dE/dx$  fit of the RST and 158 GeV/ $c$  data set.

Examples of the particle fractions for RST and 158 GeV/ $c$  with target inserted are shown in Fig. 11 and the remaining cases are shown in Figs. 35 to 37. From the fraction of the particle types  $\pi$ , K and p, it is clear that there are few  $p$  bins, between 1 and 5 GeV/ $c$ , in which the fitted fractions stand out from the overall behavior. This happen because the overlap between the  $dE/dx$  distribution of two particle types are too large, creating a degeneracy between their fractions in the fit. Since the particle fractions of these  $p$  bins are clearly not reliable, a special strategy had to be developed to approach this problem. In the next section we describe our strategy. The fractions from the target removed dataset are shown in Sec. 7.5.7.

### 7.5.6 Simulated data ensembles, cuts and corrections

The Simulated Data Ensembles (SDEs) are large sets of simulations that reproduce the most relevant features of the data and are fitted by following exactly the same fit

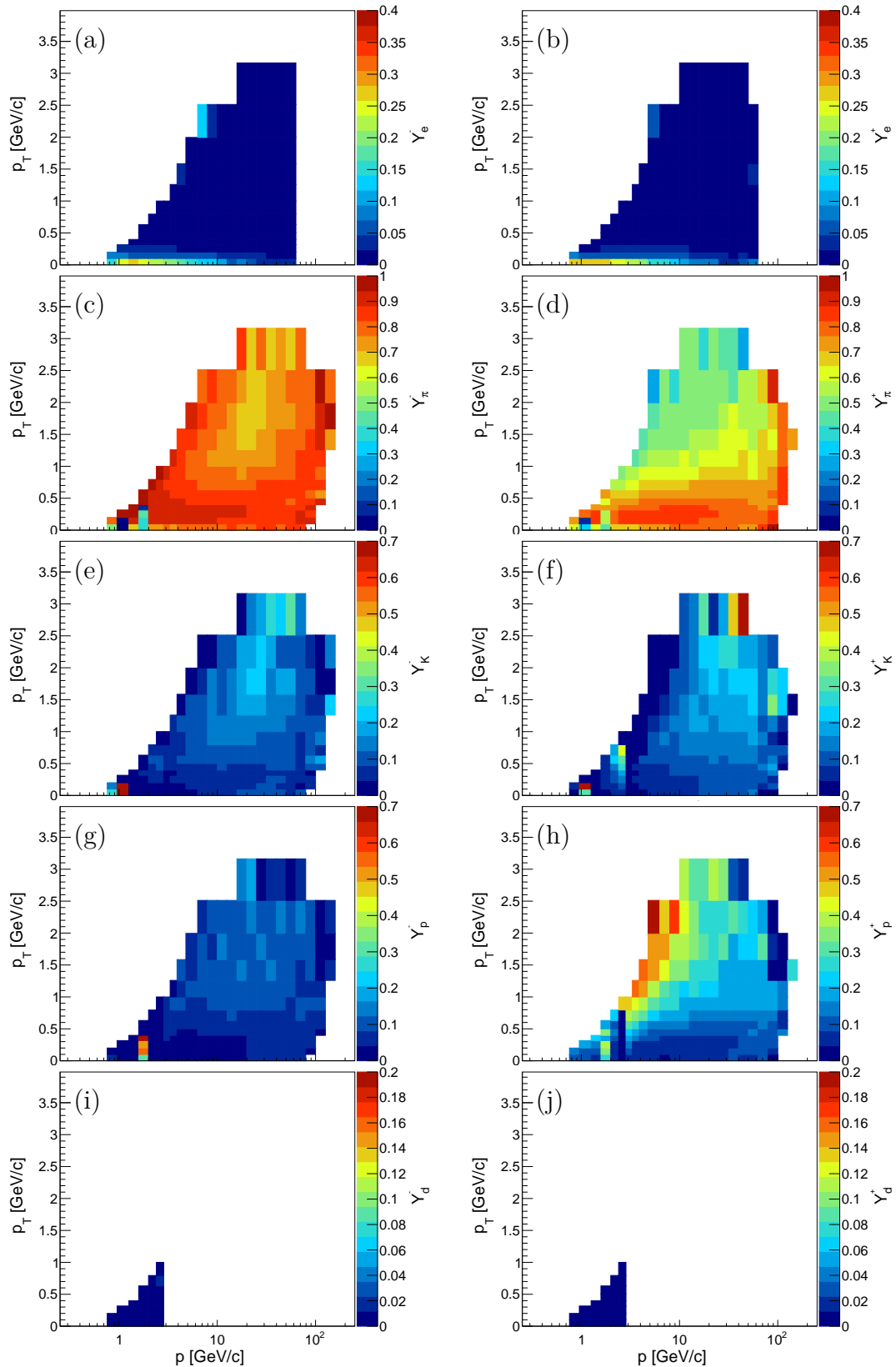


Figure 11 – Particle fractions obtained from the  $dE/dx$  fit of the RST and 158 GeV/ $c$  data set.

strategy described in Sec. 7.5.4. By analysing the fit results of the SDEs, we can evaluate the fit performance in a statistical basis and then estimate biases and statistical uncertainties of the particle fractions.

The construction of one individual simulation set of a SDE starts by creating a new simulated track for each data track reproducing its properties like  $p$ ,  $p_T$  and  $n_{\text{cl}}$ . This means that the number of tracks contained in a phase space bin, as well as their  $p$ ,  $p_T$  and  $n_{\text{cl}}$  distributions, is identical in the simulation and in the data. The second step is to associate a particle type to each simulated track. To do that we sample randomly one of the five possible types by assigning them weights that are derived from the particle fractions obtained from the  $dE/dx$  fit of the data. To avoid the statistical fluctuations on the fitted fractions, a smoothing process was performed in which a 2-dimensional forth-degree polynomial function was fitted to the fractions. The fitted function is given by

$$f(p, p_T) = \sum_{n=0}^{n<4} \sum_{m=0}^{m<4} a_{nm} (\log p)^n p_T^m, \quad (7.13)$$

where  $a_{nm}$  are free parameters to be fitted. The fit was performed by using a traditional  $\chi^2$  method. In Fig. 12 we show few examples of the  $p_T$  projections of the fractions and the fitted polynomial function.

After sampling a particle type, the  $dE/dx$  associated to each track is sampled by following the  $dE/dx$  model. The model parameters are set as the ones obtained by the  $dE/dx$  fit of the data, which are shown in Sec. 7.5.5. A set of  $\approx 1000$  simulated sets, for each beam energy, were created by following the description above and fitted afterwards. As the result, we obtain the distributions of the fitted particle fractions for each phase space bin.

From the SDEs results, we can first evaluate the relative standard deviation of the fractions, defined as  $\sigma_r = \sigma_Y / \langle Y \rangle$ , where  $\sigma_Y$  is the standard deviation of the fraction  $Y$  and  $\langle Y \rangle$  is its average value. In Fig. 13 we show one example of  $\sigma_r$  for the RST and 158 GeV/c case. The remaining cases are shown in Figs. 38 to 40. Only  $\pi^\pm$ ,  $K^\pm$  and  $p(\bar{p})$  are shown because these are the particles of interest in this analysis. Second, we can evaluate the relative bias, defined as  $\delta_r = \langle \Delta Y / Y \rangle$ , where  $\Delta Y$  is the difference between the fitted and the true fraction, being the former computed at the moment the particle types of the simulated tracks are sampled. In Fig. 14 we show examples of  $\delta_r$  for the RST and 158 GeV/c case, while the remaning cases are shown in Figs. 41 and 43 and ??.

From the  $\sigma_r$  one can clearly see that for few  $p$  bins, mainly between 1 and 10 GeV/c, the fitted fractions present a very large relative standard deviation in comparison to the remaning phase space regions. This is because of the proximity between the mean of the  $dE/dx$  distribution of two particle types that cause a partial degeneracy between their fractions. The result of the  $dE/dx$  fit at these phase space bins are evidently not suitable

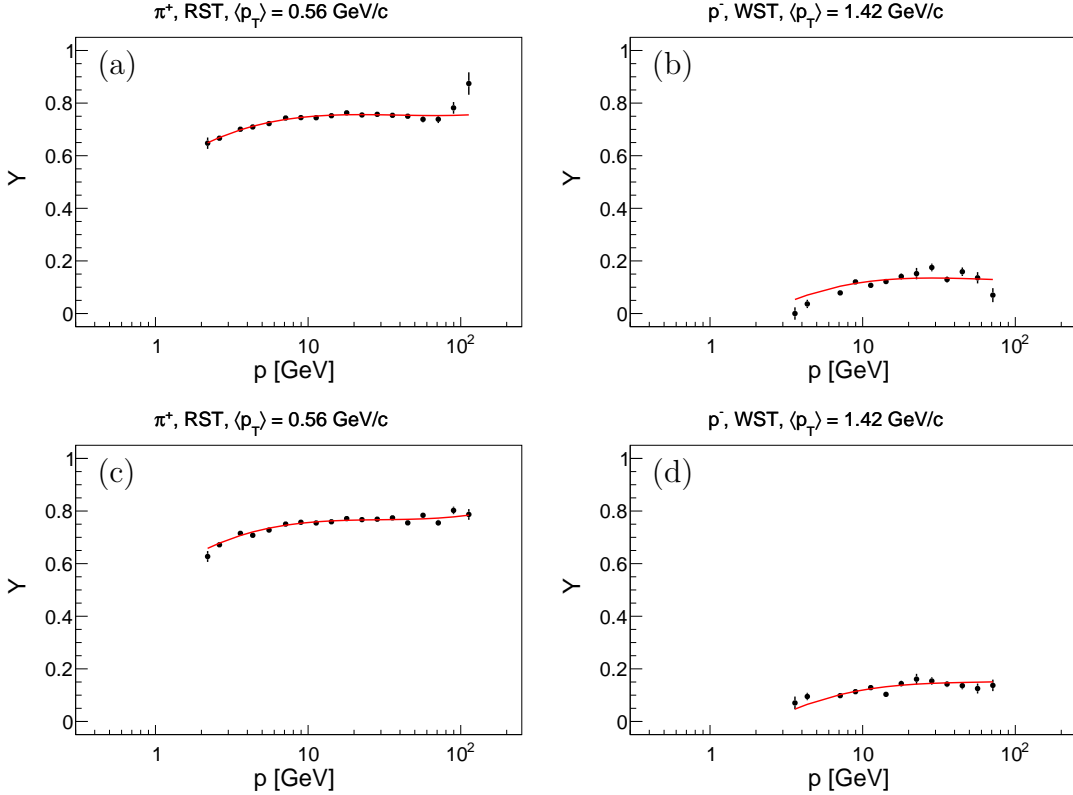


Figure 12 – Examples of the parametrization of the particle fractions to be used to create the Simulated Data Ensembles. The plots in (a) and (b) refer to the 158  $\text{GeV}/c$  data set and in (c) and (d) to the 350  $\text{GeV}/c$  one. The particle type, the RST/WST subset and the  $\langle p_T \rangle$  are indicated on the top of each plot. The black dots show the particle fractions obtained from the  $dE/dx$  fit and the red curves show the result of the fit of the Eq. (7.13) to these fractions.

and, because of that, they will be removed from our analysis. To this aim, the bins with  $\sigma_r$  larger than 0.15 for  $\pi^\pm$ , and 0.25 for  $K^\pm$  and  $p(\bar{p})$  were removed.

From the  $\delta_r$  we can observe that there are regions of the phase space which presents a significant relative bias on the fractions. These regions are mainly the low statistic and the high  $p$  bins. In the latter case, the fraction are biased because the  $dE/dx$  distributions of all particle types approach to each other following the relativistic rise behavior of the deposit energy function. Attempts were made to eliminate this bias by changing the fit strategy, however, we found no effective solution. Therefore, we have decided for a correction procedure based on the  $\delta_r$  obtained from the SDEs. A multiplicative correction factors, called  $c$ , was computed and we show it in Fig. 15 for the RST and 158  $\text{GeV}/c$  case, while the remaining cases are shown in Figs. 44 to 46. The phase space bins removed because of the large  $\sigma_r$  are shown as white bins.

Besides the cuts and corrections, the SDEs can also be used to compute the estimate the statistical uncertainties of the particle fractions. This was done by computing the standard deviation of fractions obtained from the SDEs. It is decided to use these values

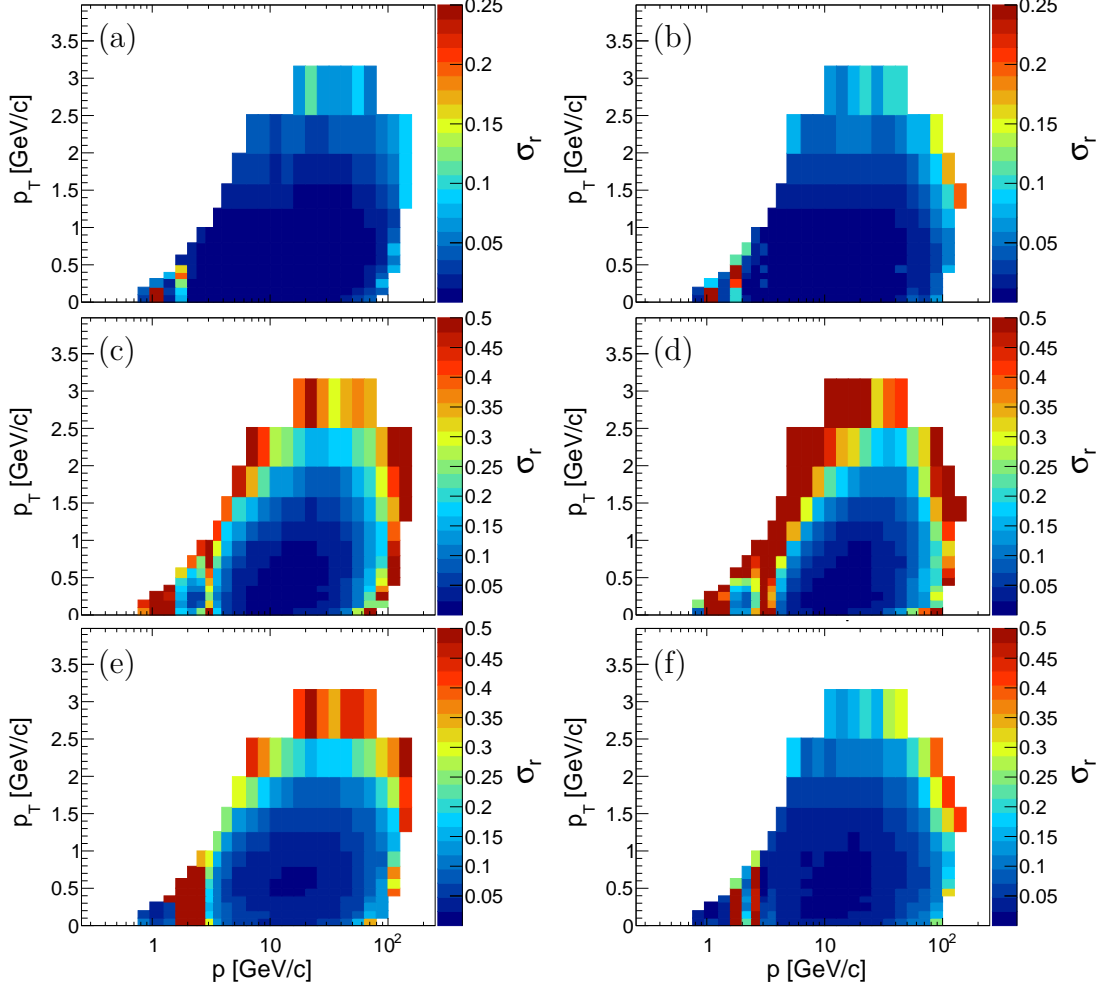


Figure 13 – Relative standard deviation ( $\sigma_r$ , see the definition in the text) of the particle fractions obtained with the SDEs for the RST and 158 GeV/ $c$  case. The  $\pi^+$  case is shown in (a),  $\pi^-$  in (b),  $K^+$  in (c),  $K^-$  in (d),  $p^+$  in (e) and  $p^-$  in (f).

of standard deviation of the final statistical uncertainties of the fractions, instead of the ones resulting from the fit procedure.

### 7.5.7 Particle identification results

After applying the cuts and corrections discussed in Sec. 7.5.6 we obtain the final particle fractions to be used to compute the spectra. In Fig. 16 we show examples of the final fractions for RST and 158 GeV/ $c$  dataset, while the remaining cases are shown in Figs. 47 to 49. Only the three particle types of interest are shown:  $\pi$ ,  $K$  and  $p$ . Each plot shows the fractions as a function of  $p$  for one  $p_T$  bin. The equivalent plots for the target removed dataset are shown in Figs. 50 to 53.

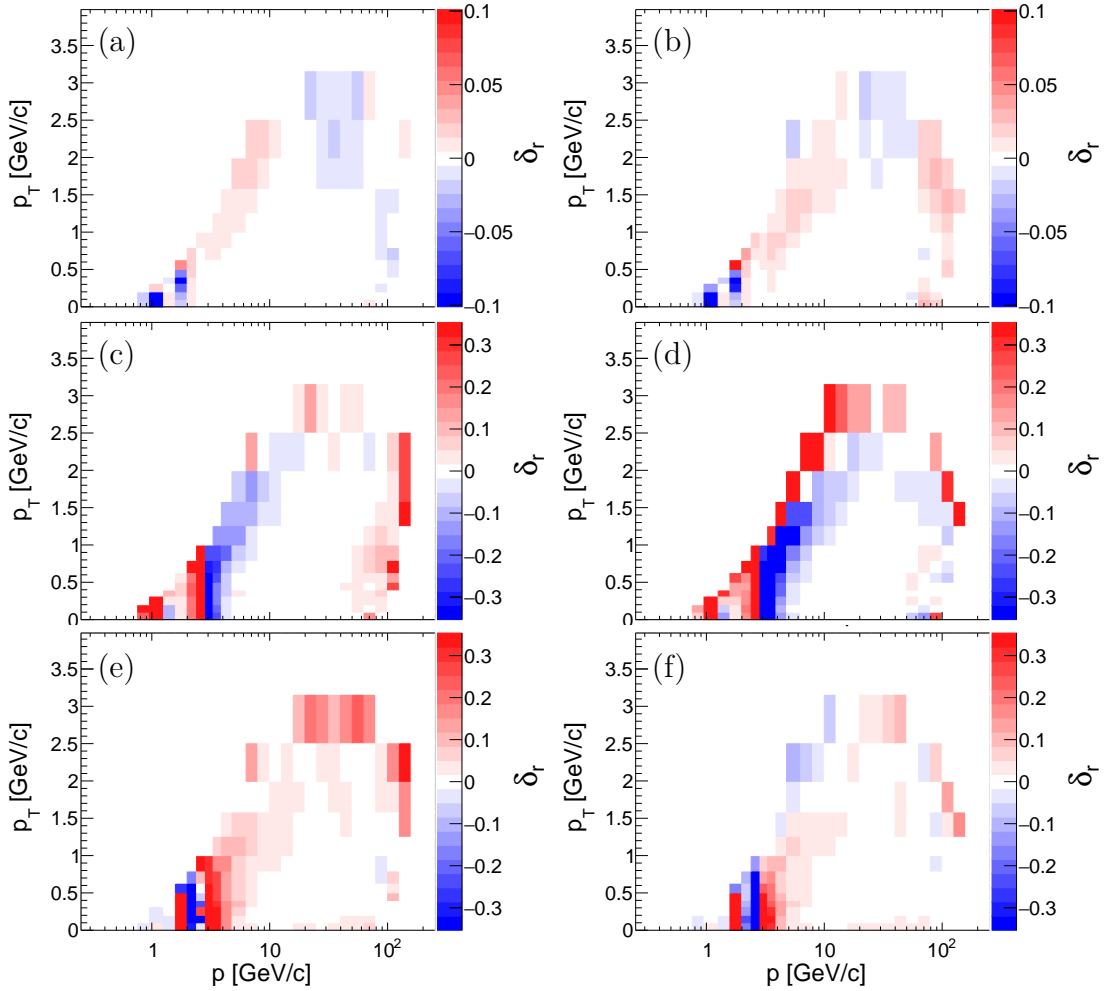


Figure 14 – Average relative bias ( $\delta_r$ , see the definition in the text) of the particle fractions obtained with the SDEs for the RST and 158 GeV/c case. The  $\pi^+$  case is shown in (a),  $\pi^-$  in (b),  $K^+$  in (c),  $K^-$  in (d),  $p^+$  in (e) and  $p^-$  in (f).

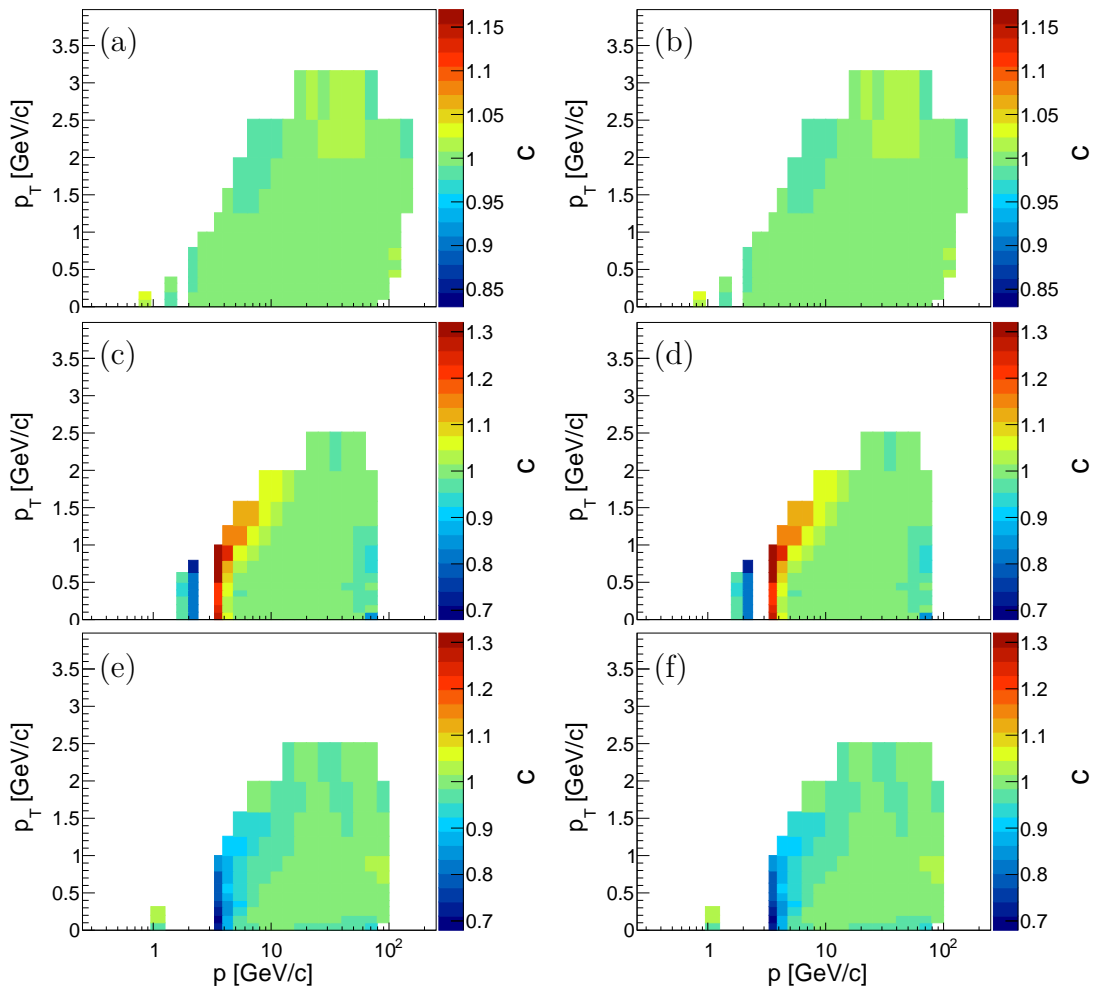


Figure 15 – Correction factors ( $c$ , see the definition in the text) for the RST and 158 GeV/c case. The  $\pi^+$  case is shown in (a),  $\pi^-$  in (b),  $K^+$  in (c),  $K^-$  in (d),  $p^+$  in (e) and  $p^-$  in (f).

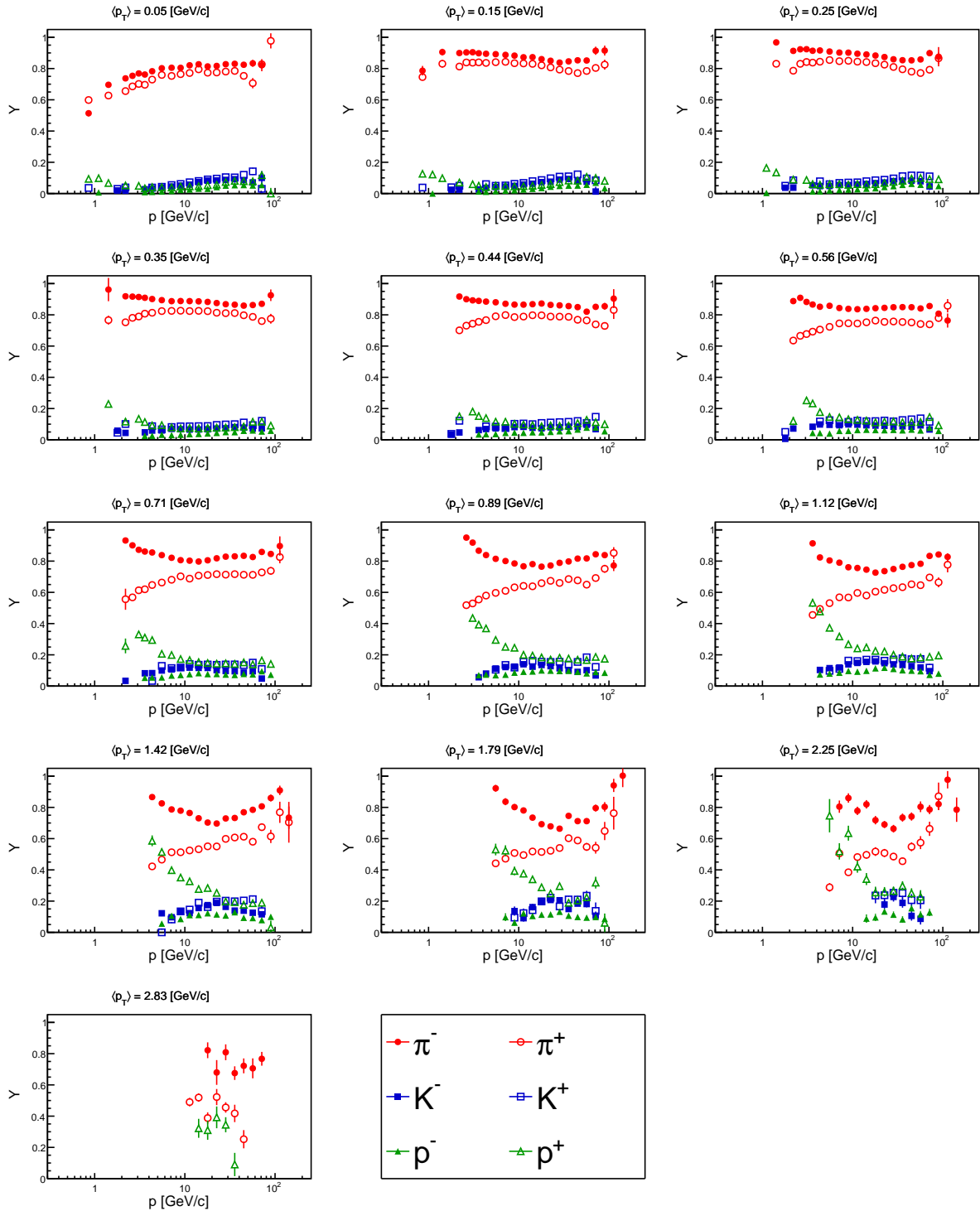


Figure 16 – Particle fractions obtained from the  $dE/dx$  fit of the RST and 158  $\text{GeV}/c$  dataset, with target inserted.

$V^0$ particle	decay products	BR
$\Lambda$	$p + \pi^-$	63.9%
$\bar{\Lambda}$	$\pi^+ + \bar{p}$	63.9%
$K_S^0$	$\pi^+ + \pi^-$	69.2%

Table 2

## 7.6 $V^0$ analysis

In this section we describe the part of our analysis focused on the  $\Lambda(\bar{\Lambda})$  and  $K_S^0$  particles. Neutral weakly decaying particles with average decay length ( $c\tau$ ) of order of few or tens of centimeters can be detected by NA61/SHINE experiment through their charged decay products. This kind of particles are called  $V^0$  particles because of the shape of the decay ( $V$ ) and its neutral charge ( $^0$ ). Although the  $V^0$  particle itself does not create a track in the TPCs, the products of its decay do, allowing us to reconstruct the position of the decay vertex and, by using the properties of the daughter tracks, identify the original  $V^0$ . Therefore, the detector acceptance depends strongly on geometrical factors because both daughter particles must create tracks on the TPCs and they must be well reconstructed. In Tab. 2 we list the three  $V^0$  particles of interest of the present work together with the properties of their decay channel which is used here (daughter particles and branching ratio).

The description of the standard algorithms applied by NA61/SHINE experiment to find and reconstruct the  $V^0$ 's can be found in Refs. [28, 29], while the particular  $V^0$  selection applied to our analysis was described in ???. The identification of the  $V^0$  particles is done by means of its invariant mass, which is given by

$$m_{\text{inv}} = \sqrt{m_+^2 + m_-^2 + 2(E_+E_- - \vec{p}_+\vec{p}_-)}, \quad (7.14)$$

where the indexes + and – refer to the positively and negatively charged daughter particles. Because of the large combinatorial background, which means that many tracks can be randomly combined and reconstructed as  $V^0$  particles, a signal extraction step is needed. This is usually done by fitting the measured invariant mass distribution with a signal and a background model. The signal extraction procedure is presented in Sec. 7.6.2 and its results are shown in Sec. 7.6.4.

### 7.6.1 $V^0$ selection

#### (TO REVIEW)

The  $V^0$  selection criteria used for the  $V^0$  analysis is the following:

- (i) The selected vertex must be identified as a  $V^0$  type vertex.

- (ii) The number of daughter tracks of the vertex must be equal to 2.
- (iii) Both daughter tracks must be of opposite charges.
- (iv) The total number of cluster has to be greater than 30 for both tracks
- (v) At least one track has to have more than 15 clusters in the VTPCs

These selection criteria are standard ones in NA61/SHINE analysis. Further cuts on the  $V^0$ 's will be applied at the signal extraction step (see Sec. 7.6.3).

Since it is not possible to define the detector acceptance for the  $V^0$ 's analogously to what is done for the tracks, the possible discrepancies between data and simulations on the borders of the acceptance will be accounted on the systematic uncertainties (see Sec. 7.8.2). Because these tracks on the borders have small number of clusters, the systematic uncertainty will be estimated by changing the minimum number of clusters on both tracks from 30 to 20.

### 7.6.2 Signal extraction strategy

The signal extraction is done by fitting the  $m_{\text{inv}}$  distribution with a model that includes the signal and the background contributions. Traditionally in NA61/SHINE analyzes the signal is modelled by analytical functions like Breit-Wigner or Gaussian functions [30, 31]. However, because of difficulties in describing the  $K_S^0$  signal, we have decided to use here Monte Carlo templates instead. More than that, it was found that for few  $K_S^0$  phase space bins, the signal description is very poor with only one single template and therefore a double template approach was preferred. The simulations used to build the templates were described in Sec. 7.2 and they include most of the expected detector effects. It was observed that the choice of the hadronic interaction model has an insignificant impact on the shape of the templates. For the background description we have decided for the standard approach, using generic polynomial functions.

The fit is performed by a likelihood method assuming Poissonian distributions for the entries of the  $m_{\text{inv}}$  distribution. The log-likelihood to be maximized is analogous to the one shown in Eq. (7.6), however the notation is simpler because the only index is the one that refers to the  $m_{\text{inv}}$  bin. This index will be represented by  $i$ , the total number of  $m_{\text{inv}}$  bin by  $I$  and the value of  $m_{\text{inv}}$  in the center of the bin by  $m_i$ . Also, the expected value of the particle mass is represented by  $m_0$ . Thus, being  $n$  and  $\nu$  the observed and expected number, respectively, the log-likelihood function is given by

$$l_0 = 2 \ln L = 2 \sum_{i=1}^I (\nu_i - n_i \ln \nu_i). \quad (7.15)$$

The expected number  $\nu_i$  is given by the sum of the signal and background contribution as

$$\nu_i = T_i + f_i^{\text{BG}}, \quad (7.16)$$

where  $T_i$  comes from the templates and

$$f_i^{\text{BG}} = p_0 + p_1(m_i - m_0) + p_2(m_i - m_0)^2. \quad (7.17)$$

The contribution of one template evaluated at a given mass  $m$  is represented by  $t[m]$ . The templates contain the same number of bins  $I$  and  $t[m]$  is computed by a linear interpolation of the two bins in which their centers are the closest to  $m$ . To allow the templates to shift, we added the shift parameters  $\delta m$ 's. In the end, the template term  $T_i$  computed by

$$T_i = S_{\text{fit}} (\alpha t^0[m_i + \Delta m^0] + (1 - \alpha)t^1[m_i + \Delta m^1]), \quad (7.18)$$

where  $S_{\text{fit}}$ ,  $\alpha$ ,  $\Delta m^0$  and  $\Delta m^1$  are free parameters to be fitted. Since the templates are normalized,  $S_{\text{fit}}$  gives directly the amount of signal in the distribution.

By combining the Eqs. (7.16) to (7.18) with Eq. (7.15) we have the log-likelihood function  $l_0$  with 7 free parameters, being  $p_0$ ,  $p_1$  and  $p_2$  for the background and  $S_{\text{fit}}$ ,  $\alpha$ ,  $\Delta m^0$  and  $\Delta m^1$  for the signal.

Similarly to what was done for the  $dE/dx$  fit, here we also include Gaussian constraints to make the fit more stable. The parameters to be constrained are the mass shifts,  $\Delta m^0$  and  $\Delta m^1$ , and the fraction  $\alpha$ . In the former case the intention is to avoid solutions of the fit in which the template shifts are too large. It is expected shifts of order of few MeV/c only and it was observed that without the constraints there could be solutions with larger shift than this, which is physically meaningless. The constraint on the  $\alpha$  parameter is important for cases in which the signal is well described by one template only and consequently  $\alpha$  becomes degenerated. The constraint term is given by

$$c = \left( \frac{\Delta m^0}{0.001} \right)^2 + \left( \frac{\Delta m^1}{0.003} \right)^2 + \left( \frac{\alpha}{0.2} \right)^2, \quad (7.19)$$

where the  $\Delta m^0$  and  $\Delta m^1$  is given in GeV/c units. Finally, the final log-likelihood to be maximized is given by

$$l = l_0 + c, \quad (7.20)$$

where  $l_0$  and  $c$  are given by Eq. (7.20) and Eq. (7.19), respectively.

The maximization of  $l$  was done by means of the MINUIT package [27]. The width of the  $m_{\text{inv}}$  bins was 1.5 and 3.0 MeV/c<sup>2</sup> for  $\Lambda(\bar{\Lambda})$  and  $K_S^0$ , respectively, and the mass range was [1.095GeV/c<sup>2</sup>, 1.160GeV/c<sup>2</sup>] and [0.42GeV/c<sup>2</sup>, 0.580GeV/c<sup>2</sup>] again for  $\Lambda(\bar{\Lambda})$  and  $K_S^0$ , respectively. For each beam energy dataset, the templates were filled with the three simulation sets, generated by different hadronic interaction models.

As results of the fit, we obtain the estimated signal  $S_{\text{fit}}$ , and the average background  $B_{\text{fit}}$ , which is the integral of the background function over all the mass range of the fit. To avoid possible bias due to misdescription of the signal by the templates, the final signal is

not taken as  $S_{\text{fit}}$ . Instead, we compute it as  $S = N - B_{\text{fit}}$ , where  $N$  is the total number of entries in the measured  $m_{\text{inv}}$  distribution. We assume by doing this that the background estimation is more precise than the signal one. The statistical uncertainty on  $S$  is given by  $\sigma_S = \sqrt{N + \sigma_{B_{\text{fit}}}^2}$ , where Poissonian fluctuations are assumed for  $N$  and  $\sigma_{B_{\text{fit}}}$  is obtained as a result of the fit.

To determine suitable starting parameters for the fit, a preliminary phase is performed by means of a  $\chi^2$  fit. In this case, the signal model is simplified and only one template is used without allowing it to shift. In this way the whole model turns to be linear on the fitting parameters and the  $\chi^2$  minimization can be done analytically. The results of the  $\chi^2$  fit is then used to compute the respective parameters to start the final fit.

Because the number of selected  $V^0$ 's is substantially smaller at the target removed dataset, a special strategy for the signal extraction is required. First, the phase space binning was changed so all the original  $p_T$  bins are merged in one unique bin for each  $p$  bin. Second, the  $m_{\text{inv}}$  fit is performed by means of an analytic minimization of the  $\chi^2$  in which only one template is considered, without allowing its position to shift. Although it is known that this fitting procedure can produce biased results, it is acceptable in this context because the statistical uncertainties due to the low statistics is surely much larger than the bias. After obtaining  $S$  from the  $m_{\text{inv}}$  fit, the target removed signal for each original  $p$  and  $p_T$  bin is obtained by assuming the same  $p_T$  dependence observed in the target inserted dataset.

### 7.6.3 $V^0$ cuts

The  $V^0$  cuts are applied to the  $m_{\text{inv}}$  data to reduce the relative amount of background events, which increases the precision of the signal extraction. Two quantities are used here for the  $V^0$  cuts, the radial impact parameter of the  $V^0$  particle ( $b_r$ ) and its decay distance ( $L_{\text{decay}}$ ). The  $b_r$  is defined as  $b_r = \sqrt{(0.5b_x)^2 + b_y^2}$ , where  $b_x$  and  $b_y$  are the coordinates  $x$  and  $y$  of the projection of  $V^0$  particle trajectory at the target plane. The factor 0.5 on  $b_x$  is included because the spread of  $b_x$  is approximately 2 times larger than  $b_y$ . In Fig. 17 we show the  $b_r$  distribution for signal and background obtained from simulations for all the phase space bins. We can observe that the  $b_r$  parameter of signal  $V^0$ 's are more concentrated at small values while the background ones show a longer tail. Because of that, only  $V^0$ 's with  $b_r$  small than a certain value were used for the signal extraction. This value was chosen to be 2 cm. The efficiency of this cut was observed to be larger than 90% for all the phase space bins.

The  $L_{\text{decay}}$  is defined as the distance between the position of the  $V^0$  and the position of the main vertex. The background  $V^0$ 's tend to have smaller  $L_{\text{decay}}$  than the signal ones, so  $V^0$  with  $L_{\text{decay}}$  smaller than a given cut value  $L_{\text{decay}}^{\text{cut}}$  are removed. Because of the physical dependence of the  $L_{\text{decay}}$  with the momentum of the particle,  $L_{\text{decay}}^{\text{cut}}$  was assumed to depend

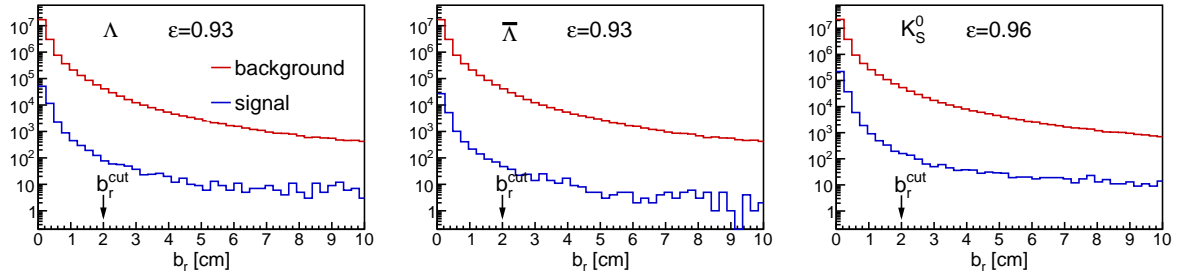


Figure 17

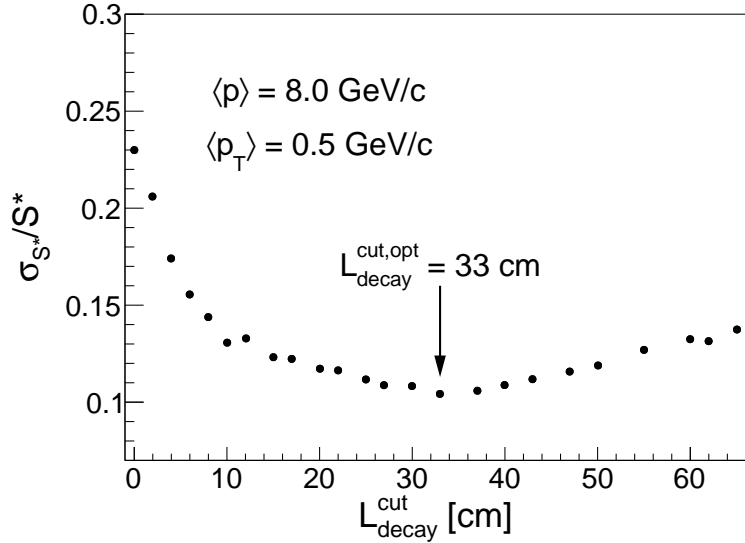


Figure 18

on the  $V^0$  momentum and it was optimized to minimize the statistical uncertainty of the extracted signal. The optimization was done by first performing the  $m_{\text{inv}}$  fit with many values of  $L_{\text{decay}}^{\text{cut}}$  and then evaluating  $S^* = S/\varepsilon$  and its uncertainty  $\sigma_{S^*}$ , where  $\varepsilon$  is the efficiency due to the  $V^0$  cuts. Next we found value of  $L_{\text{decay}}^{\text{cut}}$  that minimizes the relative uncertainty  $\sigma_{S^*}/S^*$ , which is denoted by  $L_{\text{decay}}^{\text{cut},\text{opt}}$ . One example of  $\sigma_{S^*}/S^*$  as a function of  $L_{\text{decay}}^{\text{cut}}$  is shown in Fig. 18, where  $L_{\text{decay}}^{\text{cut},\text{opt}}$  is indicated. The  $L_{\text{decay}}^{\text{cut},\text{opt}}$  found for all the phase space bins are shown in Figs. 19 and 54 as a function of the  $V^0$  momentum where the average over the  $p_T$  bins are shown as red markers. A fit of a linear function of  $\log p$  to the average  $L_{\text{decay}}^{\text{cut},\text{opt}}$  is shown as a red curve. Since this function shows to describe in first order the momentum dependence of  $L_{\text{decay}}^{\text{cut},\text{opt}}$ , we have decided to use it to define the  $L_{\text{decay}}^{\text{cut}}$ .

The signal extraction described in Sec. 7.6.2 was performed using the  $m_{\text{inv}}$  distributions obtained after applying both  $V^0$  cuts described above. The lost of signal  $V^0$ 's due to these cuts were corrected at the Monte Carlo correction step, described in Sec. 7.7.

#### 7.6.4 Signal extraction results

(TO REVIEW)

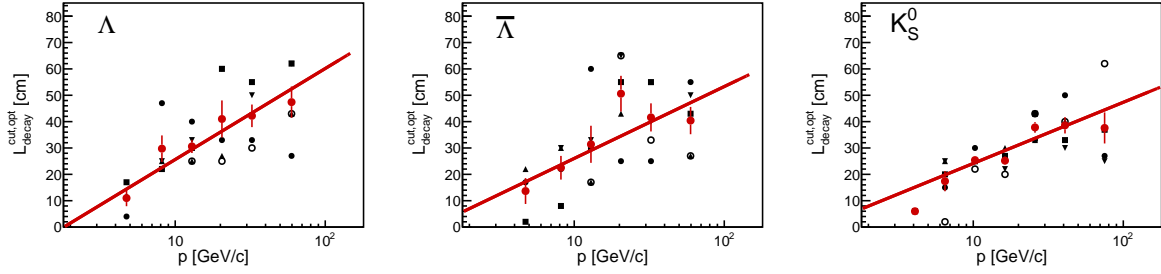


Figure 19 – Optimization of the  $L_{\text{decay}}^{\text{cut}}$  for the 158 GeV/ $c$  dataset. The plot on left, middle and right shows  $\Lambda$ ,  $\bar{\Lambda}$  and  $K_S^0$ , respectively.

In Figs. 20 and 58 we show examples of the fitted  $m_{\text{inv}}$  distributions for the target inserted dataset and in Figs. 21 and 59 for the target removed one.

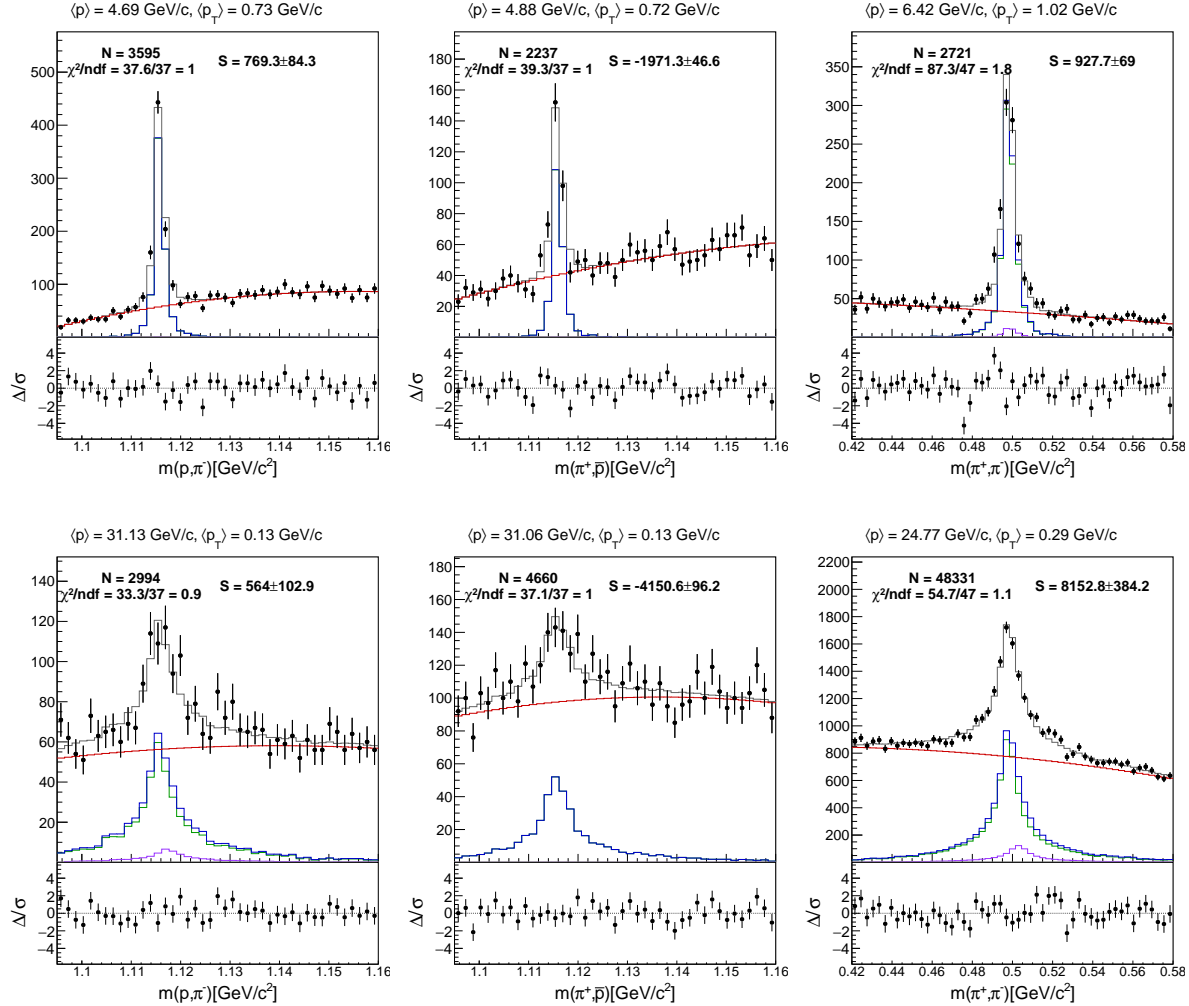


Figure 20 – Examples of the fitted  $m_{\text{inv}}$  distributions for the 158 GeV/ $c$  dataset. The plot on left, middle and right shows  $\Lambda$ ,  $\bar{\Lambda}$  and  $K_S^0$ , respectively.

The reduced  $\chi^2$  of the  $m_{\text{inv}}$  fit of the target inserted datasets are shown in Figs. 22 and 55. Since the values of  $\chi^2/\text{ndf}$  are in all phase space bins around 1 and very few bins show  $\chi^2/\text{ndf} \sim 1.5$ , we can conclude that the measured  $m_{\text{inv}}$  fit is well described by our

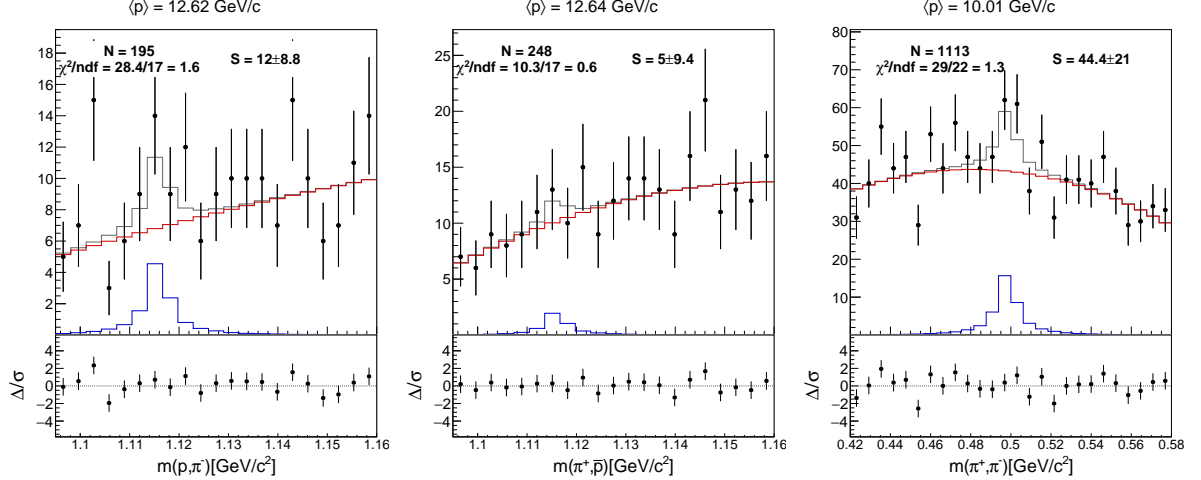


Figure 21 – Examples of the fitted  $m_{\text{inv}}$  distributions for the 158  $\text{GeV}/c$  dataset, with target removed. The plot on left, middle and right shows  $\Lambda$ ,  $\bar{\Lambda}$  and  $K_S^0$ , respectively.

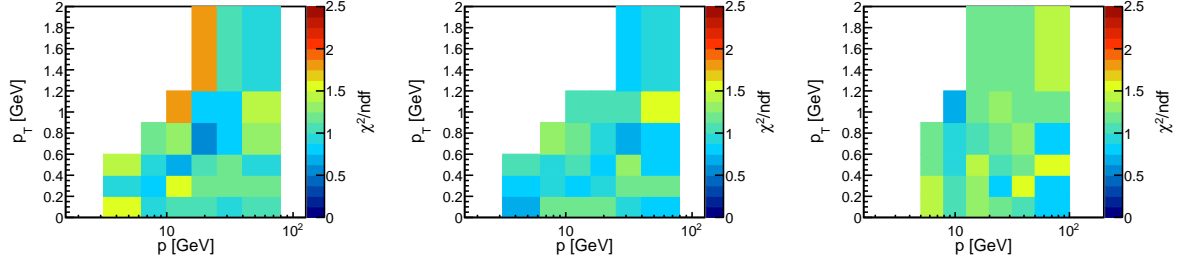


Figure 22

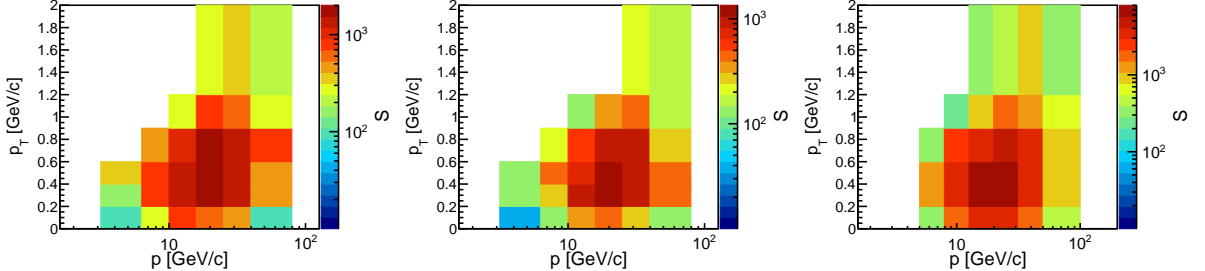


Figure 23

$m_{\text{inv}}$  model. The extracted signal  $S$  for the target inserted and removed datasets are shown in Figs. 23, 24, 56 and 57.

## 7.7 Monte Carlo corrections

### (TO REVIEW)

The measured number of events, tracks and  $V^0$ 's particles in a given phase space bin are naturally biased by detector effects. To determine the final spectra, these effects must be corrected, and that is done by applying a correction factor obtained from Monte Carlo simulations. This factor is called here  $C_{\text{MC}}$ . For a given phase space bin,  $C_{\text{MC}}$  is

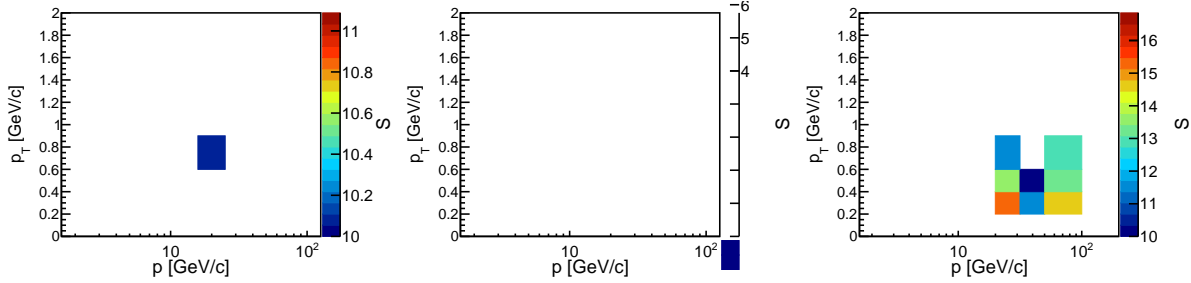


Figure 24

basically the ratio between the generated and measured spectra and it is written as

$$C_{\text{MC}} = \left( \frac{n^{\text{gen}}}{N^{\text{gen}}} \right) / \left( \frac{n^{\text{sel}}}{N^{\text{sel}}} \right). \quad (7.21)$$

where  $N$  refers to number of events and  $n$  can be either the number of tracks, for the identified spectra analysis, or the number of  $V^0$ 's, for the  $V^0$  analysis. The indexes gen and sel refer to generated and selected quantities and, while the first is obtained directly from the Monte Carlo generators, the second is obtained by the detector simulations, in which the reconstruction algorithm and selection are exactly the same as the one applied to data. For the sake of clearness, the  $C_{\text{MC}}$  can be split in the event and track or  $V^0$  contributions, which will be referred as  $\alpha$  and  $\beta$ . In this way,  $C_{\text{MC}}$  becomes

$$C_{\text{MC}} = \left( \frac{N^{\text{sel}}}{N^{\text{gen}}} \right) / \left( \frac{n^{\text{sel}}}{n^{\text{gen}}} \right) = \alpha/\beta. \quad (7.22)$$

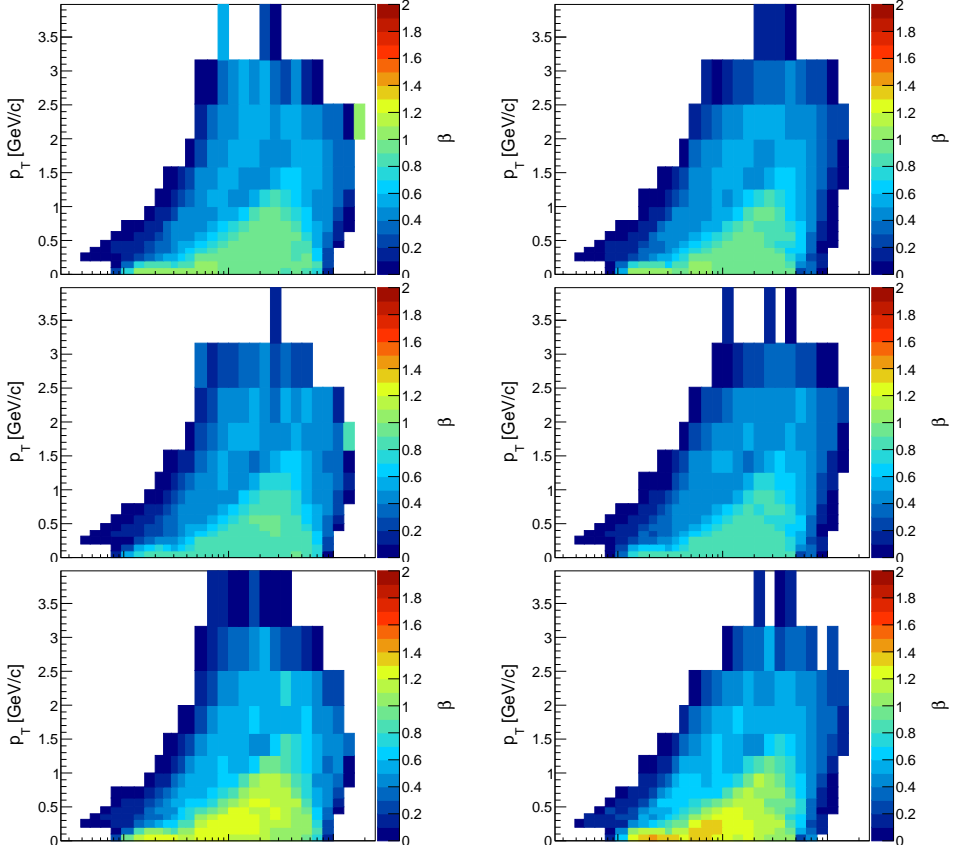
The  $\alpha$  factor is common to all the datasets, while the  $\beta$  is different for each phase space bin.

The  $C_{\text{MC}}$  was determined here by the three simulation sets, generated with different hadronic interaction models (see Sec. 7.2). The  $\alpha$  factor obtained is summarized in Tab. 3, where we show the values for each simulation set and their average value, which will be used in this work. The observed differences in the  $\alpha$  factor due to the hadronic interaction models are expected mainly because of the large discrepancy between the particle multiplicities. As an illustration, we can take the DPMJET 3.06 case, in which the average multiplicity is fairly larger than the others and consequently the  $\alpha$  is also significantly larger. This relation is caused mainly by two effects. First, the interaction trigger probability is larger on average because the larger number of particles crossing the detector. Second, the cut on the Z position of the main vertex tends to remove less events since, with more detected particles, the fit of main vertex tends to be more precise. The model dependence of the  $\alpha$  will be accounted on the systematic uncertainties in Sec. 7.8.2.

The  $\beta$  factor for  $\pi^\pm$ ,  $K^\pm$  and  $p(\bar{p})$  is computed by the ratio of the generated and measured number of tracks. In Figs. 25 and 60 we show the  $\beta$  for these particles. For the  $V^0$  particles,  $\Lambda(\bar{\Lambda})$  and  $K_S^0$ , the  $\beta$  is computed as the ratio between the  $V^0$  particles

	158 GeV/c	350 GeV/c
EPOS 1.99	0.875	0.744
DPMJET 3.06	0.949	0.848
QGSJET II-04	0.868	0.721
Average	0.897	0.771

Table 3

Figure 25 –  $\beta$  correction factor for the 158 GeV/c dataset.

generated and measured in a given phase space bin. In Figs. 26 and 61 we show the  $\beta$  for these particles. It is important to note that the  $\beta$  factor for the  $V^0$  particle includes the effect of the  $V^0$  cuts, presented in ??.

The geometrical acceptance of the detector is the dominant contribution to the  $\beta$  factor for both charged hadrons and  $V^0$  particles. Smaller effects, but still significant, are related to the event selection, track and  $V^0$  reconstruction efficiency, bin migration and feed-down from re-interactions and weak decays. The model dependence of the  $\beta$  factor is only significant ( $> 1\%$ ) for the contributions of the event selection and feed-down from weak decays. The latter case will be approached in Sec. 7.7.1. For the event selection, the differences between the three models can reach up 10% for some phase space bins, in which the contribution of both the T2 selection and the cut on the main vertex Z position are accounted for. The differences will be taken into account on the systematic uncertainties

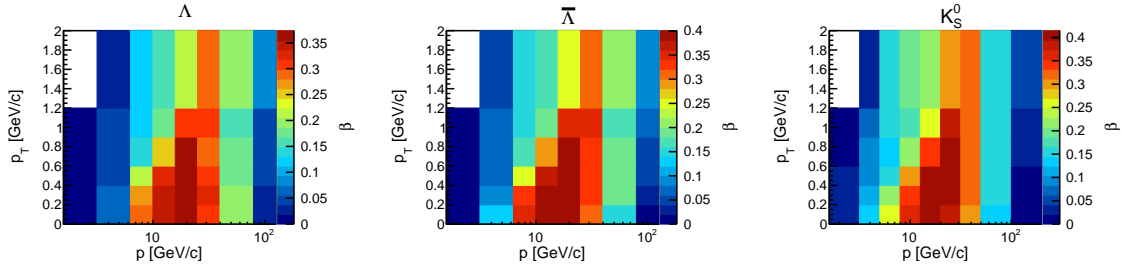


Figure 26 –  $\beta$  correction factor for the 158 GeV/ $c$  dataset.

of the spectra (see Sec. 7.8.2).

### 7.7.1 Feed-down from weak decays

#### (TO REVIEW)

For the charged hadrons, the contribution of weak decays is null for the  $K^\pm$  and can reach up to 20% for  $\pi^\pm$  and  $p(\bar{p})$ . Depending on the hadronic interaction model, the decay of  $K_S^0$  can represent from 70 to 90% of the feed-down contribution of  $\pi^\pm$ , while the decay of  $\Lambda(\bar{\Lambda})$  account for 5-10%. In the case of  $p(\bar{p})$ , from 75 to 100% is due to the decay of  $\Lambda(\bar{\Lambda})$ . Since the  $\Lambda(\bar{\Lambda})$  and  $K_S^0$  production is very different among the hadronic interaction models, the model dependence on the  $\beta$  correction for  $\pi^\pm$  and  $p(\bar{p})$  would naturally be very large, implying also in large systematic uncertainties. To avoid that, in this work the measured spectra of  $\Lambda(\bar{\Lambda})$  and  $K_S^0$  will be used to correct the feed-down contribution from these particles.

The procedure adopted for that is based on a re-weighting of the simulated particles which are produced from the decay of  $\Lambda(\bar{\Lambda})$  and  $K_S^0$ . The weight given for each model is determined by the ratio between the measured and the generated spectra of these particles by this model. To also account for  $\Lambda(\bar{\Lambda})$  and  $K_S^0$  which were produced by the decay of other weakly decaying particles, the ratio is computed by using the uncorrected spectra, which means basically the number of particles in a certain bin divided by the number of events. In ?? we show one example of the ratio for the model EPOS 1.99. A parametrization of the ratio as a function of  $p$  and  $p_T$  was performed by using a log-normal function of  $p$  in which its parameters are interpolated as a function of  $p_T$  by a second-degree polynomial function. The result of the parametrization is also shown in ??.

#### (figure here - ratio)

The weight given for the simulated particles is then computed by the parametrization of the ratio between measured and generated spectra. The small model differences due to the contribution from particles which are not  $\Lambda(\bar{\Lambda})$  or  $K_S^0$  were accounted for on the systematic uncertainties (see Sec. 7.8.2).

Concerning the feed-down from weak decays on the  $V^0$  particle spectra, the effect

is null for  $K_S^0$  and can reach up to 25% for  $\Lambda(\bar{\Lambda})$ , in which the decaying are mostly  $\Xi^\pm$ ,  $\Xi^0$ ,  $\Sigma^0$  and their anti-particles. The model dependences are also significant in this case and it will be account for on the systematic uncertainties of the spectra (see Sec. 7.8.2).

## 7.8 Spectra

### (finish it)

The final double-differential spectra for each phase space bin is computed as

$$\frac{d^2n}{dp dp_T} = \frac{1}{\Delta p \Delta p_T} C_{MC} \frac{n^I - B n^R}{N^I - B N^R}, \quad (7.23)$$

where:

- $\Delta p$  and  $\Delta p_T$  are the widths of the phase space bin;
- $C_{MC}$  is the Monte Carlo correction factor (see Sec. 7.7);
- The indexes  $I$  and  $R$  refer to target inserted and removed datasets, respectively;
- $N$  represents number of events;
- For the charged hadrons ( $\pi^\pm$ ,  $K^\pm$  and  $p(\bar{p})$ ) the  $n$  is given by the particle fraction obtained at the  $dE/dx$  fit multiplied by the total number of tracks in the phase space bin. For the  $V^0$  particles,  $n$  is the signal obtained from signal extraction procedure;
- $B$  is the target removed factor and it is meant to normalize both dataset to the same number of beam particles, and in this work it was computed by the fraction of interaction trigger events between the target inserted and removed datasets. The values of  $B$  are 5.1 and 5.2 for the 158 and 350 GeV/c datasets, respectively. This procedure to subtract the target removed contribution follow the standard approach of NA61/SHINE analysis. More details can be found in Ref. [21].

### (combination of RST and WST)

In the next sections we describe the statistical and systematic uncertainties on the spectra.

#### 7.8.1 Statistical uncertainties

The dominant contribution to the statistical uncertainties of the spectra is the uncertainty on the particle identification step for the charged hadrons and on the signal extraction step for the  $V^0$  particles. Since the number of target removed tracks is substantially smaller than the target inserted ones, the statistical uncertainties on  $n^R$  was neglected. The contribution of the  $C_{MC}$ , due to the limited number of simulated events, is taken into account, however it is relatively very small.

### 7.8.2 Systematic uncertainties

#### (dedx fit systematics)

The sources of systematic uncertainties will be listed separately for charged hadrons and  $V^0$  analysis. First, the list of systematic uncertainties accounted for in spectra of the charged hadrons are:

- $dE/dx$  fit
- The model dependence on the Monte Carlo correction factors due to the T2 event selection. Since both the number of events and tracks are affected by this selection, the model differences were estimated by combining both  $\alpha$  and  $\beta$  factors. To compute the systematic uncertainties, we first isolated the contributions of the T2 selection on the correction factor,  $\alpha_{T2}$  and  $\beta_{T2}$ , and then we computed the factor  $\alpha_{T2}/\beta_{T2}$  for all the three models separately. The relative differences between the extreme values of  $\alpha_{T2}/\beta_{T2}$  and the average one were used to define the relative systematic uncertainties.
- The model dependence on the Monte Carlo correction factors due to the cut on the main vertex Z position in the event selection. The procedure here is totally analogous to the one described for the T2 selection.
- The model dependence on the Monte Carlo correction factor due to the feed-down from weak decays. Since the feed-down is corrected at the track level, only the  $\beta$  factor has to be taken into account. Because of the feed-down correction was done by using the measured  $\Lambda(\bar{\Lambda})$  and  $K_S^0$  spectra (see Sec. 7.7.1), this contribution is very small. Similarly to what is done for the previous contributions, the factor beta due to feed-down was isolated,  $\beta_{FD}$  and computed for all the models. Then, the relative differences on the factor  $1/\beta_{FD}$  were used to define the systematic uncertainties.
- The differences on the spectra obtained by using only RST and WST dataset separately. Since the particle identification is already done separately, only the Monte Carlo correction has to be repeated. The differences observed between RST and WST spectra are small, reaching 3% at most for few phase space bins, and they come from systematic differences between data and simulations. The systematic uncertainties here were estimated by taking the relative differences between RST/WST spectra and the combined one.

Second, the sources of systematic uncertainties accounted for in spectra of the  $V^0$  particles are:

- The model dependence on the Monte Carlo correction factors due to the T2 event selection. The followed procedure is exactly the same described for the charged hadron analysis.
- The model dependence on the Monte Carlo correction factors due to the cut on the main vertex Z position in the event selection. The followed procedure is exactly the same described for the charged hadron analysis.
- The model dependence on the Monte Carlo correction factor due to the feed-down from weak decays. The followed procedure is exactly the same described for the charged hadron analysis.
- The shape of the background used on the  $m_{\text{inv}}$  fit step was changed from a second-degree to a third-degree polynomial function. In this case, only the signal extraction step had to be repeated and the systematic uncertainty were computed as the relative difference between the particle multiplicity obtained by the new background function and the standard one.
- The minimum number of cluster required on the daughter tracks on the  $V^0$  selection was changed from 30 to 20. In this case, both the signal extraction and the Monte Carlo correction had to be repeated for the new  $V^0$  selection. Again the systematic uncertainty was computed as the relative difference between the particle multiplicity obtained by the new selection and the standard one.

In Sec. 7.9, both statistical and systematic uncertainties are shown separately for the particle spectra.

### 7.8.3 Integration over $p_T$

The single differential spectra  $dn/dp$  can be obtained by integrating the double differential spectra, given by Eq. (7.23), over  $p_T$ . Since the measured spectra do not cover all the  $p_T$  range, an extrapolation is needed to perform the integration. This was done by fitting the double differential as a function of the  $p_T$  for each  $p$  bin and then using the integral of the fitted function to extrapolate the measured spectra. In this work, we have decided to use a function defined by a Gaussian function convoluted to an exponential one. The  $p_T$  integrated spectra is than computed by sum over all the  $p_T$  bins in which the measured spectra is available and add to the result the integral of the fitted function over the remain  $p_T$  range. The final  $p_T$  integrated spectra results were limited to the  $p$  bins in which the fraction of the extrapolation is smaller than 5% of the total. This was done to avoid large systematic uncertainties due to the choice of the function used for the extrapolation.

## 7.9 Results

(DO IT)

## 7.10 Summary and conclusions

(DO IT)

In this chapter we have presented the analysis of the hadron production in  $\pi^-$ -C interactions measured by NA61/SHINE experiment. The spectra of  $\pi^\pm$ ,  $K^\pm$  and  $p(\bar{p})$  were obtained by means of a particle identification method based on the  $dE/dx$  measurements and the  $\Lambda(\bar{\Lambda})$  and  $K_S^0$  by means of the  $m_{\text{inv}}$  spectra analysis.

The results obtained here will greatly impact the understanding of the muon production in air showers. Our measurements will surely have an important role on the tuning of the next generations of the hadronic interaction models. In terms of number of muons, a direct prediction can be done by looking to the  $\bar{p}$  spectra in ??. Some of the current models, like EPOS 1.99 and SIBYLL 2.3, (???) show to be nearly compatible with our measured spectra. This means that the excess of measured muons relative to simulations is likely not caused by an overall underestimation of the (anti)baryons production by the models.

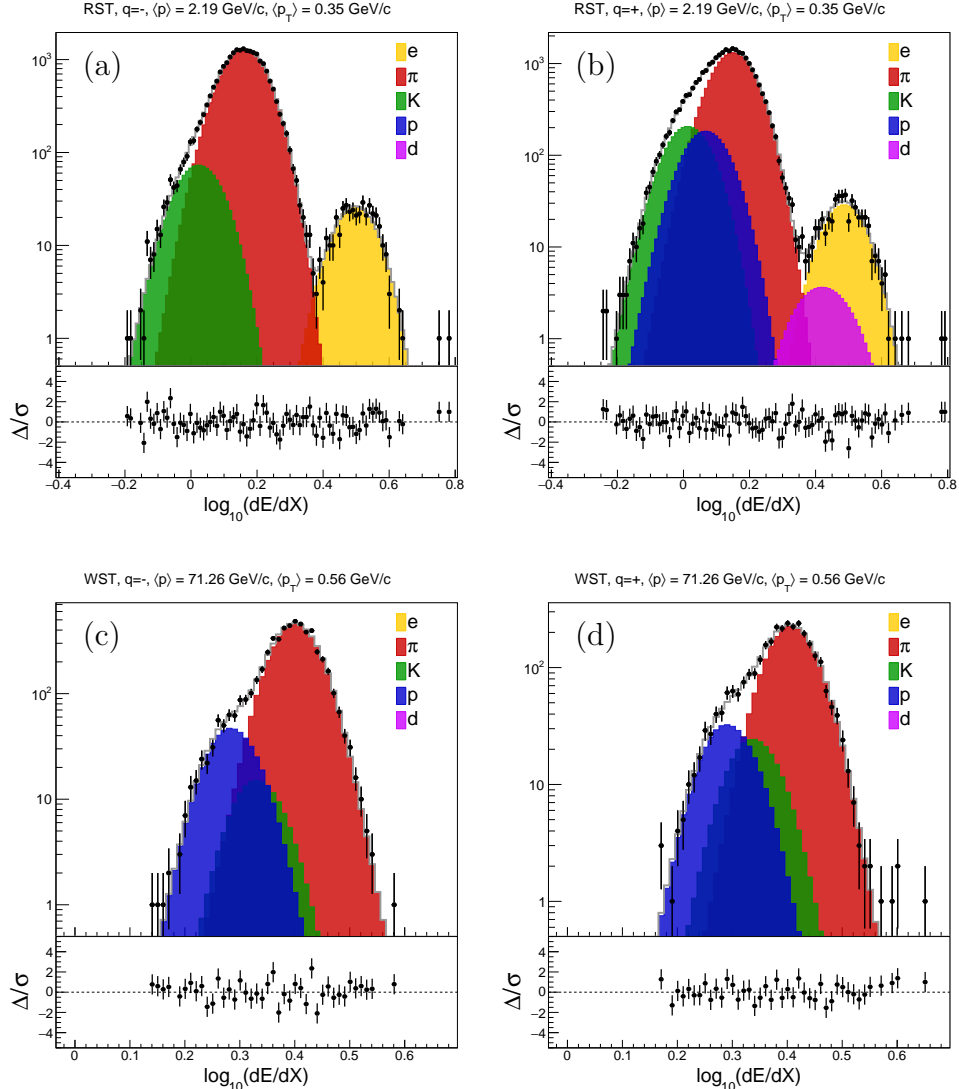


Figure 27 – Examples of the fitted  $dE/dx$  distributions from the 350 GeV/c dataset. On the top, the distributions of the (a) negatively and (b) positively charged tracks are shown for one phase space bin of the RST subset. On the bottom, the distributions of the (c) negatively and (d) positively charged tracks are shown for a different phase space bin of the WST subset. The values of the  $\langle p \rangle$  and  $\langle p_T \rangle$  for each phase space bin is indicated on the top of each plot. The black dots show the observed number of tracks, while the colored distributions are the results of the  $dE/dx$  fit for each particle type. On the bottom of each plot, we show the residual of the fit, defined as the difference between the observed and the expected number of tracks from the result of the fit, divided by the uncertainty of the observed number.

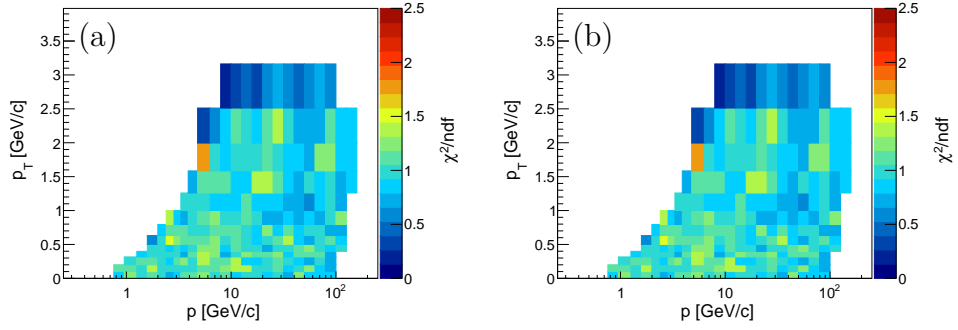


Figure 28 –  $\chi^2/\text{ndf}$  of the  $dE/dx$  fit for the 350 GeV/ $c$  data set. The RST and WST are shown in (a) and (b), respectively.

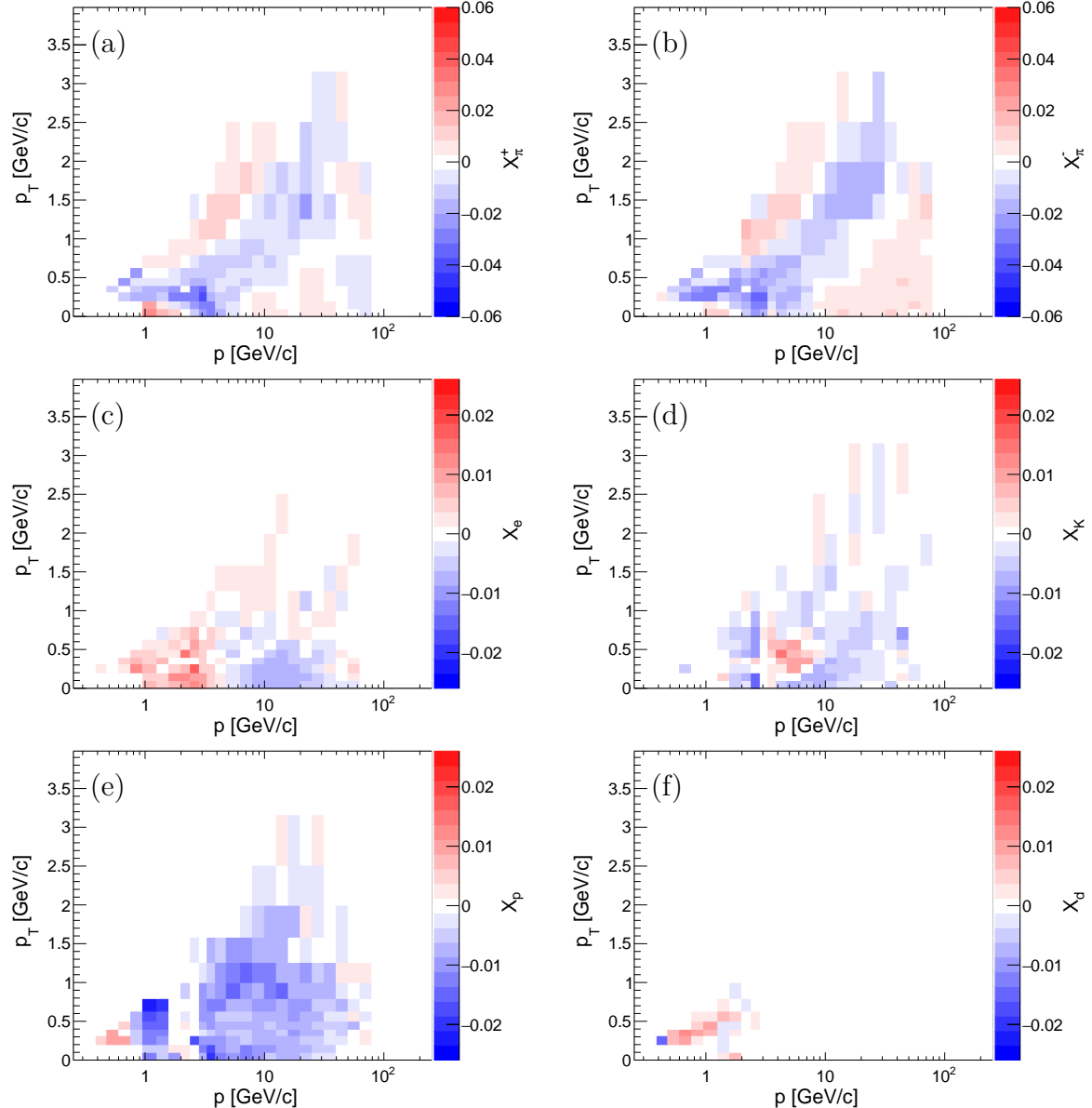


Figure 29 – Calibration constants obtained from the  $dE/dx$  fit of the WST and 158 GeV/ $c$  data set.

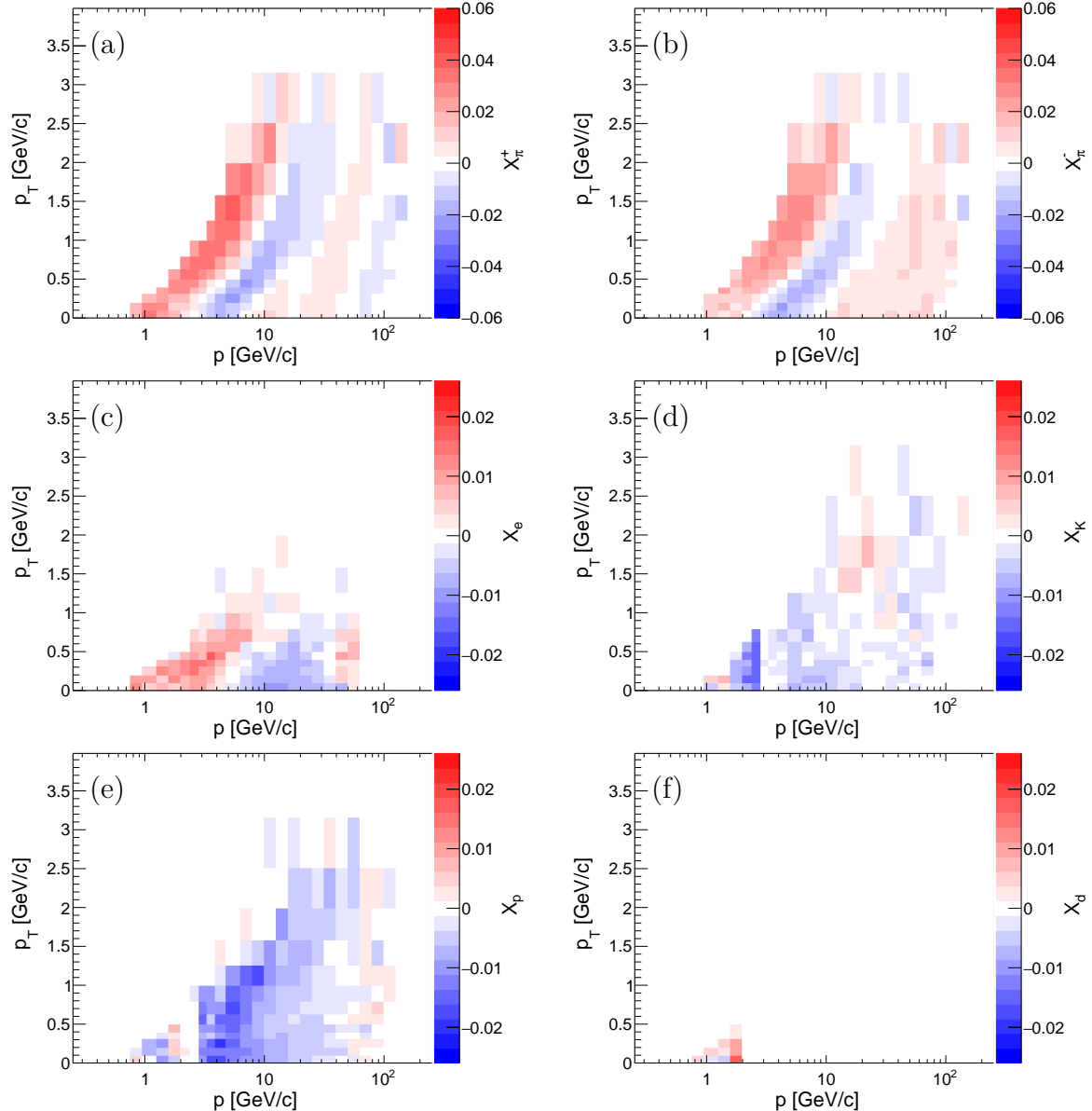


Figure 30 – Calibration constants obtained from the  $dE/dx$  fit of the RST and 350 GeV/c data set.

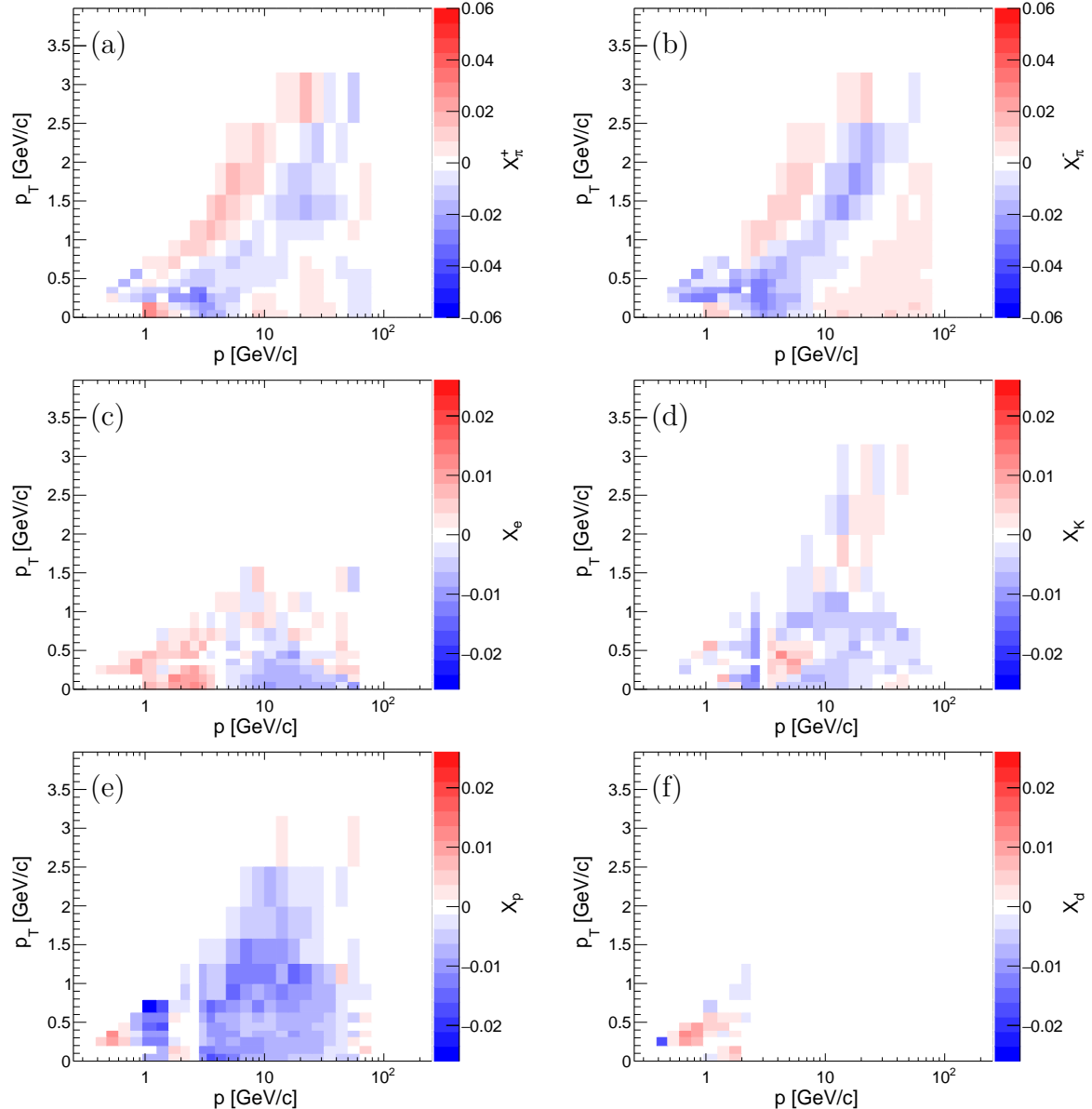


Figure 31 – Calibration constants obtained from the  $dE/dx$  fit of the WST and 350 GeV/ $c$  data set.

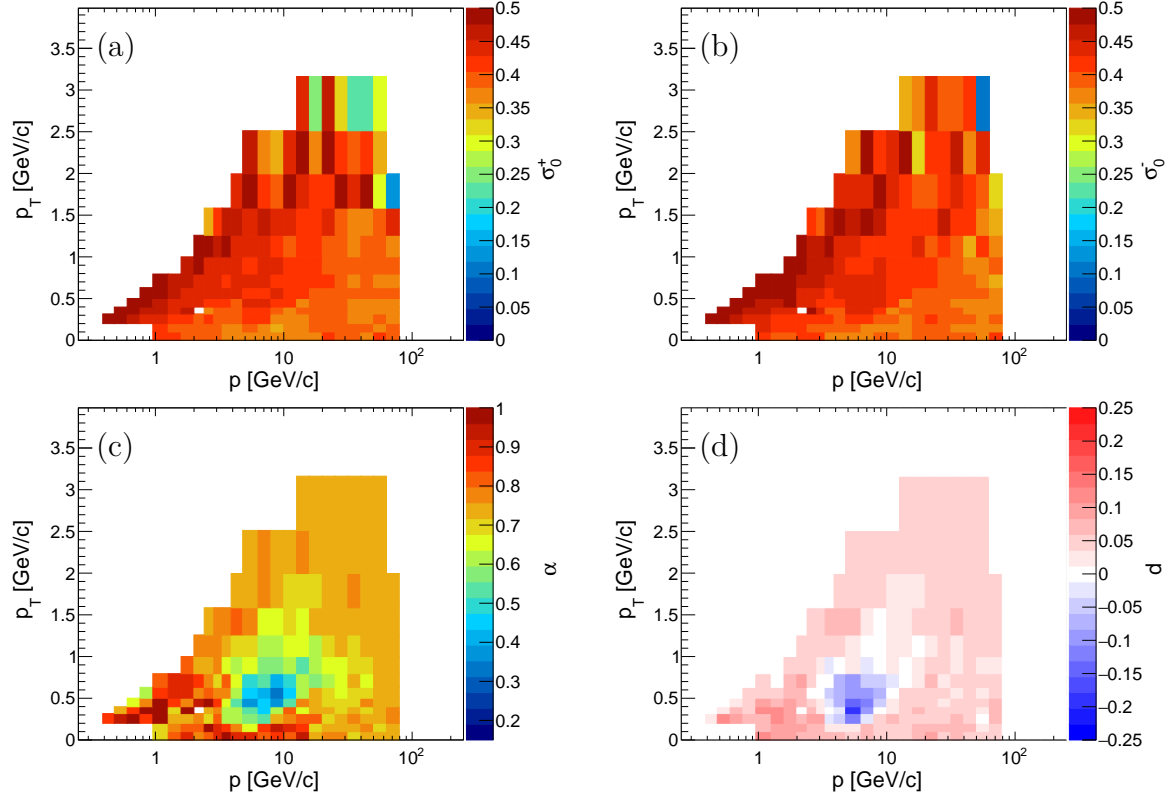


Figure 32 – Shape parameters obtained from the  $dE/dx$  fit of the WST and 158 GeV/ $c$  data set.

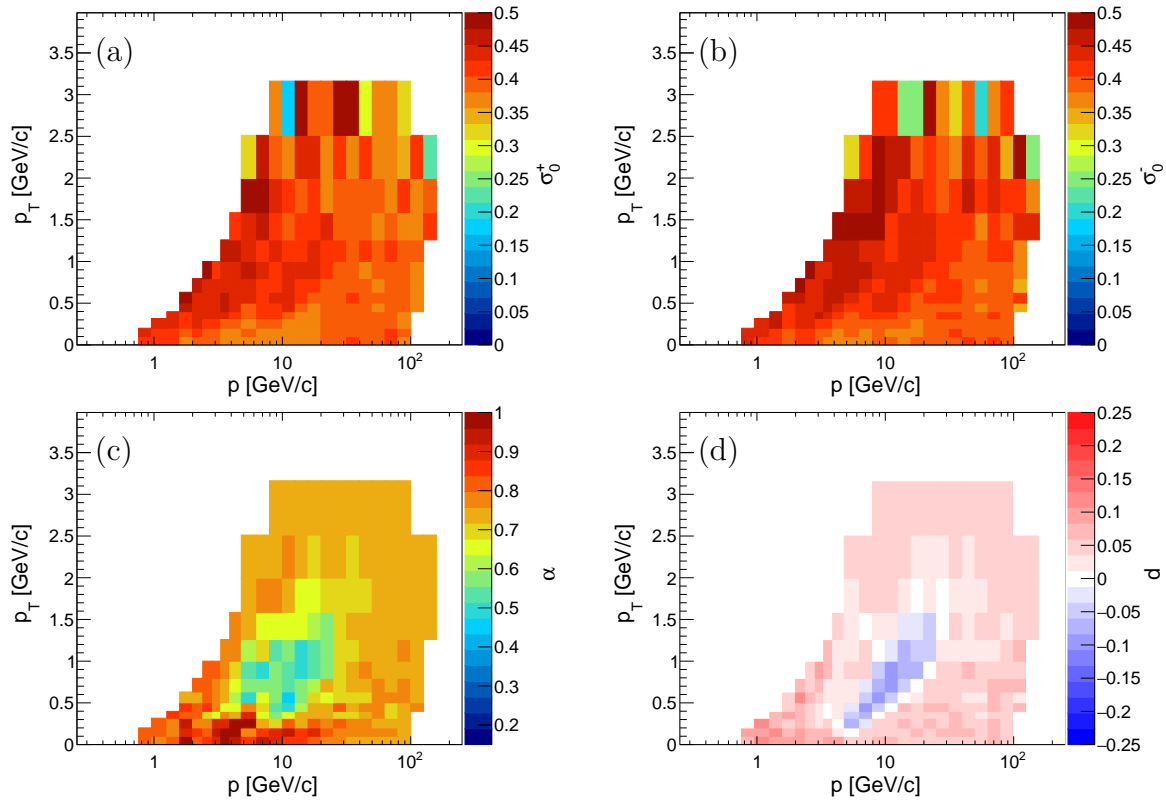


Figure 33 – Shape parameters obtained from the  $dE/dx$  fit of the RST and 350  $\text{GeV}/c$  data set.

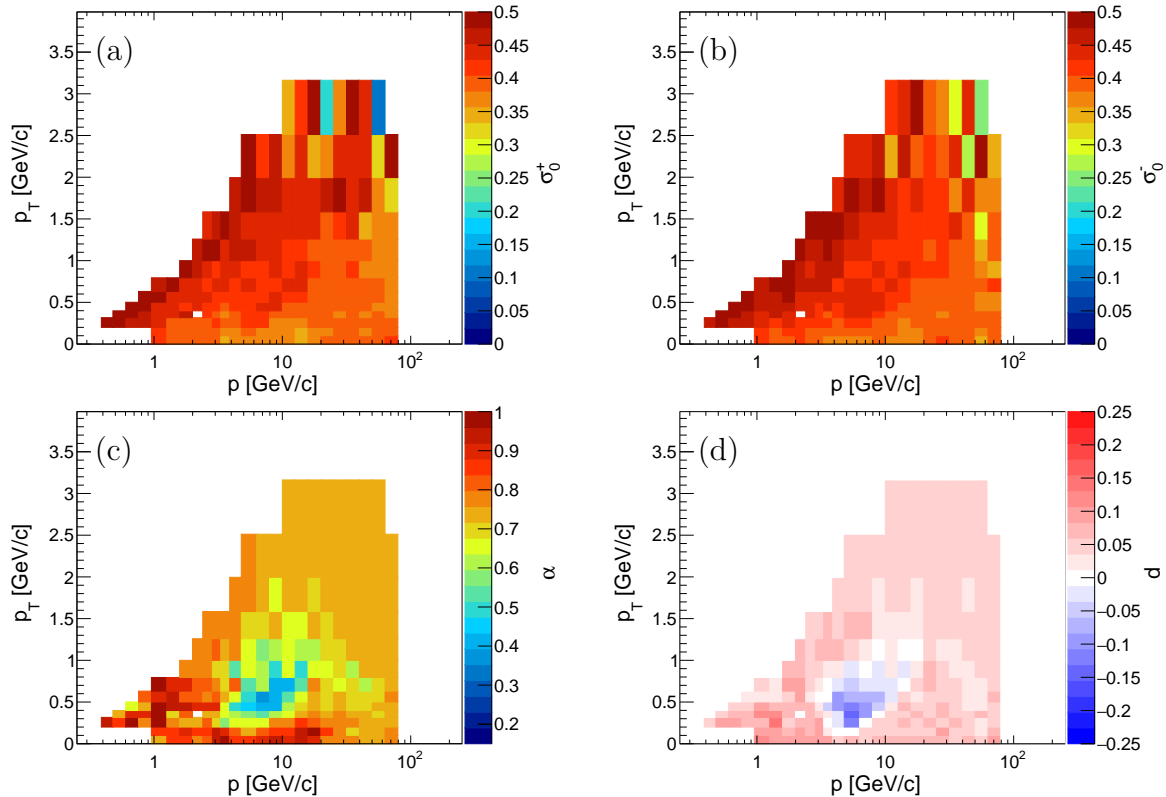


Figure 34 – Shape parameters obtained from the  $dE/dx$  fit of the WST and 350  $\text{GeV}/c$  data set.

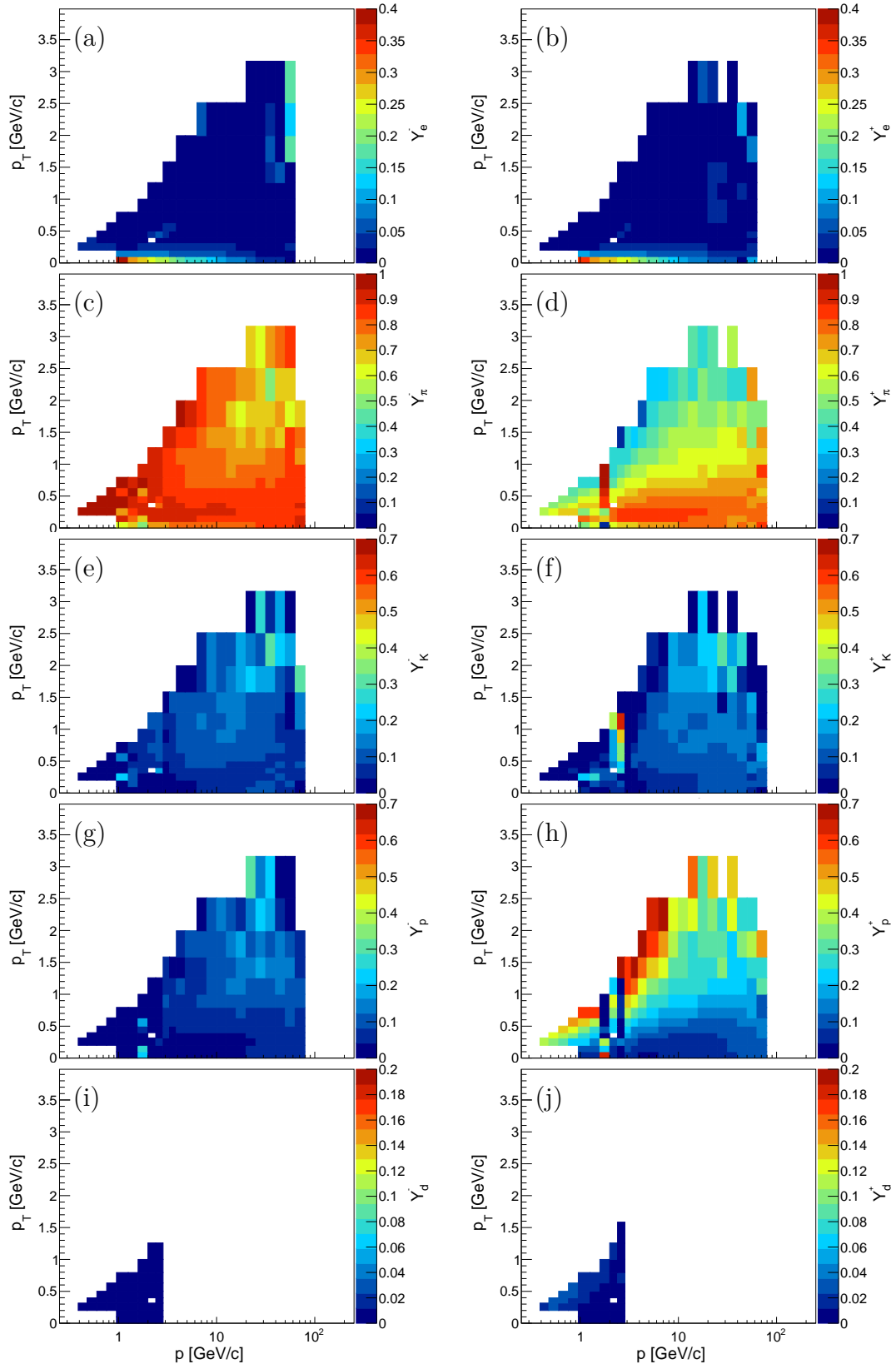


Figure 35 – Particle fractions obtained from the  $dE/dx$  fit of the WST and 158 GeV/c data set.

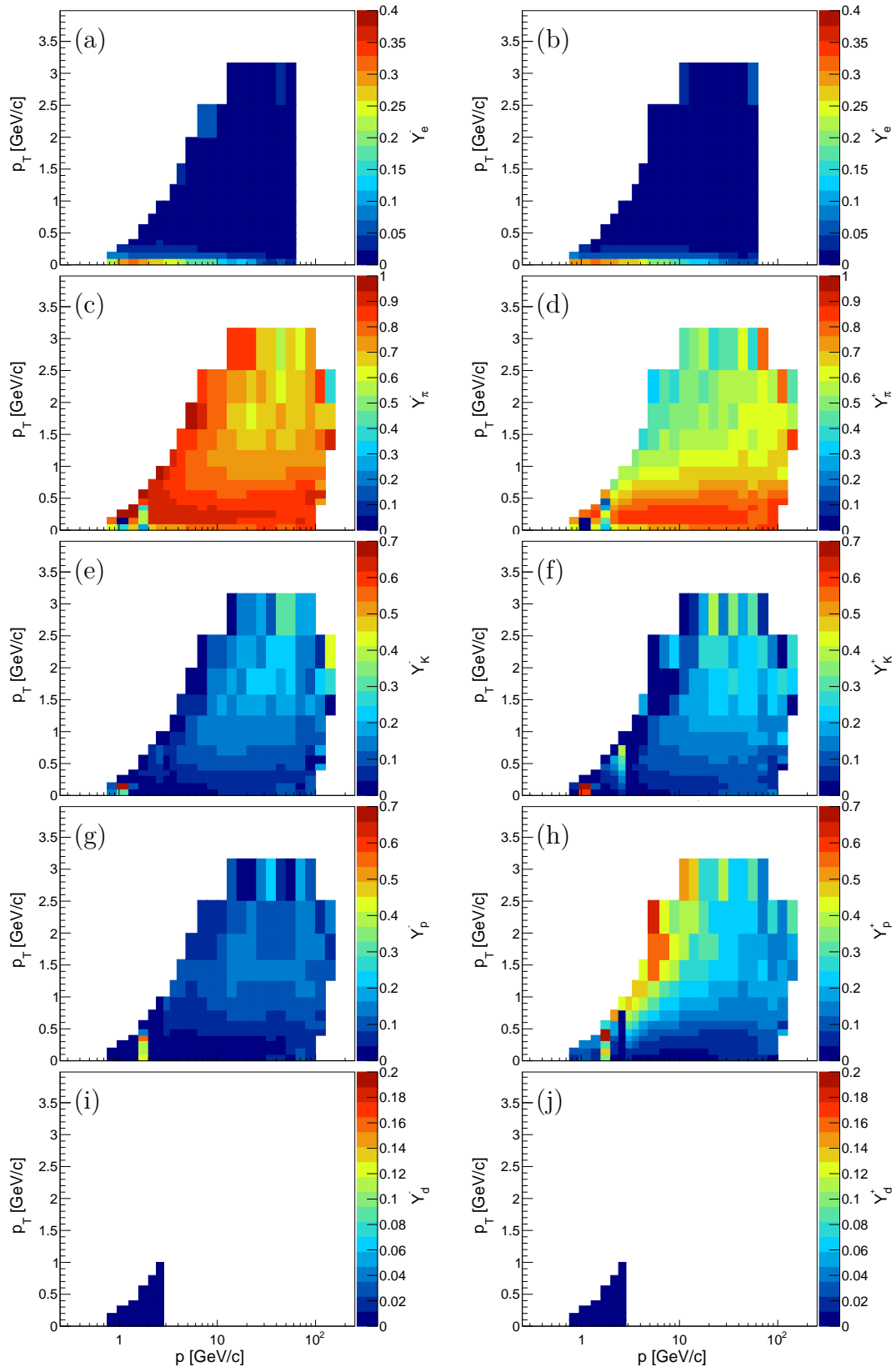


Figure 36 – Particle fractions obtained from the  $dE/dx$  fit of the RST and 350 GeV/ $c$  data set.

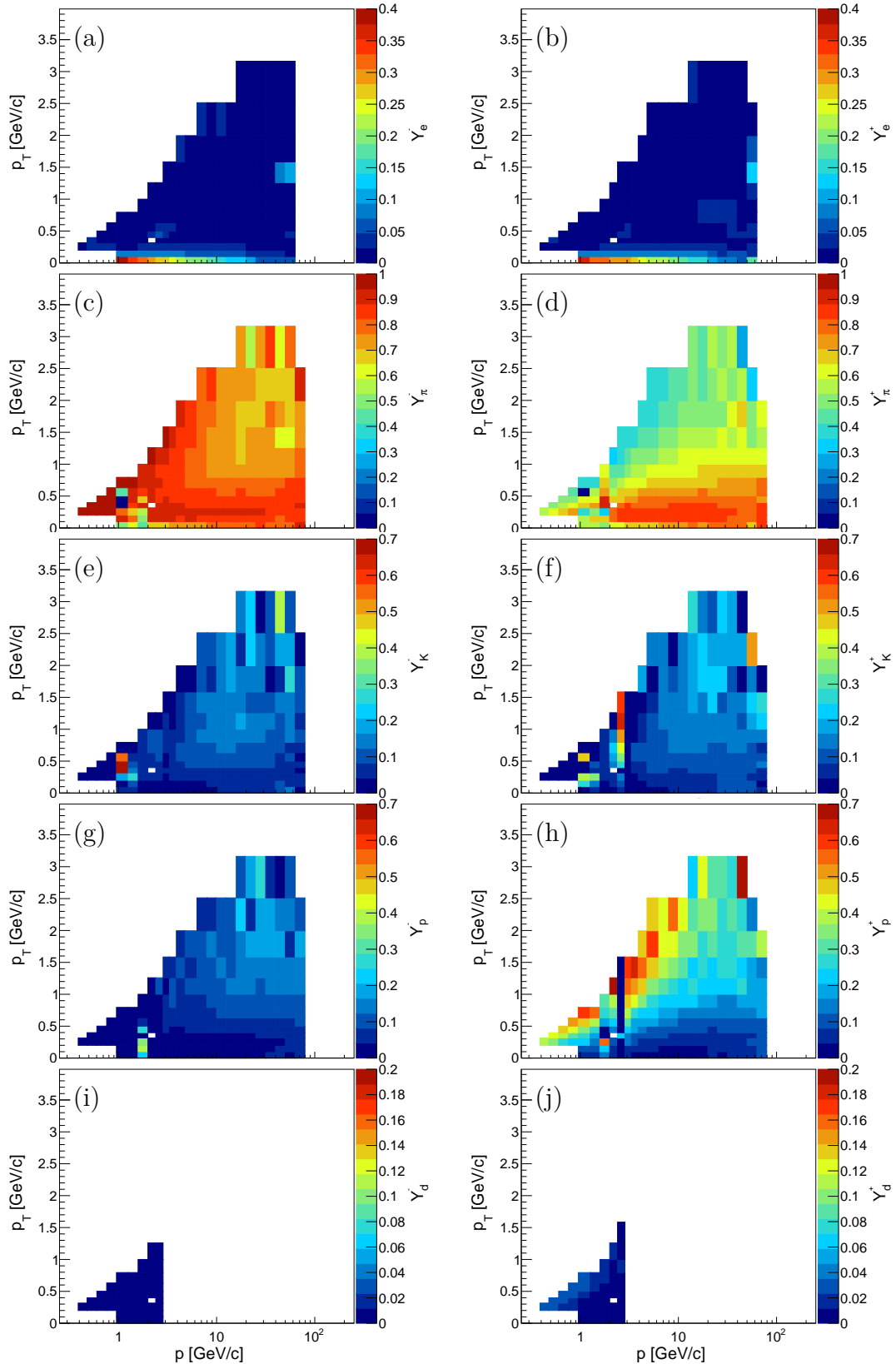


Figure 37 – Particle fractions obtained from the  $dE/dx$  fit of the WST and 350 GeV/c data set.

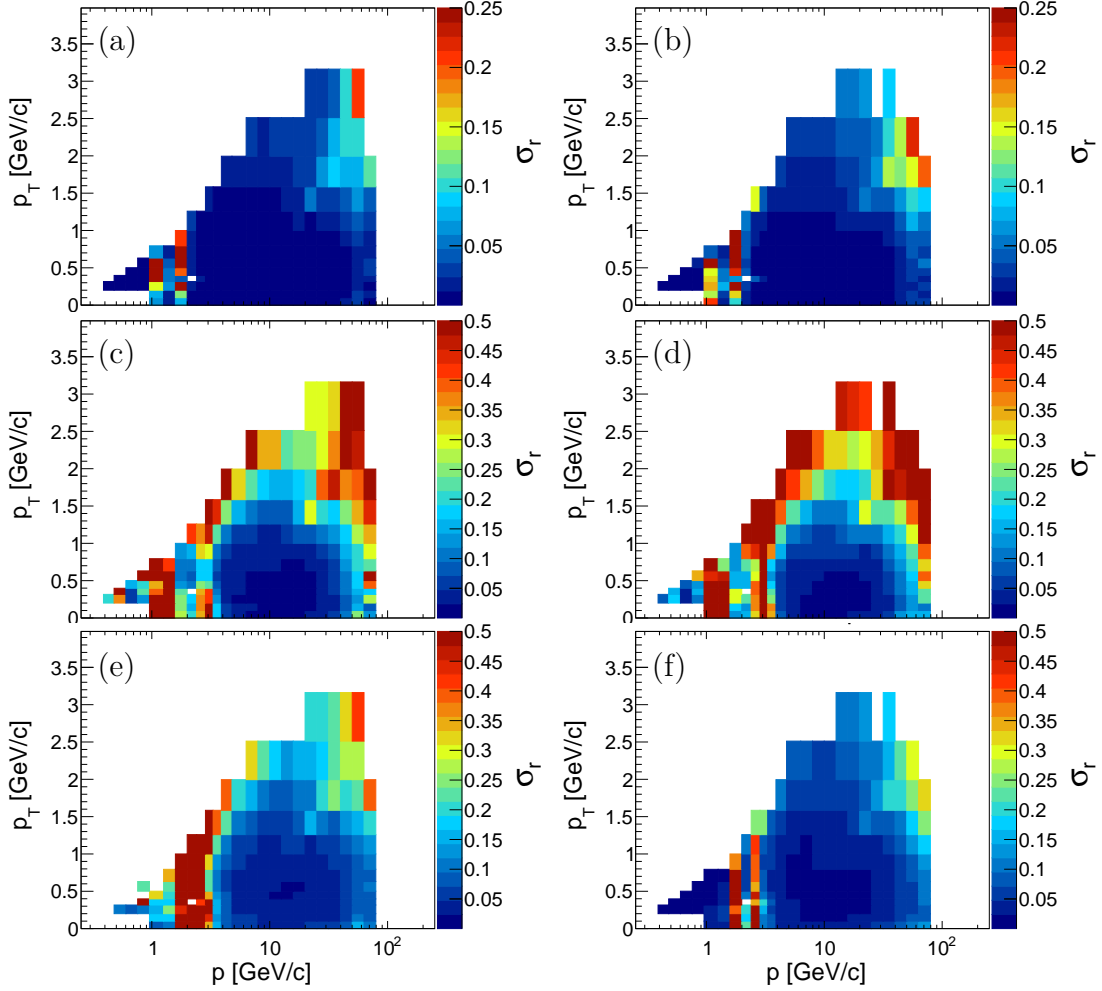


Figure 38 – Relative standard deviation ( $\sigma_r$ , see the definition in the text) of the particle fractions obtained with the SDEs for the WST and 158  $\text{GeV}/c$  case. The  $\pi^+$  case is shown in (a),  $\pi^-$  in (b),  $K^+$  in (c),  $K^-$  in (d),  $p^+$  in (e) and  $p^-$  in (f).

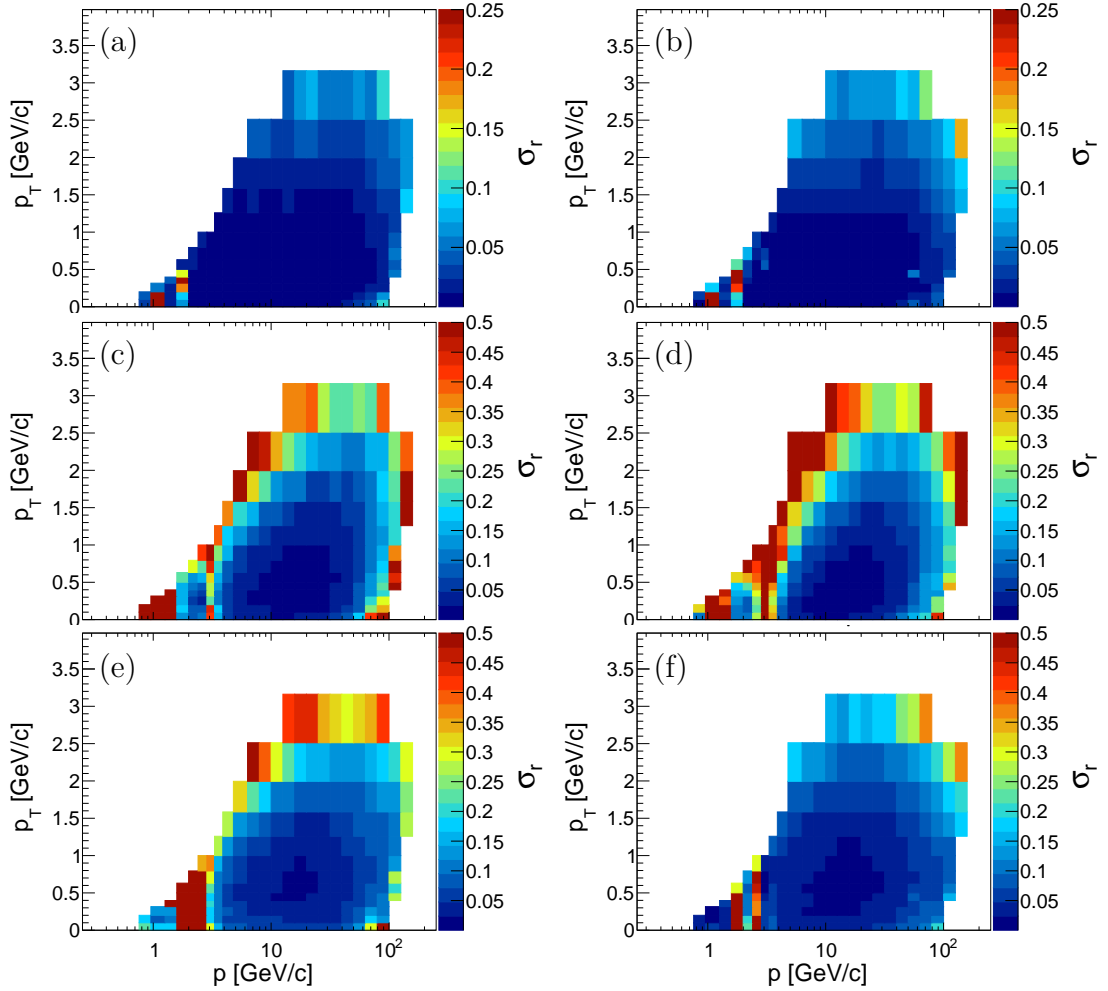


Figure 39 – Relative standard deviation ( $\sigma_r$ , see the definition in the text) of the particle fractions obtained with the SDEs for the RST and 350 GeV/c case. The  $\pi^+$  case is shown in (a),  $\pi^-$  in (b),  $K^+$  in (c),  $K^-$  in (d),  $p^+$  in (e) and  $p^-$  in (f).

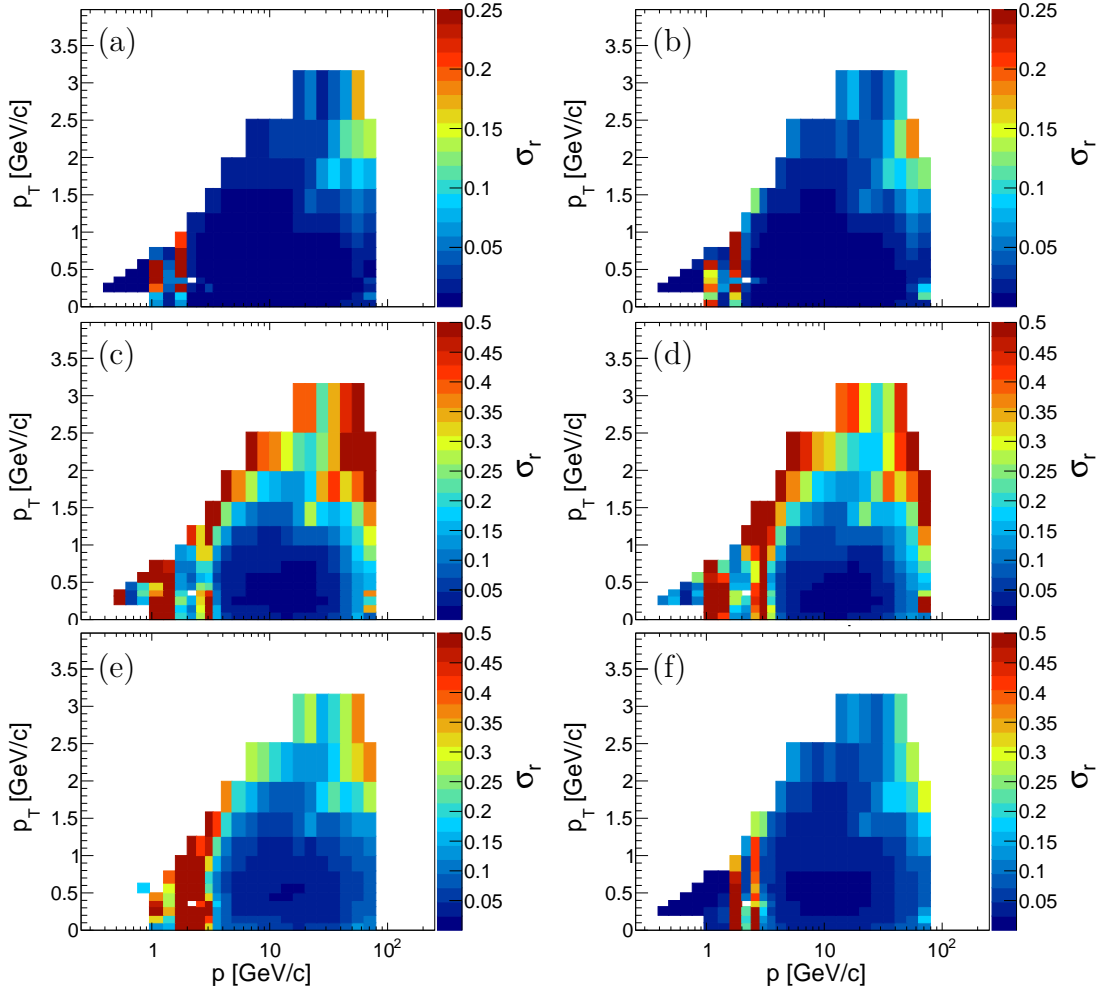


Figure 40 – Relative standard deviation ( $\sigma_r$ , see the definition in the text) of the particle fractions obtained with the SDEs for the WST and 350 GeV/c case. The  $\pi^+$  case is shown in (a),  $\pi^-$  in (b),  $K^+$  in (c),  $K^-$  in (d),  $p^+$  in (e) and  $p^-$  in (f).

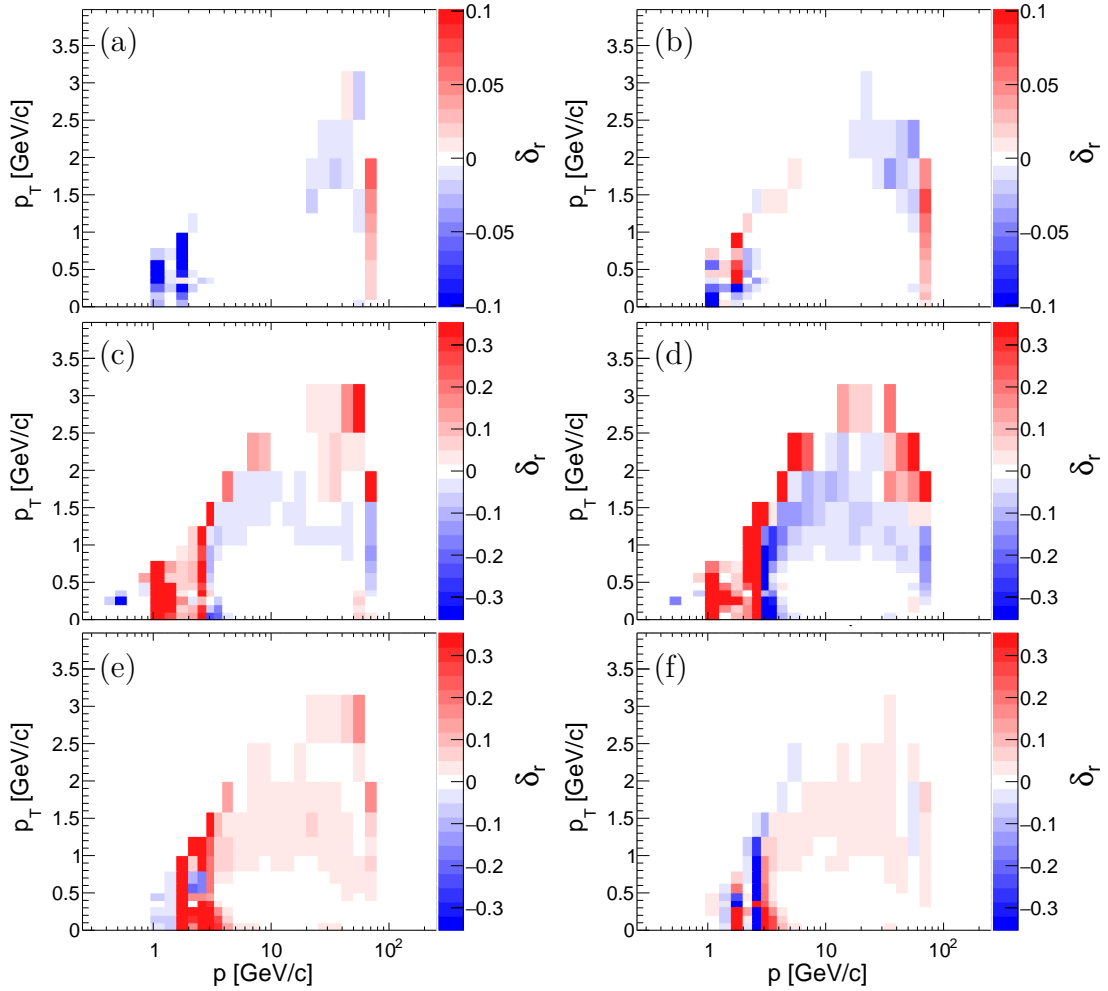


Figure 41 – Average relative bias ( $\delta_r$ , see the definition in the text) of the particle fractions obtained with the SDEs for the WST and 158 GeV/c case. The  $\pi^+$  case is shown in (a),  $\pi^-$  in (b),  $K^+$  in (c),  $K^-$  in (d),  $p^+$  in (e) and  $p^-$  in (f).

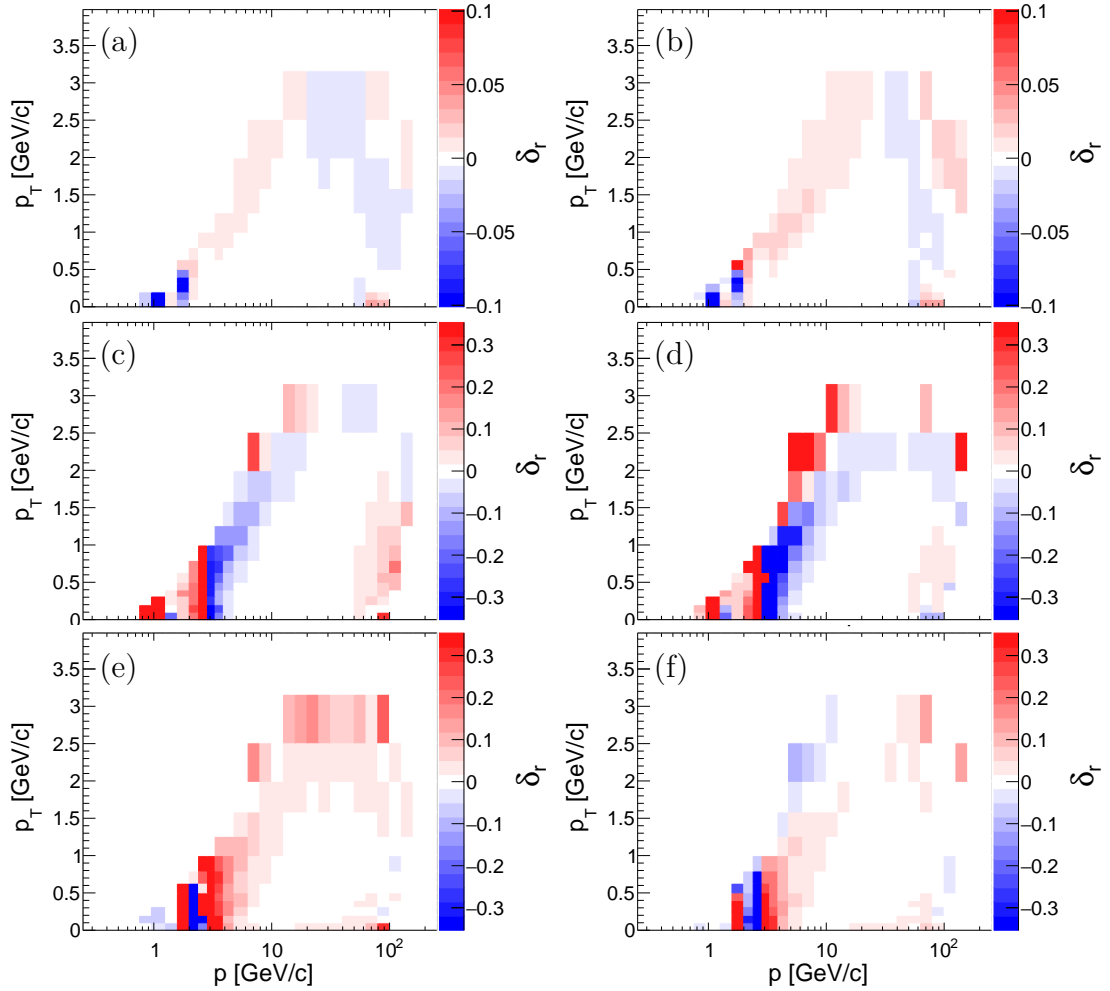


Figure 42 – Average relative bias ( $\delta_r$ , see the definition in the text) of the particle fractions obtained with the SDEs for the RST and 350  $\text{GeV}/c$  case. The  $\pi^+$  case is shown in (a),  $\pi^-$  in (b),  $K^+$  in (c),  $K^-$  in (d),  $p^+$  in (e) and  $p^-$  in (f).

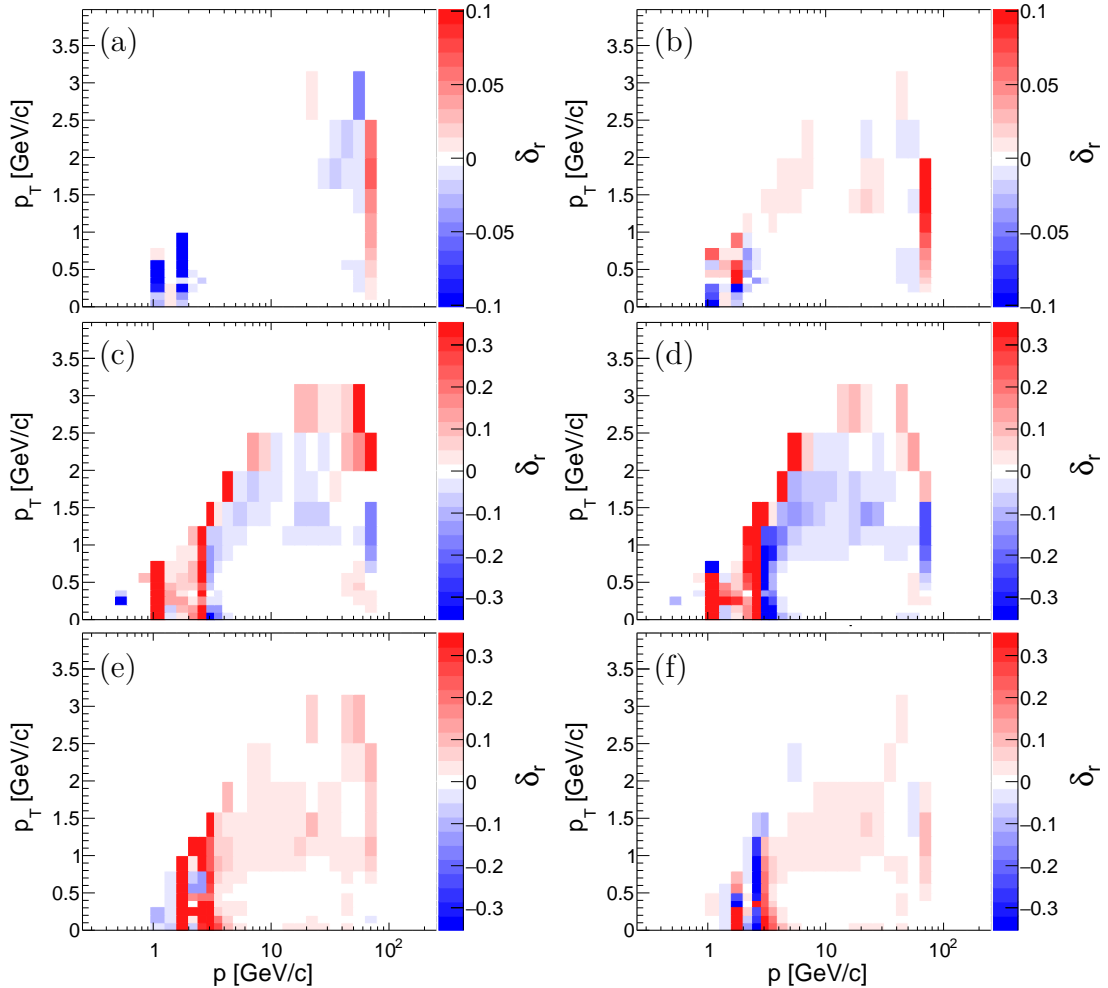


Figure 43 – Average relative bias ( $\delta_r$ , see the definition in the text) of the particle fractions obtained with the SDEs for the RST and 350 GeV/c case. The  $\pi^+$  case is shown in (a),  $\pi^-$  in (b),  $K^+$  in (c),  $K^-$  in (d),  $p^+$  in (e) and  $p^-$  in (f).

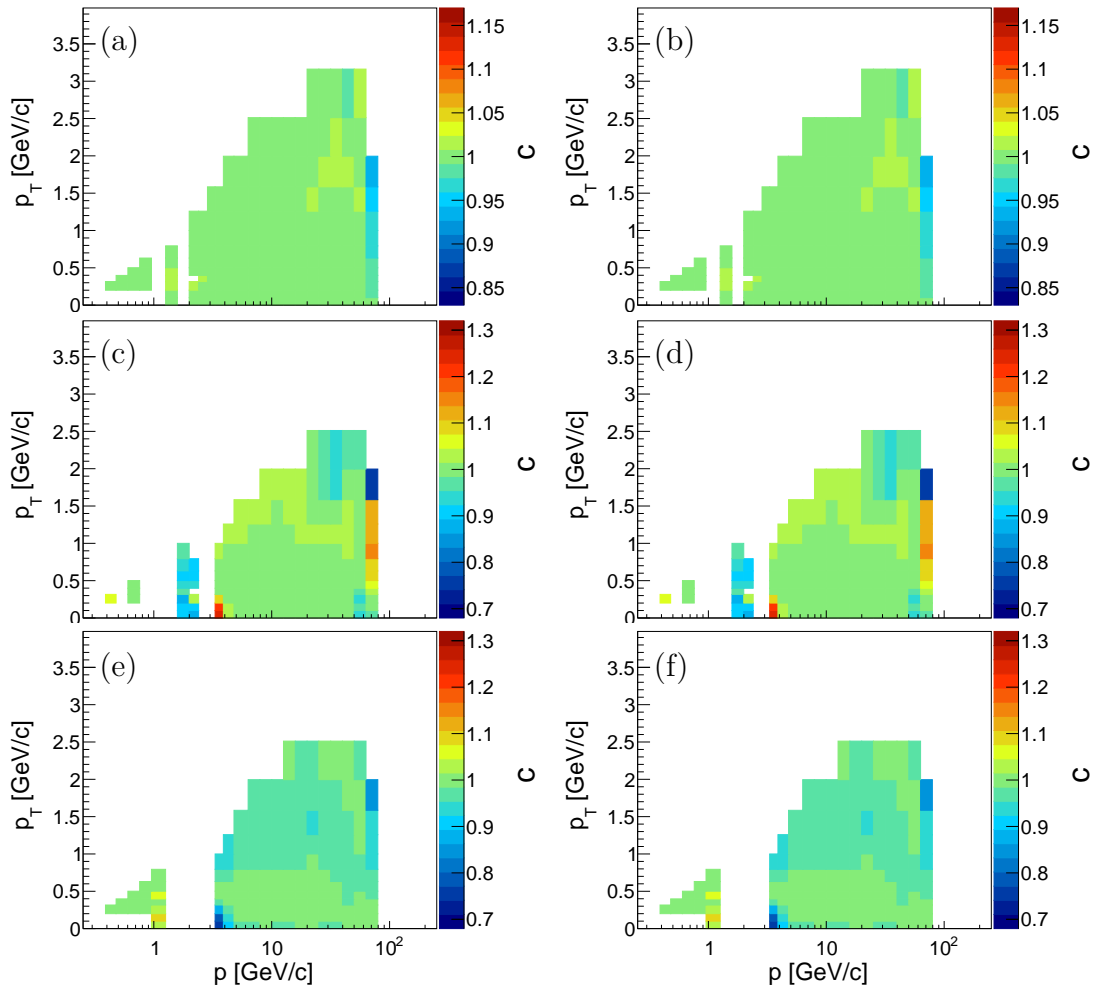


Figure 44 – Correction factors ( $c$ , see the definition in the text) for the WST and 158 GeV/ $c$  case. The  $\pi^+$  case is shown in (a),  $\pi^-$  in (b),  $K^+$  in (c),  $K^-$  in (d),  $p^+$  in (e) and  $p^-$  in (f).

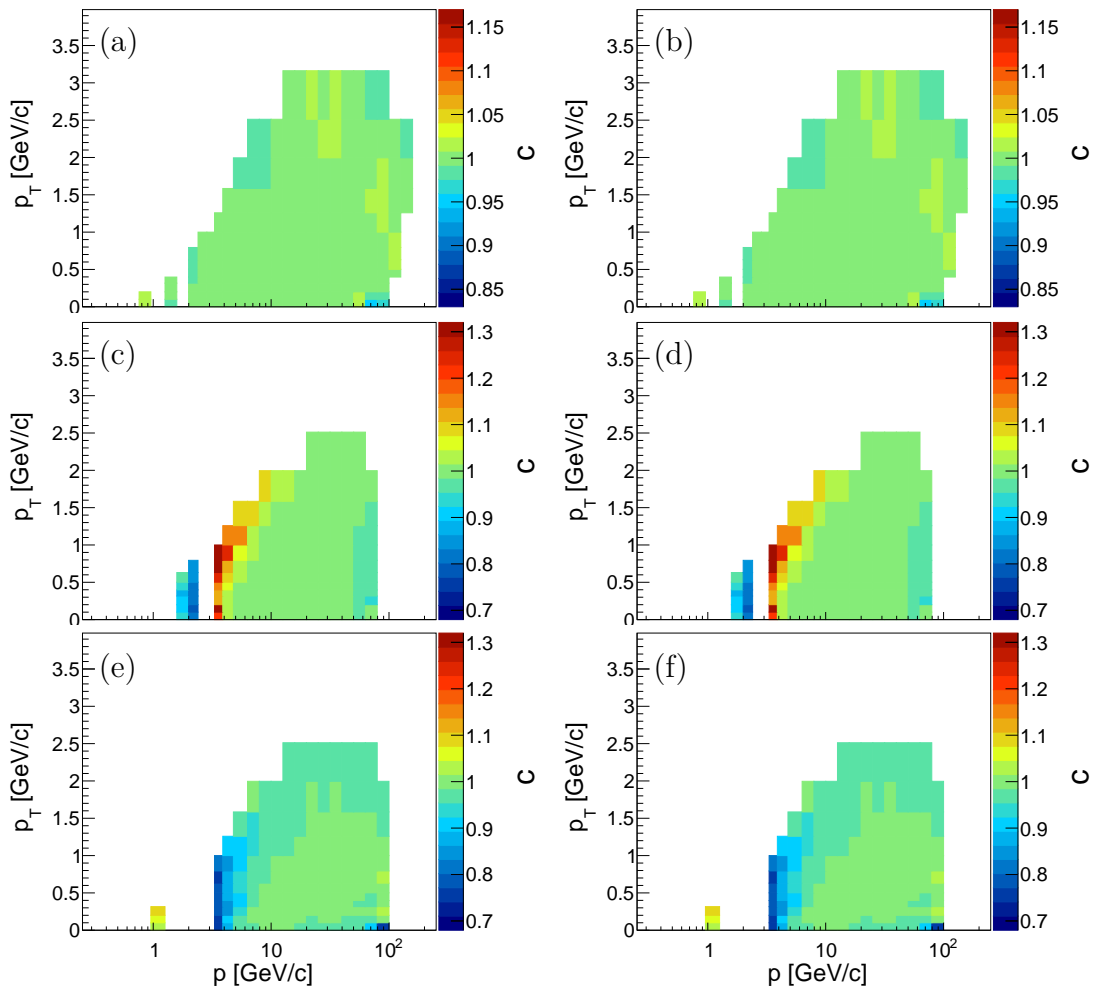


Figure 45 – Correction factors ( $c$ , see the definition in the text) for the RST and 350 GeV/ $c$  case. The  $\pi^+$  case is shown in (a),  $\pi^-$  in (b),  $K^+$  in (c),  $K^-$  in (d),  $p^+$  in (e) and  $p^-$  in (f).

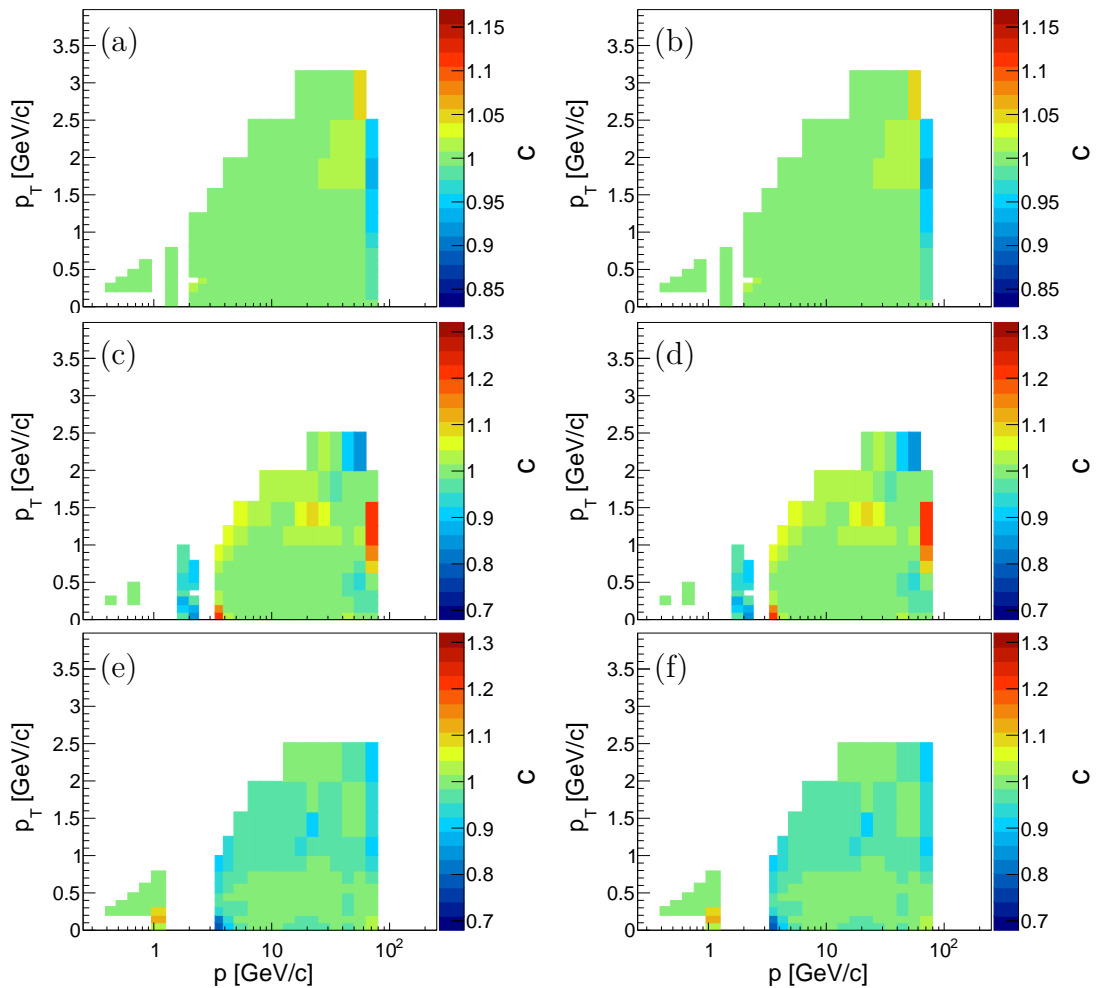


Figure 46 – Correction factors ( $c$ , see the definition in the text) for the RST and 350 GeV/ $c$  case. The  $\pi^+$  case is shown in (a),  $\pi^-$  in (b),  $K^+$  in (c),  $K^-$  in (d),  $p^+$  in (e) and  $p^-$  in (f).

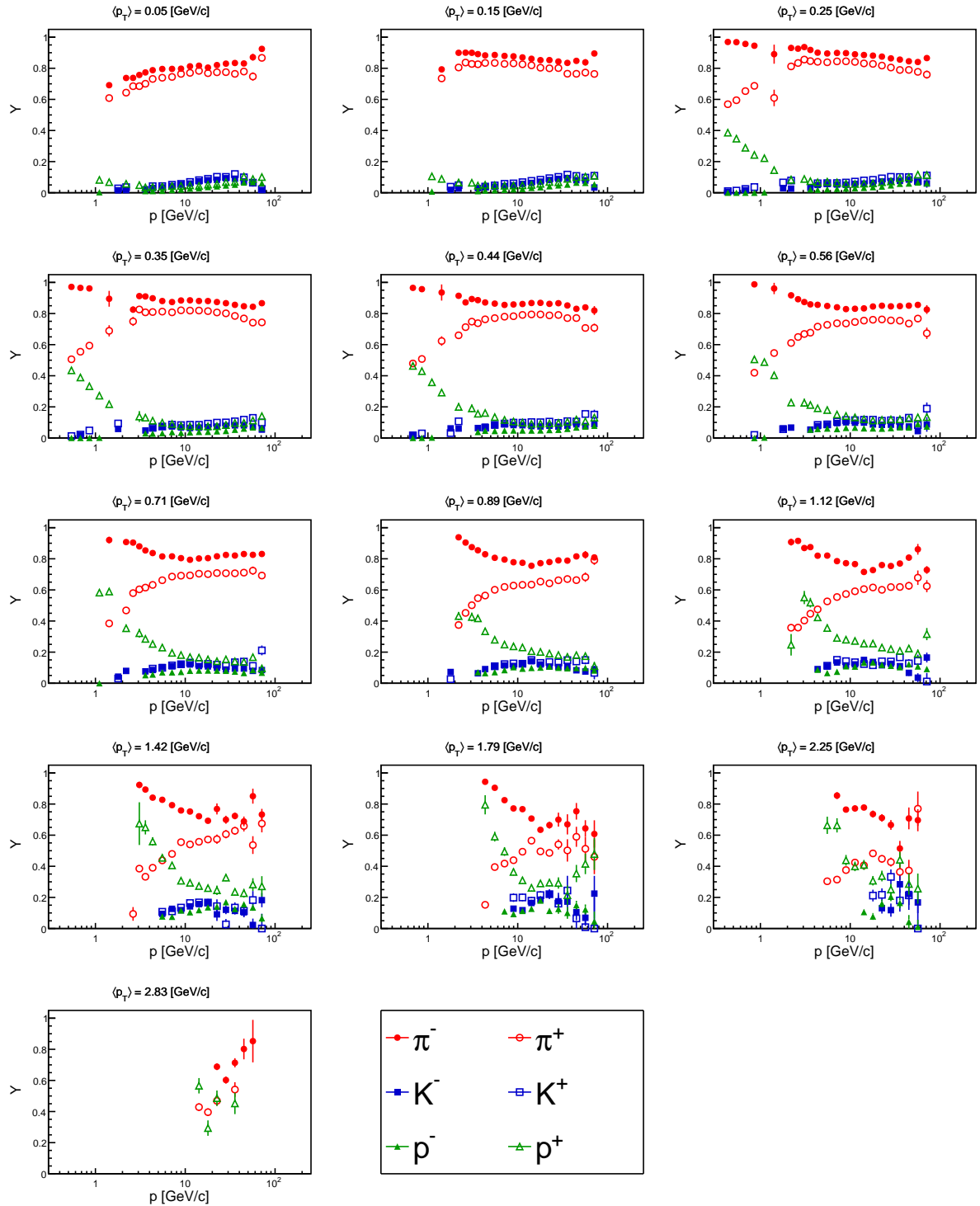


Figure 47 – Particle fractions obtained from the  $dE/dx$  fit of the WST and 158  $\text{GeV}/c$  dataset, with target inserted.

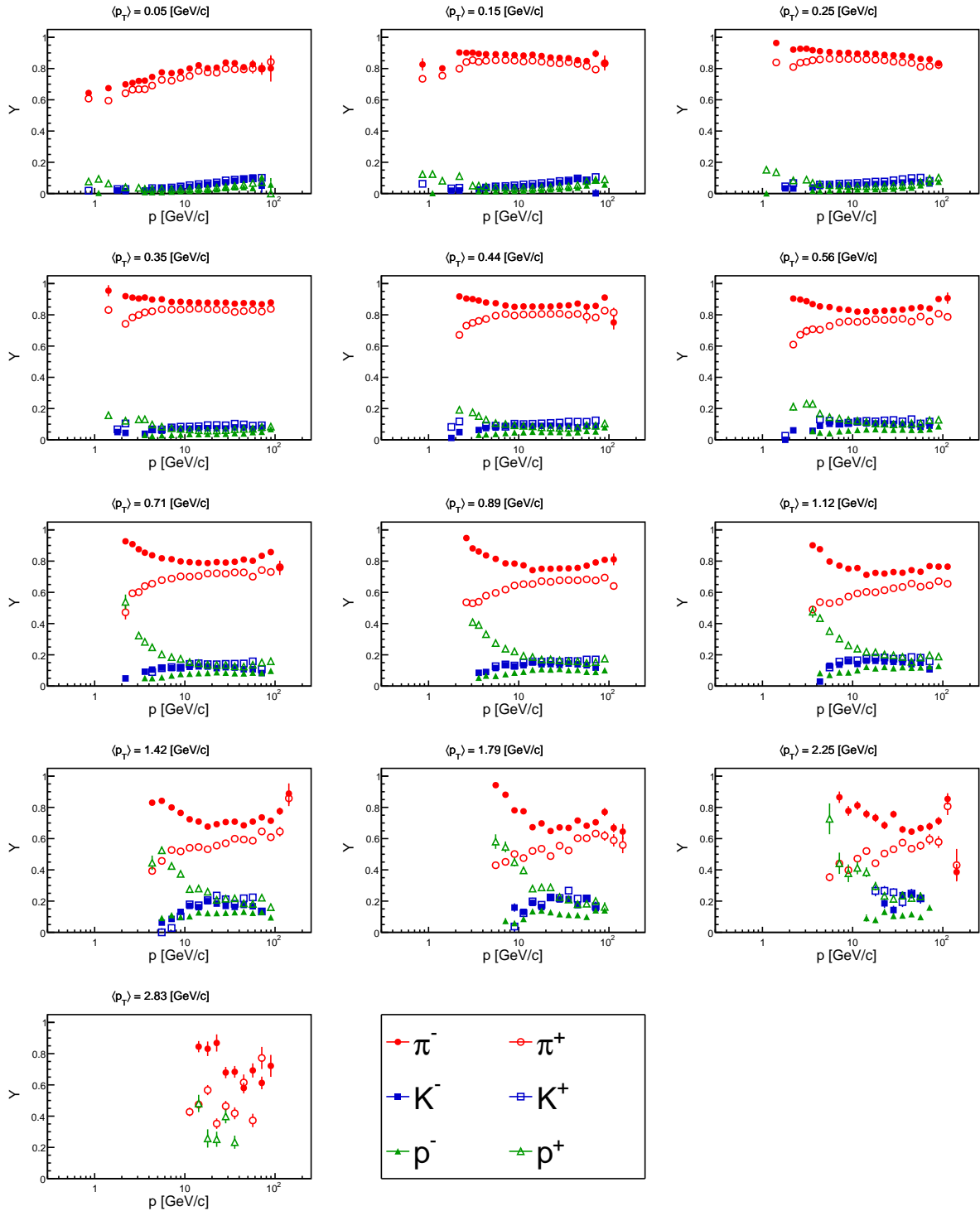


Figure 48 – Particle fractions obtained from the  $dE/dx$  fit of the RST and 350 GeV/ $c$  dataset, with target inserted.

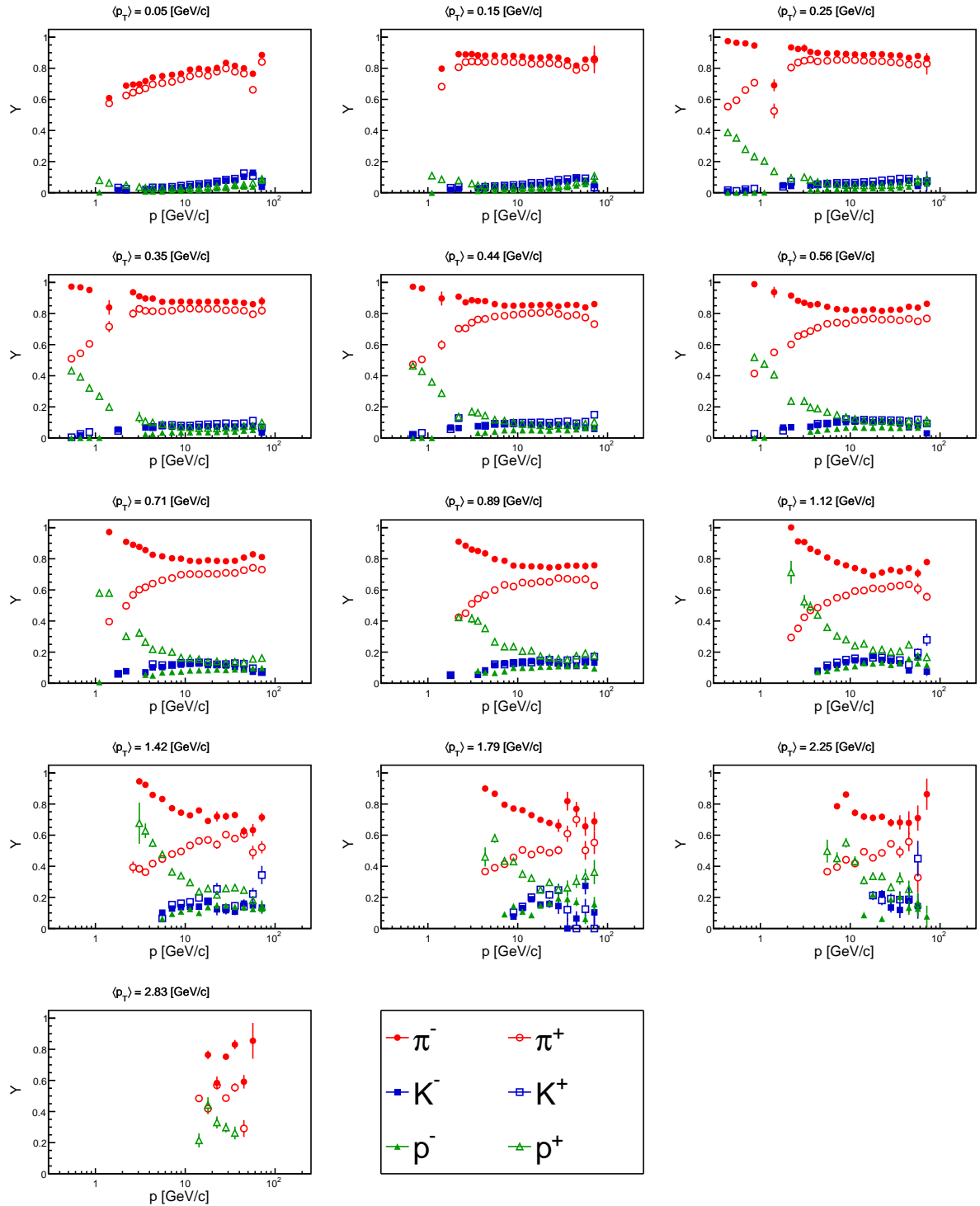


Figure 49 – Particle fractions obtained from the  $dE/dx$  fit of the WST and 350  $\text{GeV}/c$  dataset, with target inserted.

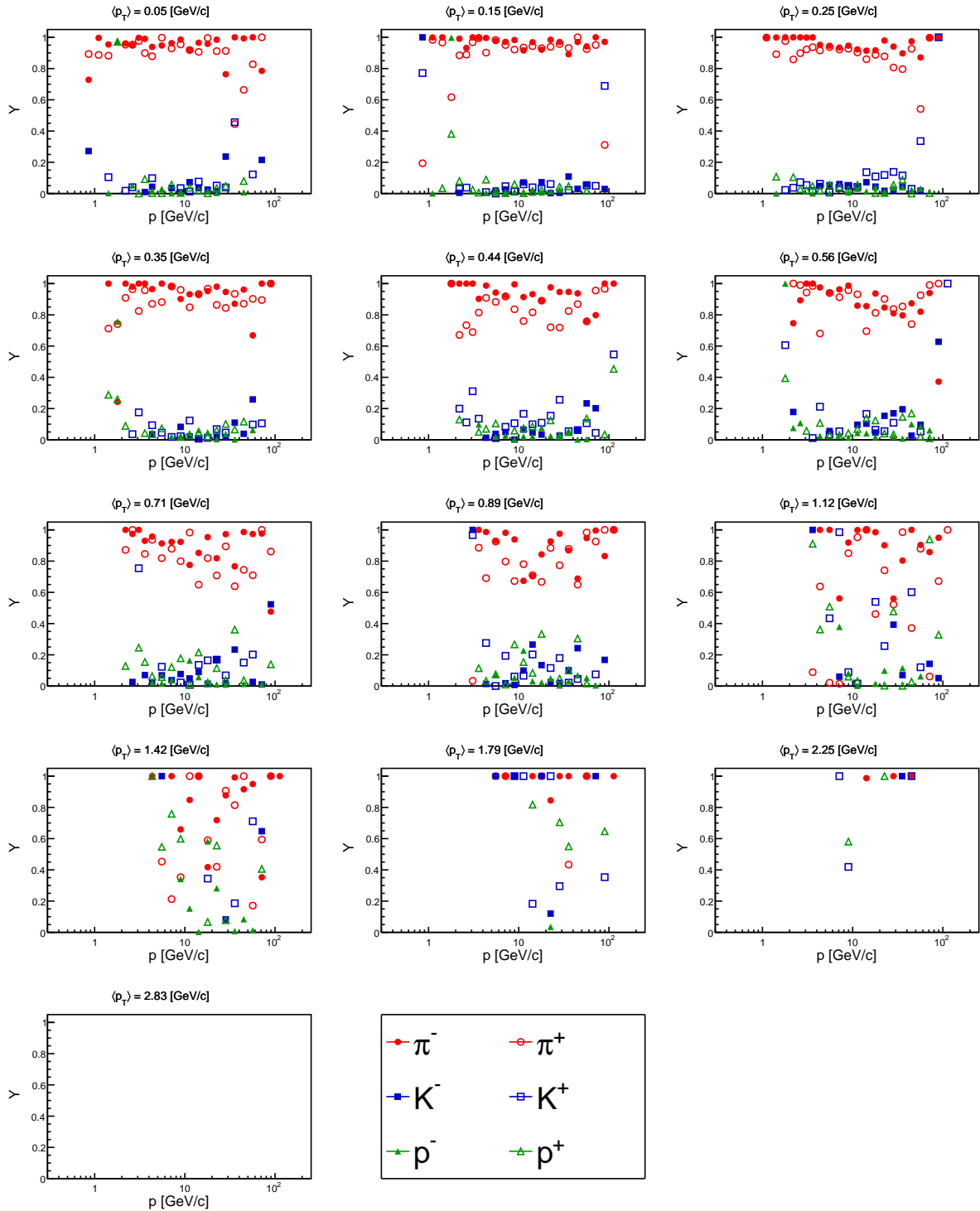


Figure 50 – Particle fractions obtained from the  $dE/dx$  fit of the RST and 158 GeV/ $c$  dataset, with target removed.

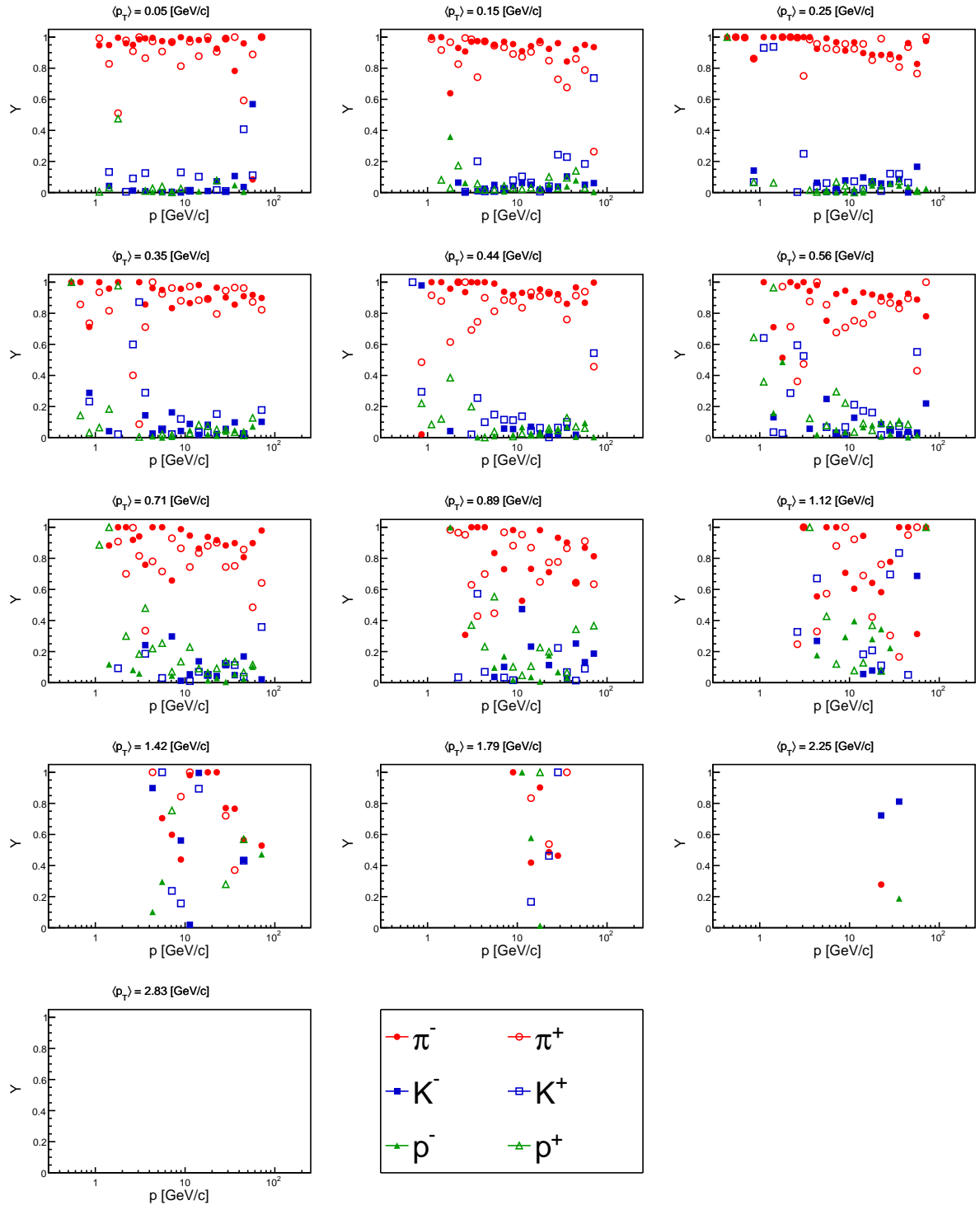


Figure 51 – Particle fractions obtained from the  $dE/dx$  fit of the WST and 158 GeV/c dataset, with target inserted.

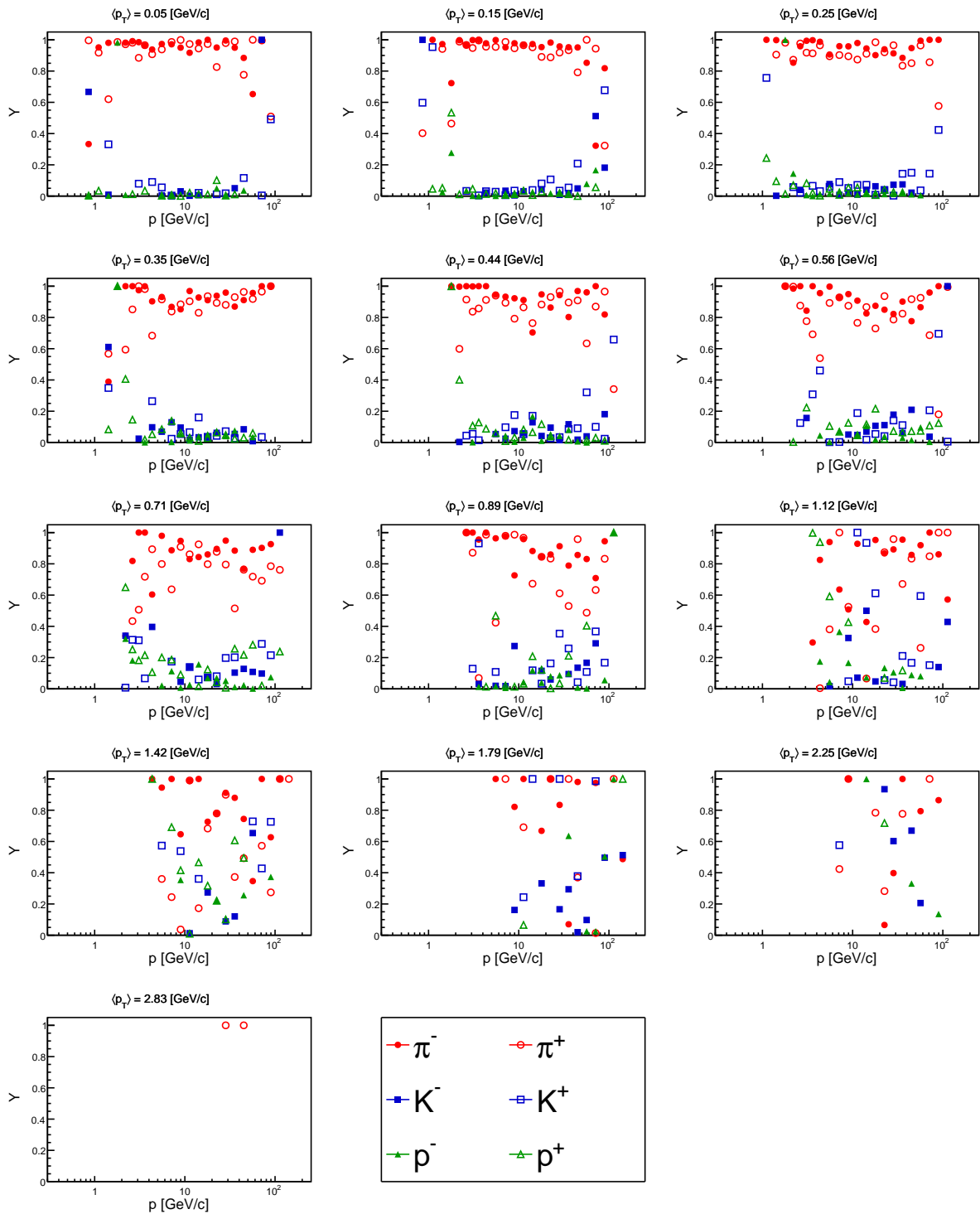


Figure 52 – Particle fractions obtained from the  $dE/dx$  fit of the RST and 350 GeV/ $c$  dataset, with target inserted.

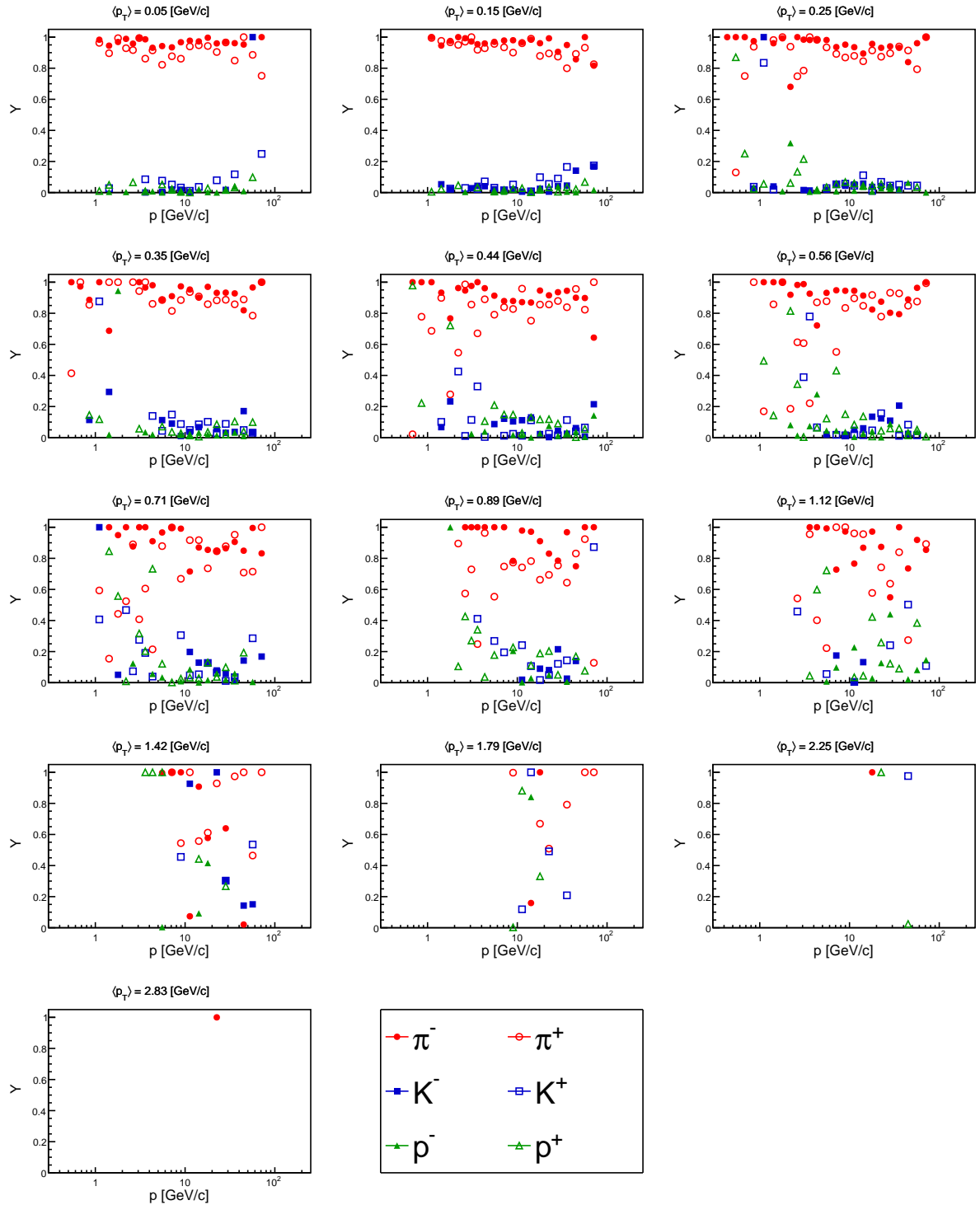


Figure 53 – Particle fractions obtained from the  $dE/dx$  fit of the WST and 350  $\text{GeV}/c$  dataset, with target inserted.

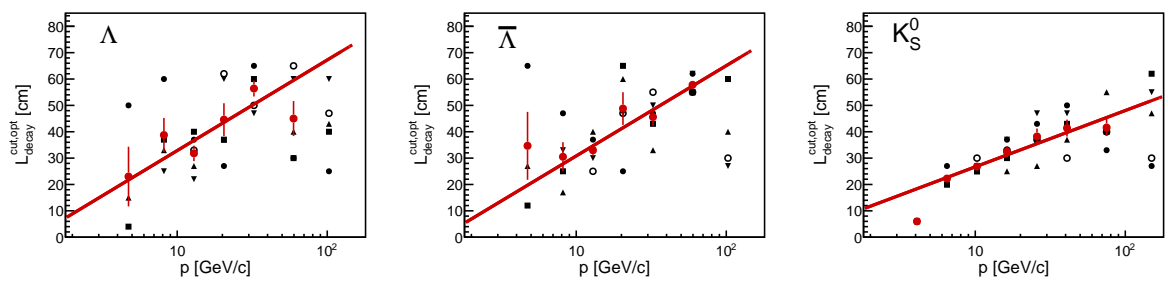


Figure 54 – Optimization of the  $L_{\text{decay}}^{\text{cut}}$  for the 350  $\text{GeV}/c$  dataset. The plot on left, middle and right shows  $\Lambda$ ,  $\bar{\Lambda}$  and  $K_S^0$ , respectively.

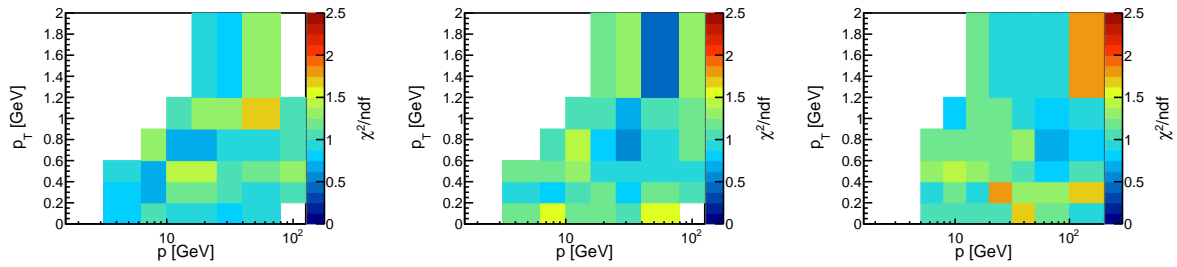


Figure 55

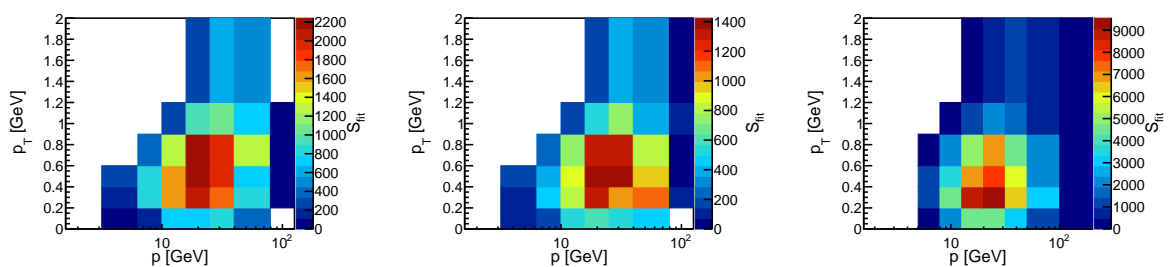


Figure 56

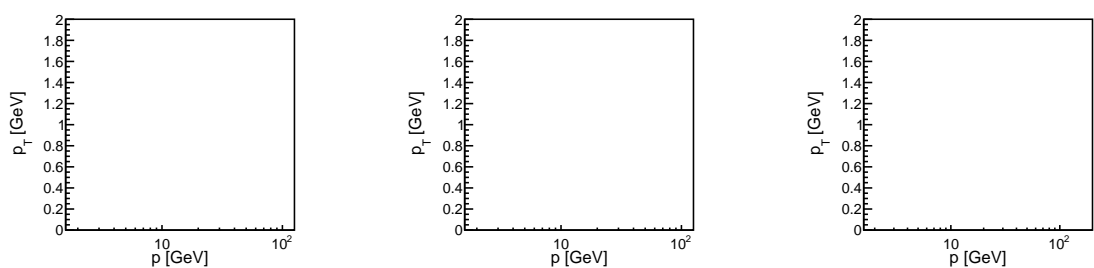


Figure 57

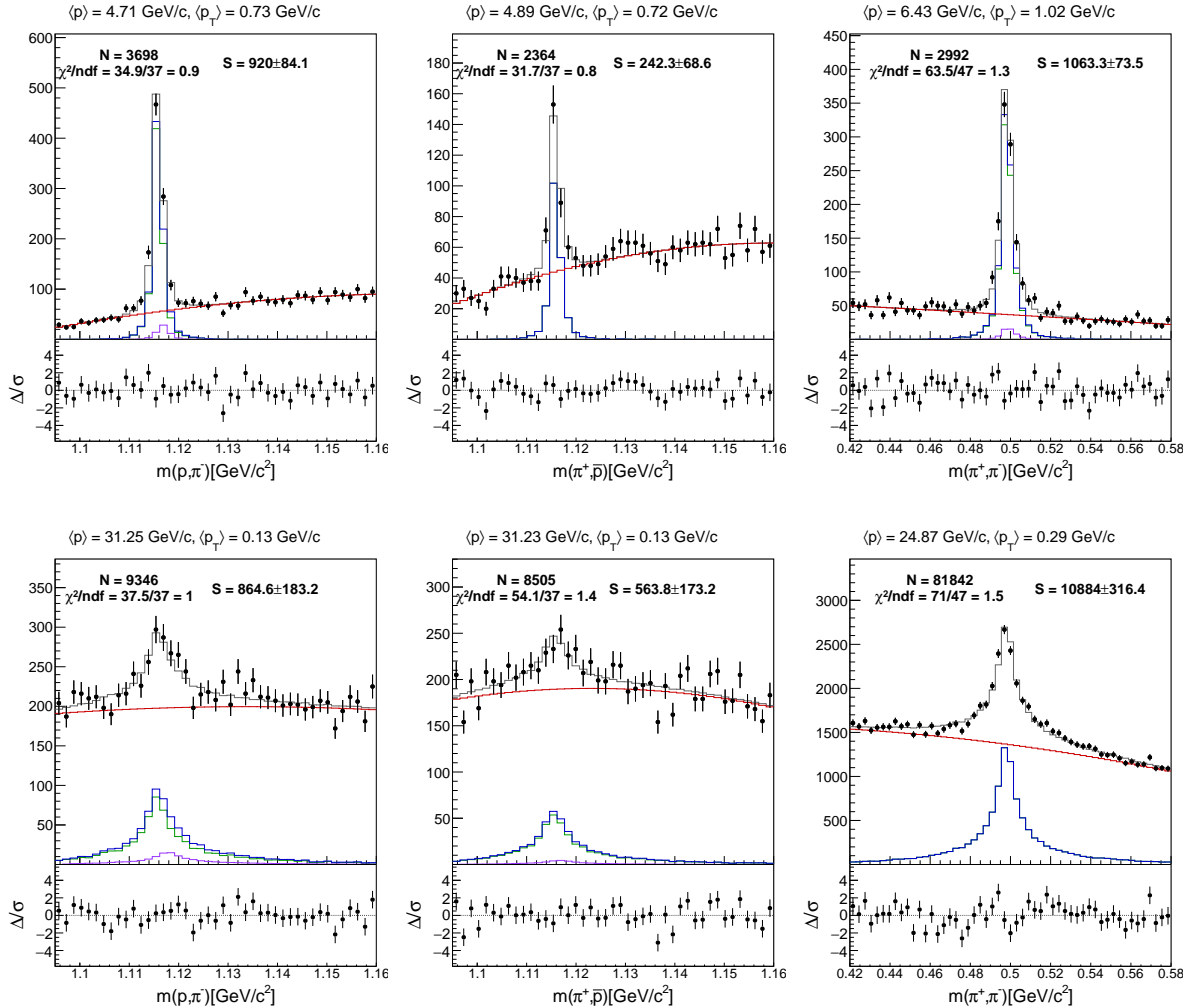


Figure 58 – Examples of the fitted  $m_{\text{inv}}$  distributions for the 350  $\text{GeV}/c$  dataset. The plot on left, middle and right shows  $\Lambda$ ,  $\bar{\Lambda}$  and  $K_S^0$ , respectively.

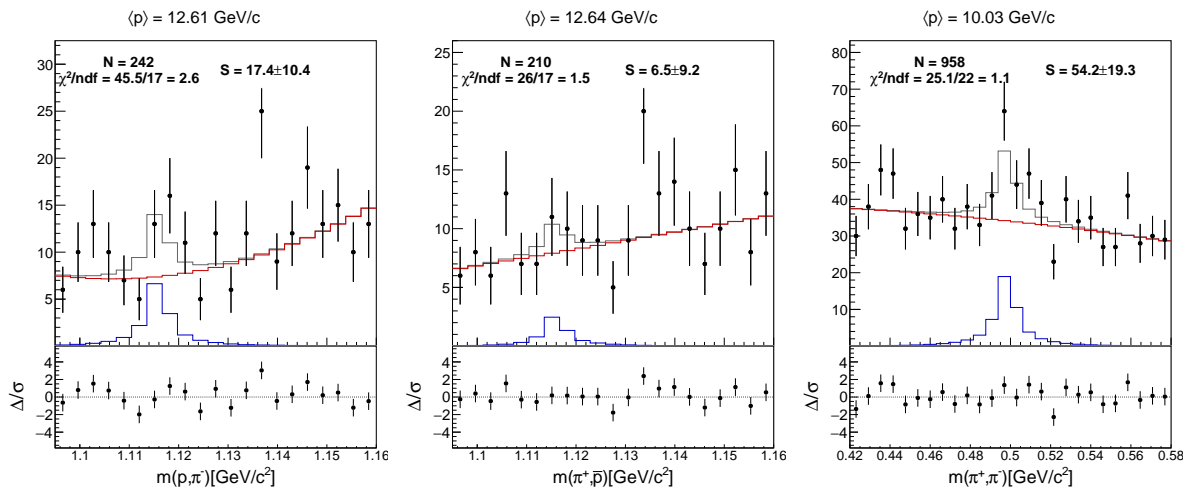


Figure 59 – Examples of the fitted  $m_{\text{inv}}$  distributions for the 350  $\text{GeV}/c$  dataset, with target removed. The plot on left, middle and right shows  $\Lambda$ ,  $\bar{\Lambda}$  and  $K_S^0$ , respectively.

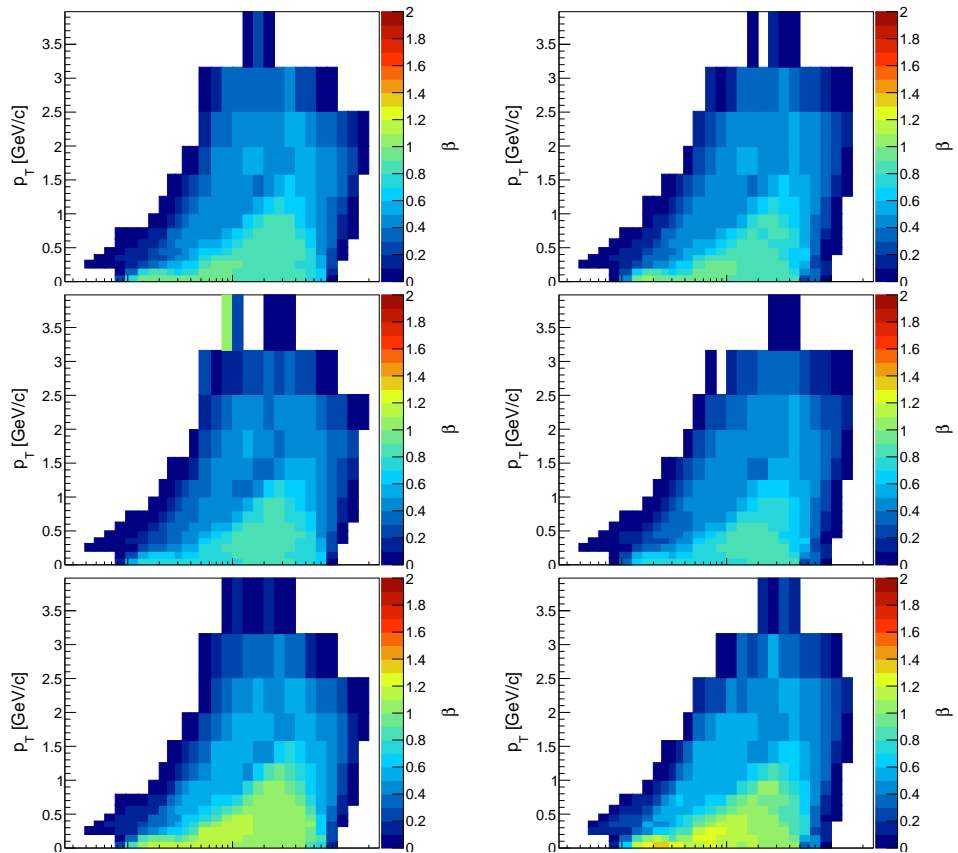


Figure 60 –  $\beta$  correction factor for the 350 GeV/ $c$  dataset.

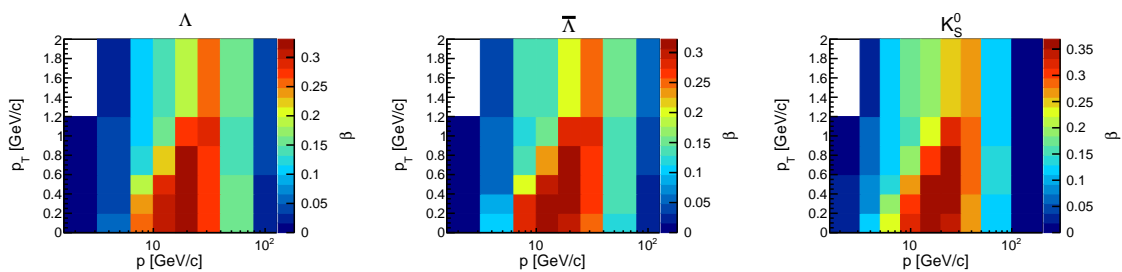


Figure 61 –  $\beta$  correction factor for the 350 GeV/ $c$  dataset.



## 8 Conclusions



# Bibliography

- 1 RUPRECHT, M. **Measurements of the Spectrum of Charged Hadrons in  $\pi^- + C$  Interactions with the NA61/SHINE Experiment.** 2012. Thesis (Masters) — Institute of Experimental Particle Physics, Karlsruhe Institute of Technology, 2012.
- 2 ADUSZKIEWICZ, A. et al. Measurement of meson resonance production in  $\pi^- + C$  interactions at SPS energies. **Eur. Phys. J.**, C77, n. 9, p. 626, 2017.
- 3 MARIS, I. C. Hadron production measurements with the NA61/SHINE experiment and their relevance for air shower simulations. In: **Proceedings, 31st International Cosmic Ray Conference (ICRC 2009): Lódź, Poland, July 07-15, 2009.** [S.l.: s.n.].
- 4 UNGER, M. Hadro production Measurements with NA61/SHINE for the Understanding of Extensive Air Showers. In: **Proceedings, 32nd International Cosmic Ray Conference (ICRC 2011): Beijing, China, August 11-18, 2011.** [s.n.]. v. 5, p. 67. Available from Internet: <[http://inspirehep.net/record/1352482/files/v5\\_1094.pdf](http://inspirehep.net/record/1352482/files/v5_1094.pdf)>.
- 5 DEMBINSKI, H. Measurement of hadron-carbon interactions for better understanding of air showers with NA61/SHINE. In: **Proceedings, 33rd International Cosmic Ray Conference (ICRC2013): Rio de Janeiro, Brazil, July 2-9, 2013.** [s.n.]. p. 0688. Available from Internet: <<http://www.cbpf.br/%7Eicrc2013/papers/icrc2013-0688.pdf>>.
- 6 HERVE, A. Results from pion-carbon interactions measured by NA61/SHINE for better understanding of extensive air showers. **PoS**, ICRC2015, p. 330, 2016. [34,330(2015)].
- 7 PRADO, R. R. Measurements of Hadron Production in Pion-Carbon Interactions with NA61/SHINE at the CERN SPS. In: **Proceedings, 35th International Cosmic Ray Conference (ICRC 2017): Bexco, Busan, Korea, July 12-20, 2017.** [s.n.], 2017. Available from Internet: <<http://inspirehep.net/record/1611552/files/arXiv:1707.07902.pdf>>.
- 8 ABGRALL, N. et al. NA61/SHINE facility at the CERN SPS: beams and detector system. **JINST**, v. 9, p. P06005, 2014.
- 9 AFANASEV, S. et al. The NA49 large acceptance hadron detector. **Nucl. Instrum. Meth.**, A430, p. 210–244, 1999.
- 10 ABE, K. et al. The T2K Experiment. **Nucl. Instrum. Meth.**, A659, p. 106–135, 2011.
- 11 ADUSZKIEWICZ, A. **Operation and performance of Time Projection Chambers of SHINE/NA61 experiment at CERN.** 2008. Thesis (PhD), 2008.
- 12 ABGRALL, N. et al. Calibration and analysis of the 2007 data. 2008.
- 13 BRUN, R.; BRUYANT, F.; CARMINATI, F.; GIANI, S.; MAIRE, M.; MCPHERSON, A.; PATRICK, G.; URBAN, L. GEANT Detector Description and Simulation Tool. 1994.

- 14 PIEROG, T.; WERNER, K. Muon Production in Extended Air Shower Simulations. **Phys. Rev. Lett.**, v. 101, p. 171101, 2008.
- 15 ROESLER, S.; ENGEL, R.; RANFT, J. The Monte Carlo event generator DPMJET-III. In: **Advanced Monte Carlo for radiation physics, particle transport simulation and applications. Proceedings, Conference, MC2000, Lisbon, Portugal, October 23-26, 2000**. [s.n.], 2000. p. 1033–1038. Available from Internet: <<http://www-public.slac.stanford.edu/sciDoc/docMeta.aspx?slacPubNumber=SLAC-PUB-8740>>.
- 16 OSTAPCHENKO, S. Monte Carlo treatment of hadronic interactions in enhanced Pomeron scheme: I. QGSJET-II model. **Phys. Rev.**, D83, p. 014018, 2011.
- 17 ABGRALL, N. et al. Measurements of Cross Sections and Charged Pion Spectra in Proton-Carbon Interactions at 31 GeV/c. **Phys. Rev.**, C84, p. 034604, 2011.
- 18 BLUM, W.; RIEGLER, W.; ROLANDI, L. **Particle Detection with Drift Chambers**. [S.l.]: Springer, 2008.
- 19 LEEUWEN, M. van. **Kaon and open charm production in central lead-lead collisions at the CERN SPS**. 2003. Thesis (PhD) — National Institute for Subatomic Physics (NIKHEF), 2003.
- 20 VERES, G. I. **Baryon Momentum Transfer in Hadronic and Nuclear Collisions at the CERN NA49 Experiment**. 2001. Thesis (PhD) — Department of Atomic Physics, Eötvös Loránd University, 2001.
- 21 MARCINEK, A.  **$\phi$  meson production in proton-proton collisions in the NA61/SHINE experiment at CERN SPS**. 2016. Thesis (PhD) — Institute of Physics, Jagiellonian University, 2016.
- 22 AAMODT, K. et al. The ALICE experiment at the CERN LHC. **JINST**, v. 3, p. S08002, 2008.
- 23 CHATRCHYAN, S. et al. The CMS Experiment at the CERN LHC. **JINST**, v. 3, p. S08004, 2008.
- 24 MORALES, Y. C. Identified hadron production in pp collisions measured with ALICE. **J. Phys. Conf. Ser.**, v. 878, n. 1, p. 012005, 2017.
- 25 CHATRCHYAN, S. et al. Study of the inclusive production of charged pions, kaons, and protons in  $pp$  collisions at  $\sqrt{s} = 0.9, 2.76$ , and  $7$  TeV. **Eur. Phys. J.**, C72, p. 2164, 2012.
- 26 KARBACH, T. M.; SCHLUUPP, M. Constraints on Yield Parameters in Extended Maximum Likelihood Fits. 2012.
- 27 JAMES, F.; ROOS, M. Minuit: A System for Function Minimization and Analysis of the Parameter Errors and Correlations. **Comput. Phys. Commun.**, v. 10, p. 343–367, 1975.
- 28 BARNA, D. **Strange Particle Production in Proton-Proton Collisions at 158 GeV**. 2002. Thesis (PhD) — Doctoral School of Physics, Eötvös Loránd University, 2002.

- 
- 29 CZOPOWICZ, T. **Study of  $K_0^S$  meson production in NA61 experiment at the CERN SPS.** 2010. Thesis (Masters) — Warsaw University of Technology, Faculty of Physics, 2010.
- 30 ABGRALL, N. et al. Measurements of  $\pi^\pm$ ,  $K^\pm$ ,  $K_S^0$ ,  $\Lambda$  and proton production in proton–carbon interactions at 31 GeV/c with the NA61/SHINE spectrometer at the CERN SPS. **Eur. Phys. J.**, C76, n. 2, p. 84, 2016.
- 31 ADUSZKIEWICZ, A. et al. Production of  $\Lambda$ -hyperons in inelastic p+p interactions at 158 GeV/c. **Eur. Phys. J.**, C76, n. 4, p. 198, 2016.